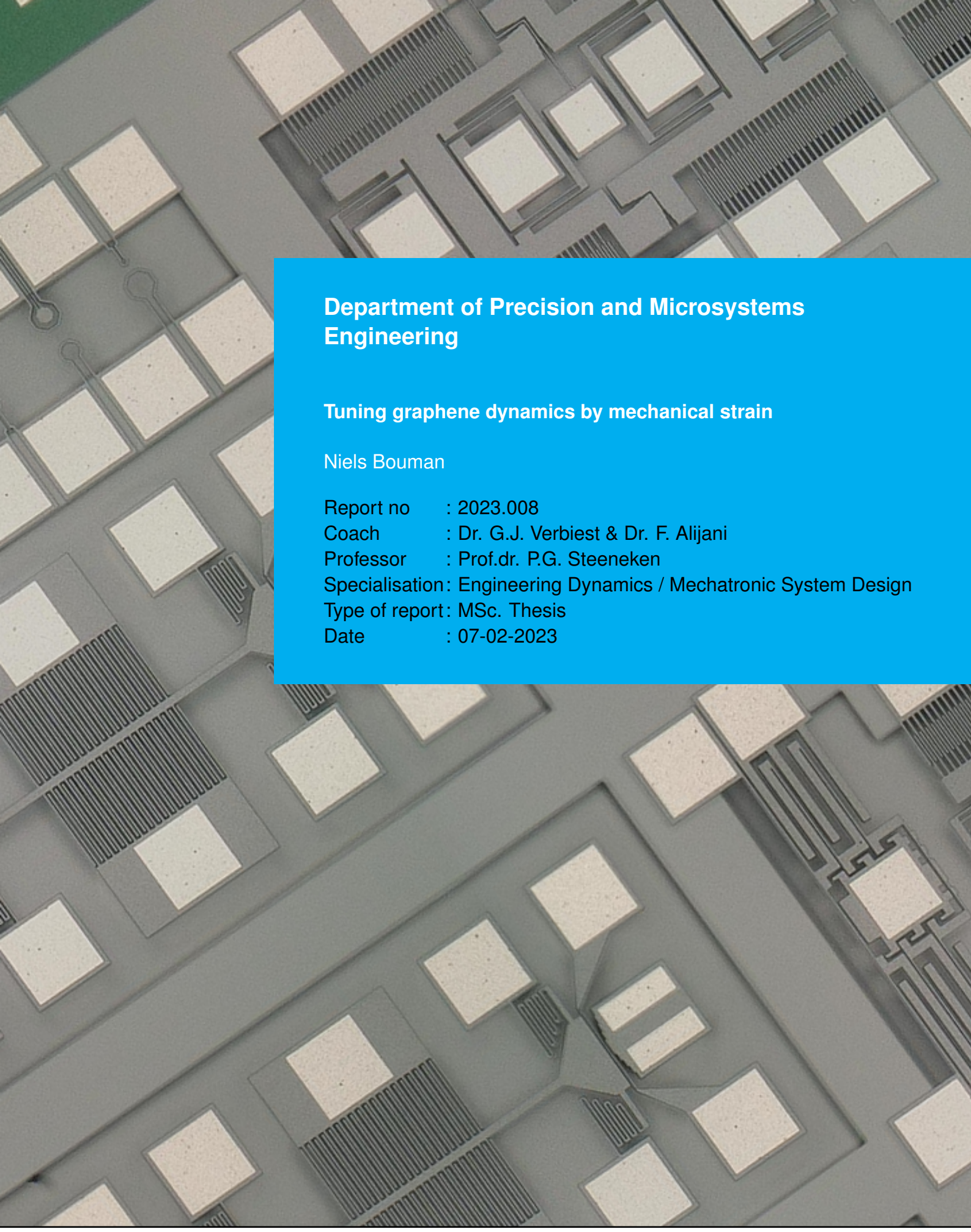

Department of Precision and Microsystems Engineering

Tuning graphene dynamics by mechanical strain

Niels Bouman

Report no : 2023.008
Coach : Dr. G.J. Verbiest & Dr. F. Alijani
Professor : Prof.dr. P.G. Steeneken
Specialisation : Engineering Dynamics / Mechatronic System Design
Type of report : MSc. Thesis
Date : 07-02-2023

TU Delft Delft University of Technology

Challenge the future

Tuning graphene dynamics by mechanical strain

by

Niels Bouman

to obtain the degree of Master of Science

at the Delft University of Technology,

to be defended publicly on Tuesday February 7, 2023 at 3:00 PM.

Student number:	4654676	
Project duration:	October, 2021 – Februari, 2023	
Thesis committee:	Dr. G. J. Verbiest,	TU Delft, supervisor
	Dr. F. Alijani,	TU Delft, supervisor
	Prof. dr. P. G Steeneken	TU Delft, supervisor
	Dr. T. Manzaneque Garcia	TU Delft

This thesis is confidential and cannot be made public until December, 2023.

TU Delft

Preface and abstract

Preface

During the past year and-some-months, I was privileged to work on fascinating fundamental research on a material that has thrilled me for years. I got to do this under the surveillance of three very passionate professors. I greatly enjoyed learning new techniques to probe the physical phenomena smaller than I had ever imagined existing. Together with the help of almost the full PME department and beyond, we pushed the boundaries on what was previously not possible. I thank everyone involved in one way or another to the success of this project:
Gerard, Farbod, Peter, Curry, Ata, Ruben, Izak, Ahmed, Tuhan, Maurits, Ali, Makars, Daniel, Irek, Murali, Hadi, Andrea, Roberto, Gabriele, Zichao, Andres, Alex, Gideon, Bradley, Patrick, Rob, Spiridon and all the people there daily to drink a cup of coffee with: Yannick, Cas, Menno, Stijn, Viktor, Tom, Jaap, Jan, Dennis, Manal, Martijn, Viktor and more. It was a pleasure.

Niels Bouman
Delft, January 2023

Abstract

Two-dimensional (membrane) materials have been receiving much scientific attention due to their unique material properties that can be used to study the smallest physical phenomena. One such material is graphene, perceived as the holy grail in material physics, due to its unique material properties. Its aspect ratio diminishes the bending rigidity and allows wrinkles, ripples and other morphological imperfections to dominate the mechanical behaviour. Applying tension is a necessity to control these geometrical imperfections and simultaneously opens up pathways to study physical phenomena such as magnetism, superconductivity, optics and much more. Typically, this tension is applied using electrostatic forces, which alters amongst others, the electric properties of the material. Mechanically applied tension offers a solution to this problem but comes at the cost of difficult manufacturability. In this work, a new method to incorporate 2D materials with N/MEMS is presented. The dynamics of mechanically tensioned graphene are probed in linear and nonlinear regimes. The former regime finds the exact opposite of what is observed in electrostatically tensioned membranes. The latter shows exotic nonlinear effects that can be tuned by applying tension. Furthermore, it is identified that the dynamics of the MEMS device are coupled to that of the resonating membrane despite their mass and stiffness being roughly five orders of magnitude apart. The bottleneck of this project is the adhesion force between the two is insufficiently strong to apply significant strain allowing slippage to occur.

List of Figures

List of Tables

Contents

1

Introduction

Combining extremely high-, electron mobility, thermal conductivity, in-plane stiffness and transparency to something that is chemically inert, impermeable to gasses (except hydrogen [108]) and atomically thin make graphene the holy grail of material properties [2, 17]. Its absurdly large surface-to-volume ratio allows applications in sensors of many kinds. Since it was discovered how to produce graphene by A. Geim et al. [40], it has been of great interest for research in all fields of science. In the field of micro- and nanoelectromechanical systems (M/NEMS), suspended 2D materials can be used for smaller, more sensitive and new functionalities in sensors compared to their silicon-based M/NEMS counterparts [72]. To use suspended graphene or related two-dimensional (2D) materials in sensing applications, a proper understanding of their mechanics is necessary. There are however many uncertainties regarding arguably the most important property; its Young's modulus, as shown in Table 1 there is a large spread in experimentally obtained values. The theoretical intrinsic Young's modulus is in hovers above 1 TPa, but is degraded in practice due to several factors such as: the substrate its grown (in the case of CVD), the presence of defects in the atomic lattice, contaminants, humidity and temperature of the environment. Additionally, for multi-layered graphene, this value degrades due to the presence of van der Waals forces between the layers.

Method	E (GPa)	Source
AFM	500,920,1120	[38, 89, 4]
Electrostatic deflection	1000	[121]
Pressurized blister	1000	[67]
Spring constant scaling	430	[110]
Coupled tunable resonators	350 [N/m] = 1000	[113]
Fitting nonlinear stiffness	590	[24]
Δf_{res}	560	[93]

Table 1.1: Different experimental methods of determining the Young's modulus of graphene shows a large non-uniformity.

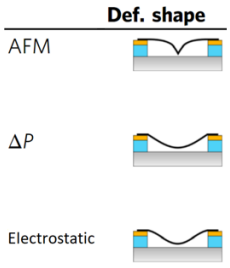

Figure 1.1: Membrane deformation for different probing methods. Adapted from [24].

On top of that, the apparent strength of a graphene membrane seems to also be strongly related to the morphology of the surface [95]. Controlling the surface morphology is therefore of significant relevance. The field of M/NEMS introduces a new strategy to exert engineerable strain fields to control the surface morphology, similar to macroscopic tensile test benches [44]. These devices are a new tool to study the influence of strain on the linear and nonlinear dynamics of such membrane resonators which show exotic dynamical behaviour [62].

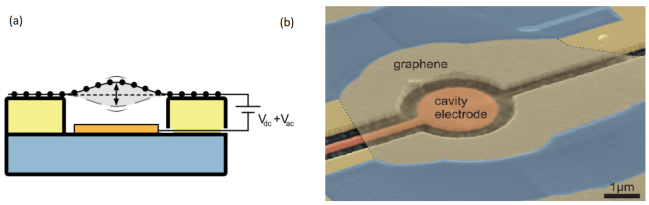

Figure 1.2: Schematic (a) of electrostatic tensioning and actuation through the summation of a constant bias and alternating voltage, the former of which is responsible for pre-straining the membrane. Image adapted from [105]. (b) A false-colour SEM image of an exemplary setup adapted from [118].

This introduction investigates the state-of-the-art methods that have been used to strain graphene in search of proper characterization for these challenging-to-handle materials and introduces their dynamical behaviour in Section 1.1. This allows for the identification of a knowledge gap and formulation of a research- question and plan in Section 1.2. The steps required to perform the experiments are presented in Section 2. Then the main results and discussion hereof are given in Sections 3&4. The conclusion to this thesis is found in Section 5

1.1. State of the art

Combining graphene or other 2D materials with M/NEMS resonators allows for the development of devices that can probe the smallest physical phenomena such as pseudo magnetic fields [44]. This section aims to cover the state-of-the-art research that has been done in the field of straining and resonating graphene and related 2D material membranes with a focus on experimental works. A knowledge gap is identified concerning how uniaxial tension causing strain, affects the dynamics of such 2D membranes.

1.1.1. Straining membranes

During the fabrication and or transfer of graphene samples, morphological defects such as folds and wrinkles are likely to occur. There is an extraordinarily low bending rigidity in graphene and other atomically thin membranes [15]. These wrinkles can e.g. form due to topological defects in the atomic structure to minimize the deformation energy [91]. There exists a tight relation between the morphological and electronic properties of graphene [59, 91]. Therefore, in many types of experiments, it is necessary to apply strain such that there is no random play which can cause hysteresis and in general make measurements less reproducible. Especially for experiments into dynamics, this control is desirable since the morphology is strongly linked to dynamical behaviour. There exist many methods to induce strain in graphene and other low-dimensional membranes. On top of controlling the morphology, other fascinating physical effects exist that can be controlled or probed by straining 2D materials. Examples of such include superconductivity (and thus electronic band structure), optical- and magnetic properties [44]. This section will swiftly describe some of the more recent approaches to induce strain. The approach in which tension is applied to the membrane alters the mechanical, optical and electronic properties. These effects should be taken into account when interpreting results.

Electrostatic

Electrostatically induced strain is one of the more often implemented methods of inducing strain in suspended sheets such as graphene. By applying a voltage to an electrostatic gate electrode parallel to the membrane, a potential difference is created between the membrane and the gate electrode. This creates attracting forces analogous to those between a parallel plate capacitor. This force deflects the membrane towards to gate and thereby inducing strain. The gate is typically located under the suspended membrane [9, 46, 81, 104]. Such schematic is illustrated in Figure 1.2.

A drawback of tensioning and actuating the membrane resonator in this manner is that the strain field is intrinsically linked to the electronic tuning of the charge carrier density [44, 126]. This in turn also affects the mechanical properties of the membrane. A higher charge carrier density results in a locally weaker material. Which thereby introduces strong nonlinear effects in the equation of motion for a large gate bias [46].

Bending carrier
Another one of the more common methods of inducing strain in graphene is by having laid out on a flexible substrate. Here there are multiple approaches to take. The substrate can be for example flexible by itself [46], the substrate could be bent using mechanical force [79] or the substrate can be a piezoelectric material [69]. The graphene itself can also be either adhered on top of the substrate or suspended above a cavity or trench. This is depicted in Figure 1.3.

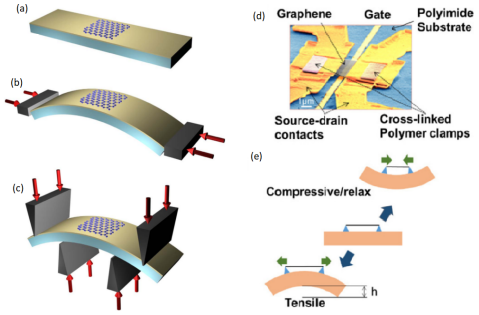

Figure 1.3: (a-c) Straining of a 2D material by bending the substrate. Image adapted from [79] (d-e) Straining of a 2D material by suspending it and subsequently bending the flexible substrate. Image adapted from [46].

The downside in the former case is that the obtained strain field is intrinsically linked to the properties of the substrate [44]. Since the membrane will be strained through the adhesive forces with the substrate. It will therefore follow the substrate corrugations which can induce local slippage when straining and thus hysteresis. In the latter case, when the membrane would be suspended, it will be the geometry of the cavity that will cause nonlinearities depending on what experiments are performed [46]. This will prevent the sample from reaching reliable results in the larger strain domain. An advantage however to this method would be that the effects of membrane sagging or buckling can be studied to the reversibility of the straining by bending process. This sag (amongst other factors) has been linked to quadratic nonlinear terms in the equations of motion which can lead to a so-called "spring softening" effect [81].

Pressure
Strain can also be applied to a graphene membrane by having it separate two volumes of different pressure. This is visually depicted in Figure 1.4.

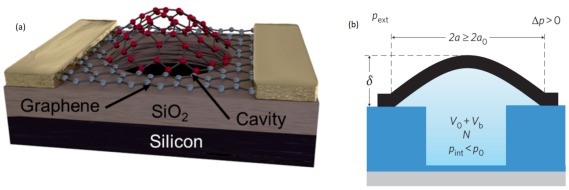

Figure 1.4: (a) Digital illustration of a graphene membrane that is strained due to a cavity with a higher pressure that the environment. Image adapted from [101]. (b) Schematic overview of the parameters that describe this strained geometry, notable is that parts of the membrane can peel at the edge. Image adapted from [67]

This type of straining is not useful for dynamic applications because the ambient pressure causes viscous effects that damp the movement of the membrane and ultimately deteriorate the quality factor (Q-factor, defined in Section 1.1.2) of vibration [33].

Thermal
Making use of the negative coefficient of thermal expansion ($\alpha_{gr} \approx -7e{-}6\,K^{-1}$ at room temperature [98]), it is possible to strain a graphene membrane using heat. One way to do so is by suspending a membrane on a carrier which expands due to heating from ohmic dissipation, whilst the suspended graphene contracts due to the elevated temperatures. Such has been demonstrated by Davidovikj [26]. This form of electrothermal straining has shown an interesting effect, namely an increase in Q-factor of up to 10%. For electrostatic actuation and straining, typically a decrease is observed which has been linked to the Joule dissipation from the displacements of currents through the membrane which is an interesting contradiction between the methods. An illustration is given in Figure 1.5

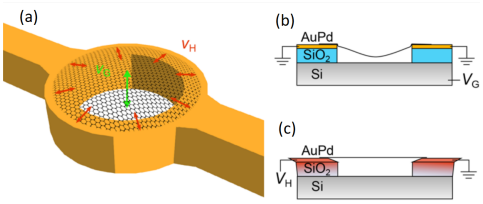

Figure 1.5: (a) CAD representation of a graphene membrane suspended on a conductive carrier. (b-c) Representation of strain field comparison between electrostatic strain or in-plane thermal strain

Another way to increase a graphene resonator's temperature and thereby strain it; is by absorption of optical power [9]. Diode-lasers have been repeatedly used to strain and drive graphene resonators [62, 34, 36]. Since this strain modulates the internal tension and therefore the stiffness, this method is often combined to strain and parametrically actuate graphene resonators.

Uniaxial tension by MEMS
In order to optimally study the electronic, optical, mechanical and even thermal properties of graphene, it is required to achieve high strain values. Controllable homogeneity is also preferred for repeatable experiments. To achieve this independent control over the strain, that is without linking the electrical tuning of the charge carrier density or mechanical properties of the substrate to the strain field [43]. Such is for example the case when electrostatically straining the membrane since the membrane acts as one of the parallel plates of a capacitor. When the membrane is deposited on a deforming substrate, it introduces disorder, charge puddles and surface imperfections.

MEMS devices provide a solution to solely adjust the mechanical degrees of freedom for graphene membranes without affecting other parameters (e.g. temperature, pressure, charge carrier density). By mechanically exerting uniaxial tension on the membrane, independent strain can be achieved. The production of such devices is typically achieved using standard micro-machining techniques. Examples of such devices are depicted in Figure 1.6.

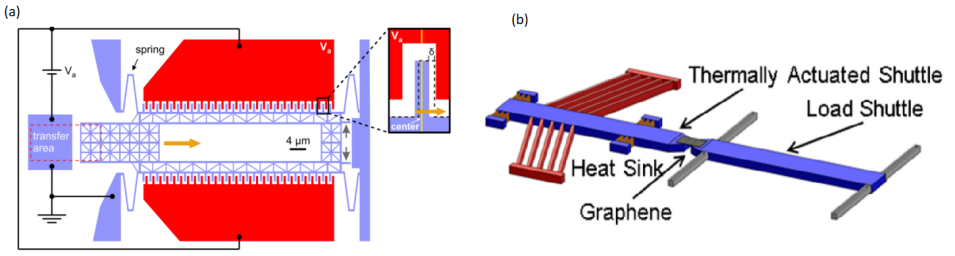

Figure 1.6: Two types of MEMS devices to strain graphene. (a) Using electrostatic comb drive (CD) actuators. Image adapted from [42]. (b) Using an electrothermal actuator known as a Chevron actuator. Image adapted from [85].

The next step according to Newton's third law is to clamp the membrane. For it will likely slip when large strain values are desired. In literature, this has been achieved using two main routes. By micro-pipetting/depositing a type of adhesive like epoxy [85, 122, 86] or by cross-linking a polymer deposited on the clamping region of the membrane by means of lithographic techniques [43, 42, 44, 46, 113, 115]

What is interesting to note is that the reported strain values for the experiments utilizing an adhesive report significantly higher achievable strain gradients. For the adhesive clamped membranes the maximum strain value for graphene and MoS_2 exceeds 10% [85]. This is interesting because according to [42], the maximum strain values for membranes at this scale is only 4%. The maximum measured strain using a PMMA clamp is therefore 1.4% [44]. This suggests that there might be creeping of the adhesive that could reinforce the resonating membrane. Such contamination might not always be detectable with popular characterization techniques such as Raman spectroscopy, optical- or even atomic force microscopy [35].

1.1.2. Linear dynamics

The linear dynamics of nano-electromechanical oscillators are relatively well understood. For the undriven suspended resonating membrane (or any other resonator) the general equation of motion (EoM) contains only three terms as shown in Equation Eq. (1.1).

$$m_i \ddot{q}_i + c_i \dot{q}_i + k_i q_i = 0 \tag{1.1}$$

Where the displacement q_i remains relatively small. A solution to this equation, assuming small damping ($c_i \ll \sqrt{4k_i m_i}$), can be found by testing out the trial solution $q_i(t) = q_{i,0} e^{\lambda_i t}$. This results in the equation:

$$\lambda_i^2 m_i + \lambda_i c_i + k_i = 0 \tag{1.2}$$

Where λ is now solved using the small damping approximation to be:

$$\lambda_{i\pm} = -\frac{c_i}{2m_i} \pm i\sqrt{\frac{k_i}{m_i} - \frac{c_i^2}{4m_i^2}} \approx -\frac{\omega_i}{2Q_i} \pm i\omega_i \tag{1.3}$$

Substituting this solution back into the trial solution gives the membrane vibration:

$$q_{i\pm}(t) = q_{i,0\pm} e^{\frac{-\omega_i t}{2Q_i} t} e^{\pm i\omega_i t}. \tag{1.4}$$

Where $\omega_i = \sqrt{k_i/m_i}$ is the resonance frequency and $Q_i = \sqrt{k_i m_i}/c_i$ is the quality factor of the resonance. In typical experiments, the resonator is however driven. The EoM for such a linear system then becomes:

$$m_i \ddot{q}_i + c_i \dot{q}_i + k_i q_i = F_{\text{ext, i}}(\omega) e^{i\omega t}. \tag{1.5}$$

Where the periodic driving force is now written as a Fourier sum ($F_{\text{ext, i}}(t) = F_{\text{ext, i}}(\omega) e^{i\omega t}$). The steady-state solutions must also be periodical such that $q_i(t) = Q_i(\omega) e^{\omega t}$. The frequency response function (FRF(ω)) and the magnitude hereof can now be described by the following equations [105]:

$$\frac{q_i(\omega)}{F_{\text{ext, i}}(\omega)} = (-\omega^2 m_i + i\omega c_i + k_i)^{-1} \tag{1.6}$$

$$\left| \frac{q_i(\omega)}{F_{\text{ext, i}}(\omega)} \right| = \frac{1}{\sqrt{\left(k_i - m_i\omega^2\right)^2 + (c_i\omega)^2}} \tag{1.7}$$

When doing experiments, it are these Equations 1.6 and 1.7 which allow fitting the data to extract the resonance frequency and Q-factor [21]. What needs to be noted however is that for example, m_i does not represent the mass of the resonator. It is a numerical coefficient related to the mass of the system but depends on mode shape and resonator geometry [105]. As an example, for a perfectly circular drum resonating at its fundamental mode, the modal mass $m_1 = 0.2695m$ where $m = \rho h \pi R^2$ is the actual mass of the drum. When doing experiments however these values will have to be experimentally determined due to fabrication imperfections of the device and material.

The Q-factor of a resonator is linked to the sensitivity it can have in practical applications. The higher the Q-factor, the more accurate shifts in resonance frequency and amplitude can be observed and the better the sensor. Until now, the Q-factor in membrane resonators such as graphene has remained relatively low compared to for example their MEMS counterparts [16]. Imperfections in surface morphology such as wrinkles and folds have been linked to the deterioration of this Q-factor [69]. And therefore should be increased with a controlled tensile strain field. The Q-factor is defined as the ratio between the resonance centre frequency and the half-power bandwidth. Stronger damping in a system thusly lowers the Q-factor.

$$Q = \frac{f_r}{\Delta f} = \frac{\omega_r}{\Delta \omega} = \frac{\text{Resonant frequency}}{3\,\text{dB bandwidth}} \tag{1.8}$$

Interestingly enough, for resonators on this scale, even an undriven membrane can show resonance behaviour due to thermal fluctuations. For example, single atoms that are colliding with the membrane or from phonons at the coupling points between the suspended membrane and substrate [15, 105].

Understanding the linear dynamics of a suspended membrane resonator like graphene already opens up a world of sensing applications possibilities. Measuring a shift in resonance frequency or amplitude allows for extremely sensitive mass or pressure sensors [72]. In real systems, it can however be challenging to fully understand even the linear dynamics since the material properties are difficult to measure using conventional characterization techniques that are available for instance for MEMS devices. Furthermore, during the fabrication of graphene and related 2D materials, there are many deviations from sample to sample, the atomic structure, the morphology, and substrate surface adhesion may all deviate from sample to sample and ultimately play a significant role in this atomically thin scale.

1.1.3. Nonlinear dynamics

As a result of the atomic-scale thickness of graphene and related 2D materials, their behaviour in dynamical systems is exotically rich compared to their macroscopic counterparts [16]. The nonlinear regime of typical graphene oscillators can already be probed at picoNewtons of force [24]. This brings to the table new possibilities for enhancing force sensitivity, effective quality factor and signal-to-noise ratio [36]. Interestingly enough, even material properties such as the Young's modulus can show nonlinearities as a result of surface corrugations [95]. A good understanding of the complete (nonlinear) dynamics of such resonators is crucial when pushing the performance of applications to their full potential [28]. This section will give insight into some of the most relevant works that discover and engineer nonlinear behaviour in such resonators.

Damping, mode coupling and internal resonance

Damping is an effect that occurs all around in mechanical systems. The nonlinear dissipative mechanisms are typically overshadowed by linear viscous damping, but not for resonators at the atomic thickness scale [97]. In typical room-temperature graphene resonators, a low quality-factor (Q) is observed. The Q is inherently linked to the energy dissipation and thus damping of the system. A good understanding of the dissipative mechanisms allows for better engineerable dynamics such as improved Q [27].

When modelling nonlinear damping in graphene resonators, a van der Pol type is often considered. Extending the linear undriven equation of motion (1.1) would in this case become:

$$m_i \ddot{q}_i + c_i \dot{q}_i + \tau_{\mathrm{nl},i} q_i^2 \dot{q}_i + k_i q_i = 0 \tag{1.9}$$

Where $\tau_{\mathrm{nl},i}$ is the nonlinear damping coefficient. This term is particularly important for modelling when parametric excitation is involved. Parametric excitation allows for resonance of amplitudes that are much larger than conventional excitation can achieve [37]. Note that there is no excitation term in Equation 1.9. For parametric actuation works by altering a device parameter, typically the stiffness [107]. At low drive levels, small parametric excitations do not cause particularly large deflections, until a threshold is reached at which large deflections can be realized. In the EoM this is represented as such:

$$m_i \ddot{q}_i + c_i \dot{q}_i + \left(k_i + k_{\mathrm{p},i}(T(t))\right) q_i = 0 \tag{1.10}$$

Where the term $T(t)$ has to be of twice the fundamental resonance frequency in order to parametrically excite the system at its fundamental mode. This is the driving principle of Opto-thermal actuation. Since the stiffness is altered by the heating and cooling causing tension and relaxation respectively [90]. The van der Pol term ($\tau_{\mathrm{nl},i} q_i^2 \dot{q}_i$) is typically in the same equations as it is responsible for the (parametric) resonance amplitude to not shoot off to infinity [62]. One of the phenomena that is hypothesised to be responsible for this nonlinear energy dissipation is coupling of modes where vibrational energy is transferred between modes. This mode coupling is dependant on the drive energy of the system, for at low driving forces, modes are decoupled and linear viscous damping dominates [47]. At higher driving frequencies, a strong intermodal coupling occurs through the effect of internal resonance (IR). Which is when the ratio of resonance frequencies approaches a rational number [62, 123]. This effect can be used to increase the frequency stability of such resonators [5]. So far, it has been shown that describing the nonlinear dissipation in such system is generally well described using a van der Pol term in the EoM [36]. However for increasingly large driving amplitudes, nonlinear damping can be separated into multi-level systems. Where at a certain amplitude the one system (e.g. the van der Pol term) can become saturated and a new terms come into presence (such as $\rho \left|q\right| \dot{q}$, or $\lambda \frac{\dot{q}}{1+|q|}$). These terms can even have an opposite sign such that damping rate decreases. Such has been observed in [99].

A multitude of other mechanisms have also been blamed to constitute to nonlinear damping such as thermoelastic- and viscoelastic damping, phonon-phonon interactions, clamping losses and more [125]. Isolating these mechanisms to study their respective effects is a challenging task for M/NEMS oscillators. Having independent control over the strain field by means of a MEMS device would allow for greater tunability of dynamical behaviour which in turn should allow for better experimental research of nonlinear (dissipative) effects.

Nonlinear stiffness

In dynamical systems, stiffness is often not linear. Even the spring constant for a regular helical spring is not a constant when the spring is deflected enough. Nonlinear stiffness can be represented in the equation of motion in many forms, the most common nonlinear term used to model the dynamics and fit experimental data is the cubic stiffness also known as the Duffing [105]. It appears in the undriven EoM as such:

$$m_i \ddot{q}_i + c_i \dot{q}_i + k_i q_i + \gamma q_i^3 = 0 \tag{1.11}$$

The effective stiffness due to this extra term thus becomes $k_{\text{eff},i} = k_i + \gamma q_i^2$. Depending on the sign of γ, the total stiffness (and thus resonance frequency) can therefore increase or decrease which is referred to as respectively spring hardening and -softening. Which in turn alters the perceived resonance frequency. The duffing parameter γ can be dependant on many factors such as the device geometry, where symmetry breaking aspects typically tend to increase the nonlinear behaviour, residual strain and inhomogeneities hereof, electrostatic back action and more [46, 103]. For increasing drive powers in for example optothermally driven graphene resonators, a hardening effect is typically observed [62]. However, for electrostatic actuation, a typical softening effect is observed [84]. Effects of even higher-order nonlinearities can be overshadowed by quadratic and cubic terms. By electrostatically softening the natural hardening effect, the duffing response can be compensated which allows probing the nature of even higher-order nonlinearities [94].

The nonlinear stiffness has proven a promising tool to characterize the Young's modulus for graphene [24]. It is fast, contactless and allows for characterization for high-frequency resonating applications. By developing an accurate model of the vibrations of the graphene resonator, it has been shown that this Duffing parameter depends on the Young's modulus and therefore can be used to determine it [24]. The values obtained using this method shows a close correlation between characterization using static deformation using electrostatic forces.

This particular Duffing type nonlinear stiffness can be exploited to detect particularly weak signals [112]. In a process called stochastic switching. Due to the nature of a Duffing response, two points exist where the stability of the vibrational state abruptly changes which are saddle-node bifurcations. Driving the membrane in between these points whilst adding noise to the drive frequency to provoke the switching [32]. After calibration, the changes in the probability distribution of the vibrational state of the oscillator can be used to effectively measure very weak signals.

1.2. Project proposal

1.2.1. The goal

The ultimate goal of this thesis is to derive the Young's modulus of graphene (modulus of elasticity, denoted E). A large spread in these values has been reported ranging from as low as 130 GPa up to 1.1 TPa [30]. This can partly be explained due to the multitude of different contact, non-contact, static and dynamic methods for characterizing elastic properties. Each with its respective issues. Typical examples of such methods are atomic force microscopy (AFM) deflection techniques [70], electrostatic deflection [46, 81] or the pressurized blister test [67]. A recurring uncertainty in most experiments involving graphene or other two-dimensional (2D) materials is the wrinkling of the membrane that can occur with the fabrication of the sample due to virtually zero out-of-plane stiffness. This, amongst others, is why the exact physics that governs the elastic properties of 2D materials remains a topic that is subject to debate [75]. When investigating the elastic properties of 2D materials this effect of wrinkling contributes largely to the spread in reported Young's modulus values [2]. These wrinkles also alter other material properties such as electronic conductivity [30]. Having independent control over the strain field in graphene membranes would allow for a more controllable level and type of wrinkling, thereby increasing the accuracy and repeatability for experimental characterization experiments [44].

It has been shown that the dynamic deflections of graphene membranes can be read out with high accuracy using interferometric principles [9, 16, 24, 25]. The focus of this work will therefore be to study the dynamics of graphene membranes. Particularly on how the dynamics are affected as strain is exerted upon the membrane and if this changes the extracted mechanical properties. There is no experimental work in literature yet that has investigated the effect of uniaxial mechanical tension on the nonlinear dynamics of a doubly-clamped membrane. Regular effects of strain on membranes

typically include a tunable resonance frequency and an increase in the quality factor of its fundamental resonance due to a decrease in energy dissipation [26]. Although this latter effect seems to depend on the method with which the strain is induced. For that induced by an electrostatic force (out of plane) has shown an increase in energy dissipation and therefore a decrease in quality factor which is essential for e.g. force sensing applications [120]. Besides the regular effect of strain on membrane dynamics, the strain also affects imperfections from the fabrication such as edge adhesion, sag and wrinkles.

One particularly interesting research has looked into the characterization of the Young's modulus by means of analyzing the Duffing type nonlinear stiffness [24]. This thesis will aim to improve on this process by applying an independent strain field through mechanically pulling the membrane with a MEMS device.

With that in mind is it possible to formulate a research question: "Does mechanical tensile strain affect the nonlinear dynamic characterization of graphene's Young's modulus". Would this question be answered, there remains a copious amount of other experiments that can be performed on the same sample that involves mechanical strain in graphene.

1.2.2. The requirements

To study the strained dynamics, uniaxial tension will be applied to the membrane by means of a pre-designed micro-electro-mechanical system (MEMS) similar to that as designed by Goldsche et al. [42]. On this device, a few-layer graphene sheet needs to be deposited. There are numerous methods for transferring graphene membranes and even sheets, determining the correct procedure is essential since the transfer is on a fragile MEMS device. The dynamics can be analyzed using a setup built by Dr. Keskeler such as has been described in his work [62]. Which will is described in Section 2.3

2

Methods

In order to fabricate a device capable of mechanically applying strain to graphene or other 2D materials, an elaborate manufacturing process is unavoidable. The generalised process flow can be divided into three main stages. These are enumerated as follows:

1. Fabrication of MEMS device.
2. Transferring 2D material onto device
   - Obtaining 2D material.
   - Transferring 2D material.
   - Further development of the straining device.
3. Obtaining experimental data.

The purpose of this chapter is to describe all the methods that were involved in obtaining what ultimately be a graphene-straining MEMS device, in such a way that someone reading this could perform the same process. Not all methods described did directly contribute to the solution but were part of the process nevertheless.

2.1. Fabrication of the device

The following section will take the reader through the steps that have led to the successful fabrication of MEMS devices for graphene transfer. This process can be split up into three main phases; MEMS fabrication, graphene transfer and post-processing of the MEMS device.

2.1.1. Design of MEMS device

In order to mechanically apply strain on a 2D material membrane, a MEMS device was designed.

The design at hand has a large resemblance to MEMS type Inertial Measurement Units (IMUs). These types of sensors are also relatively thick in the out-of-plane direction and require a large surface area between static and dynamic comb fingers to maximize capacity for accurate detection of acceleration. Therefore a company (X-FAB Semiconductor Foundries) with expertise in the fabrication of such devices has produced the wafer with these MEMS devices. Figure 2.1 shows the device in greater detail.

This comb-drive (CD) device functions as a simple tensile bench for 2D membrane materials. By being able to pull on the suspended shuttle by means of electrostatic forces. These electrostatic forces arise from a difference in electrical potential between the static and the suspended part of the CD actuator. Such as depicted in Figure 2.2.

When applying an electrostatic potential, the forces that arise can be described using the following formulae.

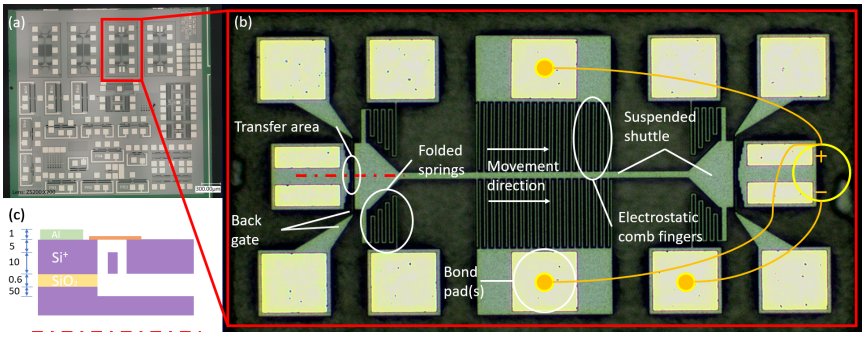

Figure 2.1: (a) Image of full MEMS die. (b) Closeup of MEMS device used for mechanical straining of 2D materials. All main features are indicated as well as the electrical connections are indicated. Some features are repetitive and have for simplicity only been indicated once. (c) Schematic cross-section of transfer area, dimensions in μm.

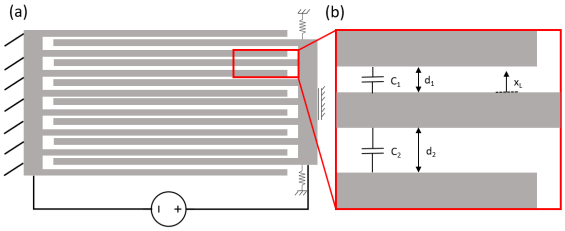

Figure 2.2: Schematic illustration of the working principle of the asymmetrically designed CD actuator.

$$F_e = -\frac{\partial U}{\partial d} \tag{2.1}$$

Where U denotes the electrostatic potential energy between the capacitive fingers. Fringing field effects are initially neglected as these terms are expected to be rather small compared to the parallel plate capacitance. U then becomes.

$$U = \frac{1}{2}CV^2 = \frac{1}{2}\frac{nA\epsilon_0}{d}V^2 \tag{2.2}$$

C represents the capacitance which is comprised of the number of fingers ($n = 38$), the overlapping area between the fingers ($A = 1.5\text{e}{-9}\,\text{m}^2$), the permittivity of vacuum ($\epsilon_0 = 8.854\text{e}{-12}\,\text{Fm}^{-1}$), the gap distance ($d_1 = 2\text{e}{-6}\,\text{m}\&d_2 = 4\text{e}{-6}\,\text{m}$) and the potential difference (V in Volts). Substituting Eq. 2.2 into 2.1 then yields.

$$F_e = \sum_{i=1}^{2} F_{e,1} = F_{e,1} + F_{e,2} \tag{2.3}$$

$$F_{e,1}\hat{\boldsymbol{i}} = \frac{\partial U_1}{\partial d} = -\frac{\partial}{\partial(d_1 - x_L)}\frac{nA\epsilon_0}{2(d_1 - x_L)}V^2 = \frac{nA\epsilon_0}{2(d_1 - x_L)^2}V^2 \tag{2.4}$$

$$F_{e,2} - \hat{\boldsymbol{i}} = \frac{\partial U_2}{\partial d} = -\frac{\partial}{\partial(d_2 + x_L)}\frac{nA\epsilon_0}{2(d_2 + x_L)}V^2 = \frac{nA\epsilon_0}{2(d_2 + x_L)^2}V^2 \tag{2.5}$$

$$F_e(V, x_L)\hat{\boldsymbol{i}} = \left(\frac{nA\epsilon_0}{2(d_1 - x_L)^2} - \frac{nA\epsilon_0}{2(d_2 + x_L)^2}\right)V^2 = \frac{nA\epsilon_0(d_2^2 + 2x_L(d_1 + d_2) - d_1^2)}{2(d1 - x_L)^2(d_2 + x_L)^2}V^2 \tag{2.6}$$

Such that x_L denotes the displacement of the CD as defined in Figure 2.2.

In order to determine the displacement of the CD actuator, it is necessary to know the stiffness of the system. The stiffness can be determined analytically using a series of back-of-the-envelope (BotE) calculations for beam deflections. Making use of the assumption that only the beams perpendicular to F_e deflect. This is a particularly valid assumption because of the (over)constraining of the suspended CD actuator, which permits it to only translate in one direction ($\hat{\boldsymbol{i}}$). A schematic overview of the situation is depicted in Figure 2.3.

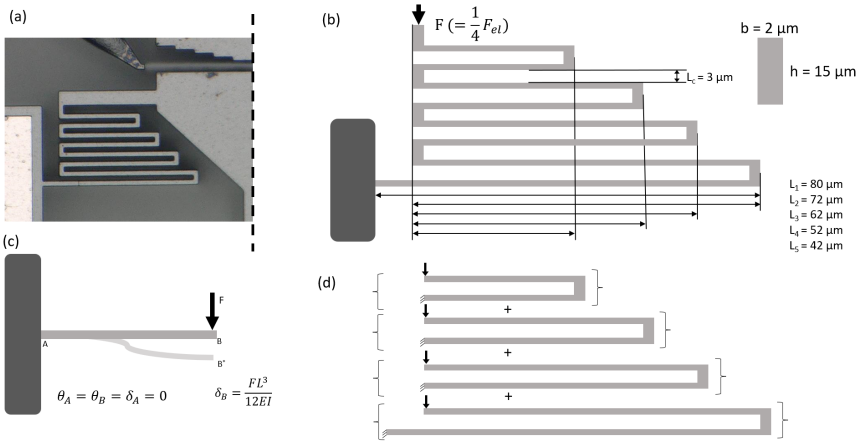

Figure 2.3: (a-b) Optical image and schematic of one of the four folded beam flexures. (c-d) Beam-deflection representation and assumptions to determine stiffness.

With a schematic description of the system, its stiffness in desired directions can be determined. The suspended shuttle is connected to four identical folded-beam flexures as depicted in Figures 2.1&2.3. Where each of the folded-beam flexures can be subdivided into another 4 springs (Figure 2.3(d)). Making use of the over-constraining assumption mentioned, the displacement of one such sub-flexure can be expressed by.

$$\delta x = \frac{F\,l_c}{A\,E} + \frac{F\,{l_{l1}}^3}{12\,E\,I} + \frac{F\,{l_{l2}}^3}{12\,E\,I} \tag{2.7}$$

Which can be rewritten to express stiffness $k = F/x$.

$$k_{subflexure} \frac{12\,A\,E\,I}{A\,{l_{l1}}^3 + A\,{l_{l2}}^3 + 12\,I\,l_c} \tag{2.8}$$

Where $A = bh = 3\text{e}{-11}\,\text{m}^2$ is the cross-sectional area of the beams which is identical everywhere, $E = 160\,\text{GPa}$ is the Young's modulus of the silicon, $I = \frac{hb^3}{12}$ is the area moment of inertia of a beam cross-section here the beam is flexed in its 'weak' direction such that h & b correspond to the dimensions as depicted in Figure 2.3 (b). $l_{l,1}$&$l_{l,2}$ Are the length of the long sides of one flexure and l_c that of the short connecting piece. Since the force in all these four sub-flexures is equal, their displacements add up which connects them as springs in series. Thus yielding a total stiffness for one of the 4 folded-beam flexures to be.

$$k_{flexure} = (\frac{1}{k_{sub,1}} + \frac{1}{k_{sub,2}} + \frac{1}{k_{sub,3}} + \frac{1}{k_{sub,4}})^{-1} \tag{2.9}$$

The values for each of said sub-flexures are given in Table 2.1 which yields a total stiffness for one flexure to be $k_{flexure} \approx 10.72\,\text{N/m}$. Now the total stiffness of the MEMS

Subflexure stiffness	$l_{l,1}$ [μm]	$l_{l,2}$ [μm]	l_c [μm]	$\approx$ Stiffness value [N/m]
$k_{sub,1}$	42	42	3	129.6
$k_{sub,2}$	52	52	3	68.3
$k_{sub,3}$	62	62	3	40.3
$k_{sub,4}$	80	72	3	21.7

Table 2.1: Values for the sub-flexure stiffnesses within each of the four main flexures.

actuator can be found by adding the stiffness of these four flexures. Two flexures are in tension and two are in compression but they all add to the stiffness hence they can be added as parallel springs such that.

$$k_{total} = k_{mems} = 4k_{flexure} \approx 42.9\,\mathrm{N/m} \tag{2.10}$$

To validate these calculations, a numerical simulation of the physics was done in COMSOL. An illustration of this model is depicted in Figure 2.4. The results of these simulations are presented in Section 3.2 and discussed in 4.3.

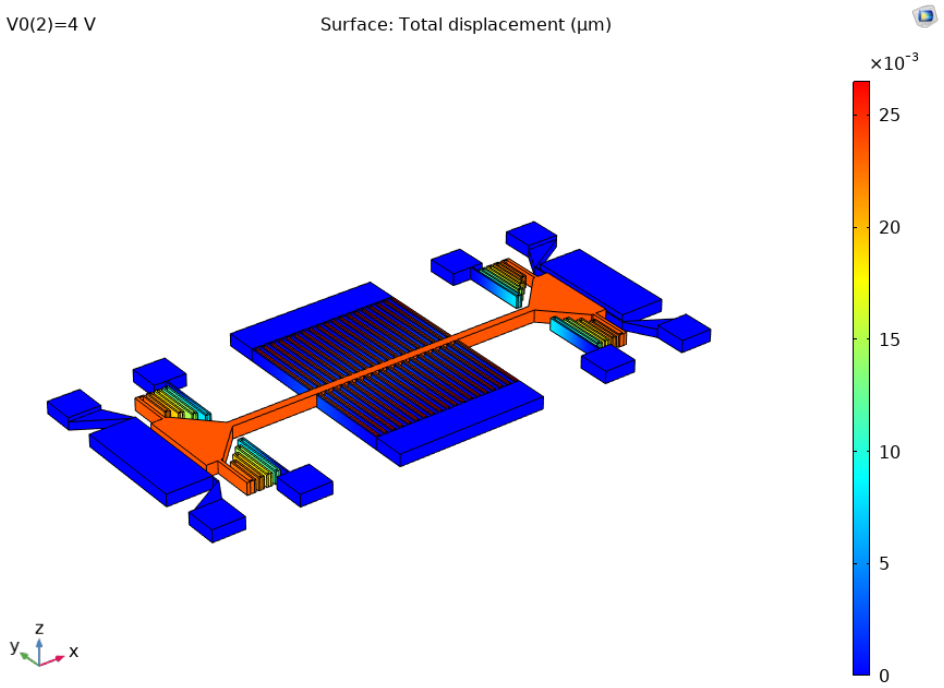

Figure 2.4: Visual schematic of deformation in numerical simulation software COMSOL of MEMS device subject to small electrostatic potential (4V).

2.1.2. Fabrication of MEMS device

The fabrication of the MEMS device has been outsourced to a company named "X-FAB Silicon Foundries SE" or "X-FAB" for short. They have high competence in manufacturing silicon wafers, from consumer to industrial demands and anything in between. The fabrication of this particular MEMS device follows from a series of DRIE (Deep Reactive-Ion Etching) steps to shape the MEMS device which is fusion-bonded on a cavity-SOI wafer. This particular bonding step allows for full control over the cavity geometry as well as optional deposition of contact metal layers on the top and bottom of the device-wafer. This process they name "XMB10", has some other benefits such as low para-

sitic capacitances, recessed z-direction elements and low atmospheric pressure around the device if there would be a top-cap wafer glass-frit bonded. The latter two of which remain unutilized within this project. Therefore a simplified version of the "XMB10" process can be summarised as depicted in Figure 2.5

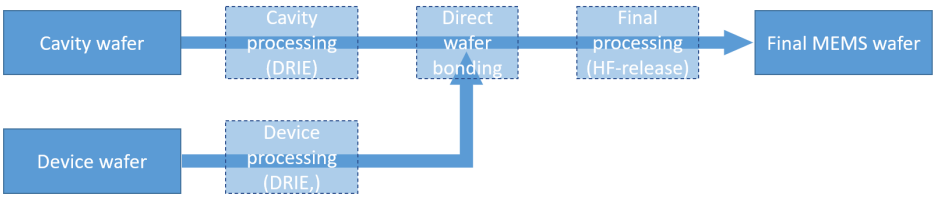

Figure 2.5: Simplified version of a 2-wafer process used to fabricate the MEMS devices of this project.

2.1.3. Fabrication of graphene

The fabrication of graphene follows a generic exfoliation procedure commonly referred to as the "scotch-tape method" [40]. In this method, a piece of large crystal graphite is stuck to a piece of scotch tape (type Magic™) and removed. From the relatively strong adhesion to the tape, some layers can be exfoliated (peeled) from the crystal. The number of layers is likely to be too large to be considered graphene after the first peel. To obtain a small number of layers, one can repeat the process by either folding the tape with the sticky sides to itself or putting a clean piece of sticky tape on itself and peeling that. If this process is repeated until the sheets of graphite peel atomically thin layers. After the exfoliation, the flakes can be deposited onto the desired substrate. Typically this is Si/SiO_x or a transfer polymer such as PDMS, PMMA or PPC.

Figure 2.6: Visible graphite on scotch-tape being exfoliated onto a silicon die as graphene. Image adapted From [111].

2.1.4. Transfer of graphene

With exfoliated graphene on the adhesive tape, it is now the task to transfer it to a transfer polymer. In this case, a polydimethylsiloxane (PDMS) stamp is used because of its transparency, weak adhesive properties, and short-term availability. The thickness of this stamp is around 2 mm on top of a regular microscope slide. Using this stamp to exfoliate graphene onto, is not the ideal method to obtain single-layer graphene since the optical contrast on the transparent stamp is minimal [7, 64]. If single-layered graphene were desirable, one could exfoliate the flakes onto a silicon with calibrated thickness of oxide and adjust the wavelength of the microscope light accordingly since the contrast depends on both these variables. Nevertheless, producing multi-layer graphene ($\pm$10 layers) is not an issue.

With the graphene stamp prepared, it can now be transferred to the MEMS device that strains the membrane whilst it is suspended. The most straight forward method, which is often used to transfer graphene onto flat surfaces or small cavities, is by stamping the PDMS stamp directly onto the desired location. Then slowly peeling off the stamp should leave behind the graphene on the target substrate. The geometry of the target

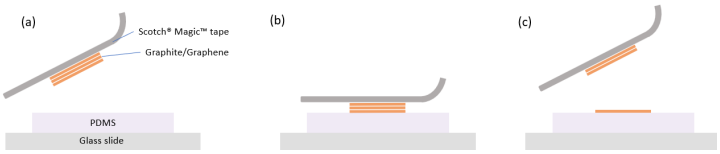

Figure 2.7: Schematic of the preparation of the PDMS stamp with graphene exfoliated onto it.

substrate plays a crucial role in whether the graphene sticks amongst many other parameters. Figure 2.8 indicates some of the common geometries this target substrate can have.

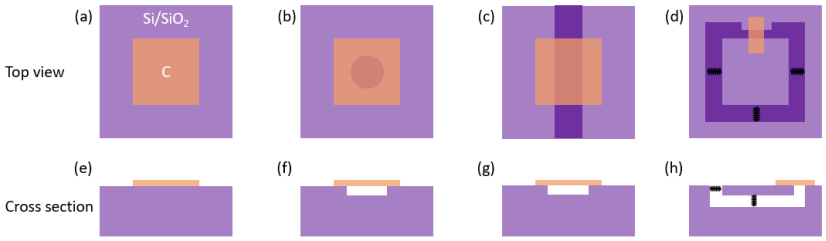

Figure 2.8: Schematic overview of different types of geometries the target substrate can have with increasing difficulty of graphene from left to right. (a) Bare silicon (b) Cavity (c) Trench (d) Suspended shuttle

Since the MEMS device has been fully fabricated before the integration of graphene and the device works like a tensile strain bench, the geometry that best describes the is that represented in Figure 2.8(d&h). Whilst attempting to stamp the graphene in place using the regular "all dry viscoelastic" stamping method [14], two main problems arose that led to the consistent failure of transferring graphene and other 2D materials. These problems are elaborated on in Section 2.2. In order to circumvent these issues, a new method to transfer graphene onto such delicate substrates has been discovered. This method shares similarities to methods such as has been recently described by Kinoshita et al. [64] in the choice of transfer polymer, poly-propylene carbonate (PPC). This transfer method has two key features that separate it from ordinary stamping methods [14, 54, 64, 96, 103, 117, 102].

1. The geometry of the stamp is dome-like by curing a droplet of PDMS on a microscope slide. This allows for a minimal contact area between the MEMS device, which prevents contamination to other devices on the chip. Therefore allowing to place multiple flakes on different devices on a single chip simultaneously.

2. The transfer stamp is covered with a film of another transfer polymer. To deposit the graphene, this polymer is locally melted on the tip of the stamp such that it releases itself from the stamp and is transferred on top of the graphene. To dispose of this unwanted polymer it is annealed in a vacuum oven.

The transfer process itself can be separated into three phases. The first step is to prepare the transfer stamp. This is done by dissolving pellets of PPC ($[CH(CH_3)CH_2OCO_2]_n$) into anisole (C_7H_8O) with a 15/85 weight ratio. Anisole was chosen as it is one of the less reactive and thus safe solvents. It was found that assistance from a hotplate at 50°C and a magnetic stirrer reduces the dissolving time to about 2 hours for a batch of 15 ml which suffices for about 30 films. A droplet of the solution is placed on an ultrasonically cleaned microscope coverslip (in two successive baths of acetone and isopropanol alcohol (IPA)). This is then spin-coated on the slip to create the film. This film is left to aerate such that the anisole evaporates. Using similar sticky tape as used for graphene exfoliation, this film can be transferred onto the microscope slide with a PDMS ($[C_2H_6OSi]_n$) dome. This process is schematically illustrated in Figure 2.9.

Having now the graphene flakes and the transfer stamp prepared, it is now possible to

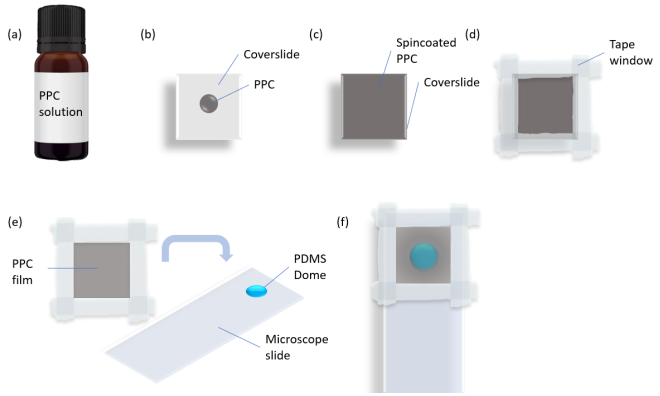

Figure 2.9: Preparation of transfer-stamp. (a-c) PPC dissolved in 85% anisole by weight is spin-coated on a microscope coverslip. (d-f) Using a window of sticky tape, the film can be peeled from the coverslip and placed on a dome of PDMS.

transfer the graphene onto the MEMS device. This is done by first picking the flake from the PDMS substrate on which it was exfoliated. Since the PPC films tend to stick to the graphene stronger than the PDMS, the pickup process yields a high success rate ($\approx$ 95%). Because of the dome-shaped transfer stamp, there is an initial contact point which spreads radially outwards when more contact pressure is applied. It was found that in order to have more control over the speed of the coming into- and releasing contact, the flake should be positioned slightly away from this initial contact point. Bringing the transfer stamp into contact with the flake and subsequently slowly releasing it in the described manner, the flake should now be on the transfer stamp. The flake can now be positioned above the desired location on the MEMS device. The MEMS device is subsequently heated to about 105°C from a hotplate underneath. This temperature is chosen because it is well beyond the glass-transition temperature of PPC [87]. The result of this is that the film on the transfer stamp becomes almost fluid-like within the contact area and adhesion to the MEMS device is favoured. Retracting the transfer stamp now results in a separation of the film such that the contact area stays on the MEMS device along with the graphene. This process is illustrated in Figure 2.10. More details about the transfer and the setup used to accomplish this can be found in Appendix B.

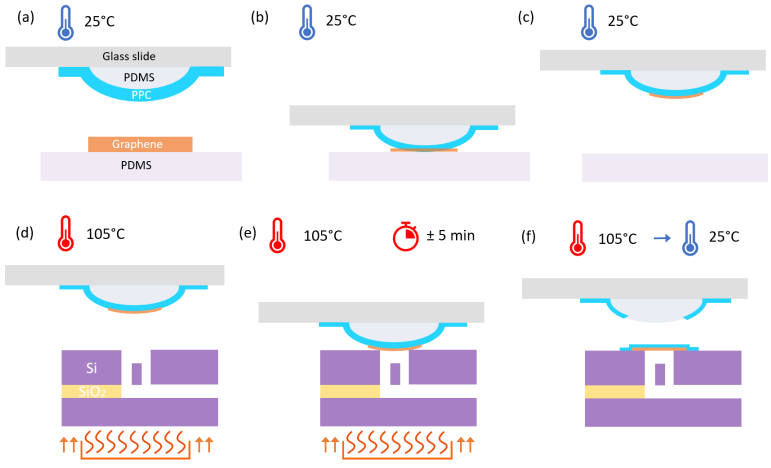

Figure 2.10: Transfer of exfoliated graphene flake onto MEMS device. (a-c) The transfer stamp is brought into contact with graphene and is able to peel it from the PDMS. (d-f) Graphene flake is brought into contact with a (pre) heated MEMS device such that the PPC film locally melts and stays on the MEMS device when the stamp is retracted.

Since the desired material is transferred along with a part of the PPC film, a post-processing

step is required to remove this polymer. That step is the annealing of the MEMS device such that the polymer is removed. Conveniently enough, the highest reported value for the thermal decomposition of PPC (278°C [76]) is well below that of any other material on the MEMS device when graphene is considered as the material to be strained. The annealing is performed in absence of oxygen by first drawing a vacuum of about 1e−6 mbar. Subsequently, a small flow of argon gas (Ar) is provided to prevent the creation of carbon byproducts from the residual polymer that can react with oxygen to produce e.g. amorphous carbon [1, 73, 100]. Alternatively, the flow of Ar during heating can be shut off completely, since the main requirement is the absence of oxygen molecules to the polymer. In this scenario, a much higher level of vacuum can be obtained (≈ 1e−7 mbar) and less Ar is used, making the process cheaper. The difference in the scenario where no Ar flow is provided during the heating, is that the decomposed polymer is not being flushed away as effectively. This results possibly in the polymer depositing onto the quartz vacuum tube and reappearing in the experiments of another user. Both scenarios have proven successful, although the former (Ar flow during heating) is thought to be better for the annealing setup.

The annealing process is schematically depicted in Figure 2.11. This fabrication step is particularly advantageous because the transfer or graphene using polymers is often accompanied by some contamination from that polymer [13, 35]. Although such contaminations are often not visible using standard optical inspection methods. These contaminations are likely to cause imperfectnesses to the membrane such as wrinkles, cracks and folds [77]. A more realistic representation of this process can be found in Appendix B Figure B.4. After exposing the device to a temperature of about 300°C for an hour, the PPC is not visible anymore with an optical microscope. Although this indicates a successful removal of the PPC, there could be still extremely tiny contaminations [12, 77]. If there would be any, their effect on the dynamics of the membrane is neglected.

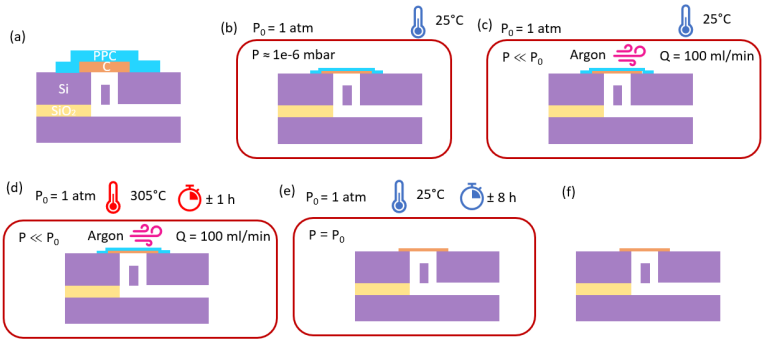

Figure 2.11: Annealing of MEMS device to remove PPC. (a&b) The sample is subjected to a vacuum, indicated by the enclosure around the schematic. (c-e) The sample is heated for 1 hour in presence of a vacuum with a small flow of argon gas and cooled back to room temperature. (f) The sample is removed from the vacuum.

2.1.5. Post-processing of MEMS device

With the annealing successful, there are three final steps required to complete the device. How the graphene sample is connected such that it can be actuated is portrayed in Figure 2.12

1. Fixation of the graphene flake onto the MEMS device such that it cannot slide.
2. Wirebonding the MEMS device dies to a chip carrier.
3. Connecting the chip carrier to a printed circuit board (PCB)

The first point is particularly important and greatly determines the boundary conditions of the dynamical system. As such, the clamping impacts observed mechanics. Unfortunately, this project has not produced a clamping procedure that is guaranteed

to be successful. Nevertheless, an effort was made to achieve this. The effort that has been made, as well as some initiatives that are worth trying in a future project, are described in Appendix F.

The second point is necessary to apply an electrostatic potential (V_{mems}) on the CD actuator. In the batch that is depicted in Figure 3.3, this procedure was expedited to Maurits Houmes. Using a TPT-HB05 wirebonder with Au wires the bonding was performed. First, using an arc, a ball is created which is then ultrasonically bonded onto the MEMS device. The other side of the wire is then drawn to the chip-carrier and bonded by a wedge bond. In Section 4.1 the effect of the bonding is further scrutinized.

The final step is to connect the chip-carrier to a PCB which can be mounted to the vacuum cube of the measurement setup. This PCB provides connections to which cables can be soldered. These cables have an SMA connection on one side and bare metal on the other side. The SMA cable has both positive and negative terminals such that only one throughput wire is required. On the other side of the vacuum enclosure, the SMA cable is converted to a BNC-type cable which can then be connected to a programmable power supply.

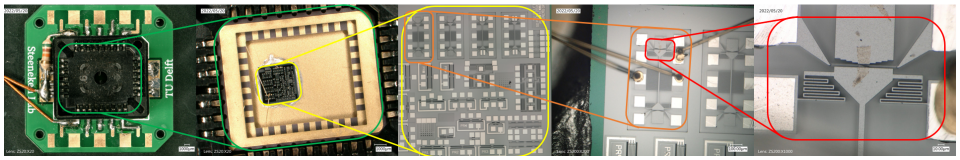

Figure 2.12: PCB to graphene sample illustrated as a series of close-ups.

As everything around the MEMS device is to be situated in a vacuum environment, there are certain extra precautions that need to be made to prevent outgassing. First of all, if anything is touched by bare hands, such as the PCB, it shall be washed with isopropanol-alcohol (IPA). The SMA cable that is soldered on the PCB is shielded by Kapton instead of some regular polymer shielding. The soldering itself only uses minimal flux where it is absolutely necessary and solders are properly cleaned with IPA to remove any excess flux.

2.2. Transfer failure analysis

It has taken great effort to optimize the process of depositing graphene onto the MEMS device. In the following subsections, some of the main attempts to solve the poor adhesion between graphene and SiO_2 are elaborated on. The unsuccessful transfer attempts have two root causes; peeling and poor adhesion.

The former problem is caused by the deformation of the MEMS device during the graphene stamping.

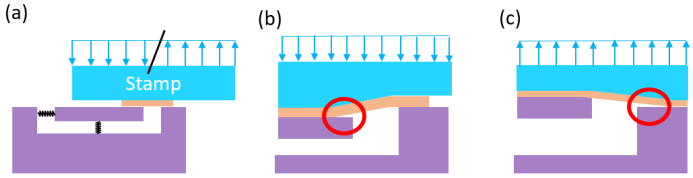

Figure 2.13: Indication (red circles) of the peeling problem graphene exhibits on the target substrate at hand which deflects vertically and laterally.

As depicted in Figure 2.13, a problem occurs due to the deflecting of the suspended side of the transfer area. When stamping any 2D material in this region, the shuttle deflects downwards, therefore, creating a peeling area around the edge as indicated in 2.13(b). When moving the stamp away from the substrate, the opposite side of the flake w.r.t. the transfer area starts to peel, such as indicated in 2.13(c).

The latter problem is a result of the fabrication process of the MEMS device as described in Section 2.1.2. The finished MEMS device has a good surface finish in the out-of-plane dimensions, which is good for electrostatic functionality. But on the in-plane dimension (on the top surface), little effort is made to ensure a smooth top surface. Resulting in great surface roughness. Therefore, whilst stamping a material, only very little effective contact area is created. Professor Steeneken hypothesised that this might be an anti-sticktion coating of some kind. Regardless, the total van der Waals interaction force is insufficient such that adhesion to the stamp dominates, resulting in a failing transfer. This effect is illustrated in Figure 2.14. The analysis of the roughness is presented in Appendix A

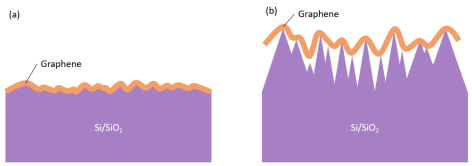

Figure 2.14: Comparison of (a) a smooth silicon surface resulting in a large contact area with transferred material. To (b) a rough silicon surface resulting in areas of non-contact.

The following sections will elaborate on some of the main attempts that have been made to circumvent these issues and ultimately fabricate the MEMS device with incorporated graphene.

2.2.1. Plasma cleaning

In an attempt to stimulate adhesion between the SiO_2 of the MEMS device and the graphene, it was hypothesised that a treatment of cold oxygen plasma could help. The plasma serves two purposes in this context.

1. Clean the surface of contaminants of nanoscopic size.
2. Alter the hydrophobicity of the surface layer.

Regarding the first purpose, it is well-established that exposing a substrate (silicon, glass, polymers etc.) to a plasma of a noble gas e.g. Ar results in a microscopic version of a sand-blasting process. The kinetic energy given to the ions is able to chip away very tiny contaminations that resist chemical cleaning. In the situation at hand. However, a plasma of O_2 is used which has an additional cleaning mechanism. Due to the oxygen radicals being formed in the plasma, reactions take place with hydrocarbon residues on the surface from e.g. releasing agents [109]. This process is illustrated in Figure 2.15.

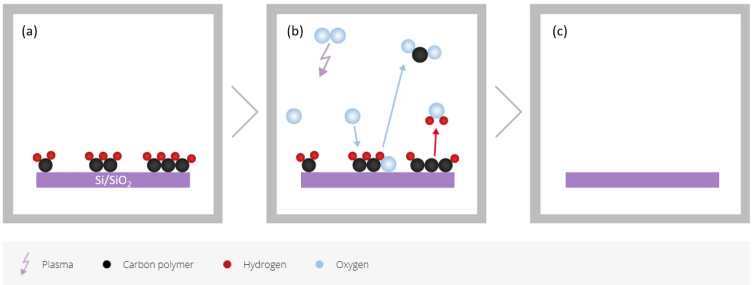

Figure 2.15: Schematic of oxygen plasma removing surface hydrocarbons from silicon surface [31].

The second purpose of the plasma is to alter the wettable properties of the surface. Substances with low surface energy are able to wet those with high surface energy, but not vice versa. Increasing the surface energy by means of plasma activation can possibly lead to better adhesion between graphene and MEMS. Unfortunately, this activition is highly unstable for metals and therefore lasts in the order of minutes [58].

2.2.2. Vapor HF etching

Another sequential attempt to promote adhesion between the membrane and MEMS device was to reduce the surface roughness. The idea behind this is that the membrane, despite extremely low bending rigidity, would be better able to conform to the surface profile of the MEMS device. Which would increase adhesion area and thus the total adhesion force [8]. A buffered oxide etch (BOE), in this case with hydrofluoric acid vapour (HF), reacts with the SiO_2 layer and etches it away. The idea is sketched in Figure 2.16.

$$SiO_2 + 4\,HF \longrightarrow SiF_4(g) + 2\,H_2O \tag{2.11}$$

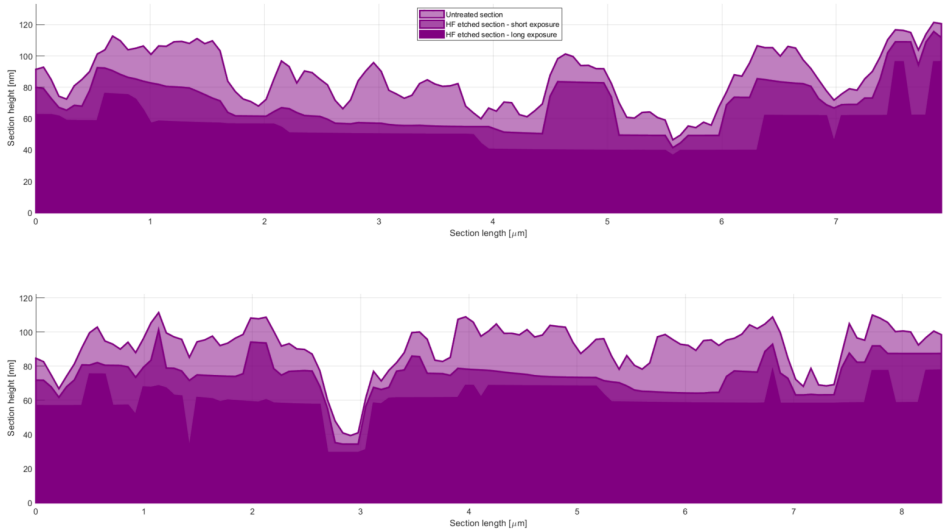

Figure 2.16: Simulation on raw AFM data indicating how a VHF treatment would alter surface roughness of SiO_2 for two different profile lines. Darker purple indicates a longer exposure time.

In practice however, there are many variables that the final result depends on. The VHF process was performed by Roberto Pezone MSc. Since the oxide layer is etched, the effectiveness of the process depends on the thickness hereof. The device is very fragile as it contains structures already suspended. This in combination with the aluminium bond pads being present eliminates the option of thermal oxidation. It was therefore attempted to oxidize the surface in a "cold plasma" as described in Section 2.2.1 [3, 61]. Unfortunately, even at prolonged plasma (3 hours) exposure, no significant increase in oxide thickness could be observed rendering the etching process unsuccessful.

2.2.3. Gold coating

In contrast to smoothing the surface by subtractive processes like VHF etching as described in Section 2.2.2, it is also an option to add material. The additive process in question is electron-beam (E-beam) evaporation. Here the to-be-deposited metal is evaporated in the vicinity of the target substrate and should deposit on it in an almost laminar fashion since the evaporation occurs from a point source. Unfortunately, this process has also turned out not to yield the desired improvements in roughness. A more in-depth analysis is given in Appendix A.

2.2.4. HMDS coating

Another method that was mentioned in the literature to improve the adhesive force between the membrane and SiO_2 is to coat the device in a monolayer of hexamethyldisilazane (HMDS). This material can form what is known as a self-assembled monolayer (SAM). In the case of SiO_2, which is present at the surface of the device a certain reaction takes place when the volatile liquid HMDS is placed in the presence of the device. Here the SiO_2 at the surface reacts with the $[(CH_3)_3Si]_2NH$ to form a surface of which

the CH_3 groups perturb [6]. This effectively lowers the surface tension and makes the surface more hydrophobic. This is in the case of graphene favourable, as graphene is also hydrophobic of nature when it is of multilayer thickness [63]. In some literature works where graphene transfer was problematic, it was said that: "This surface treatment makes the graphene transfer very easy" [14]. This increased surface adhesion should in theory also have other benefits for other applications such as for graphene-field-effect transistors by also limiting hysteresis [92]. The coating was done in a similar method as prescribed by Semicon manufacturer supplier MicroChemicals®. This process is (almost) depicted in Figure 2.17. The chemical lab where this process was performed did not have a bubbler. Upon discussion with A. Sharaf (PhD candidate) and A. van Bogaard (lab technician), it was concluded that this should not pose a problem as the NH group of the HMDS should be able to separate itself with the N_2 that is present in the air.

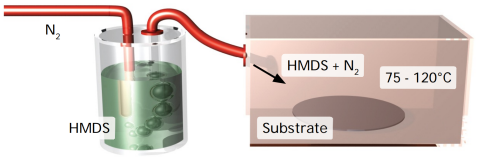

Figure 2.17: Render of the HMDS coating process. Image adapted from [41].

Unfortunately, the regular transfer methods (all-dry viscoelastic stamping/PPC stamping without melting PPC) remained unsuccessful. It could be observed that the surface adhesion of the membrane to the device remained insufficient. Had the surface been not as rough, the effect of this coating would likely be more noticeable due to an increased effective surface area.

2.2.5. Wet transfer techniques

Another branch of methods described in the literature are the wet transfer methods. These methods can vary but have the same basic principle involving water or some other solvent in which typically the target substrate is submerged. The membrane is set afloat on this medium. To do this, some sort of handling polymer is typically required. This can then be aligned to the target substrate, to get the membrane in contact with the substrate, the liquid can be pumped out, or the substrate can be brought upwards [29, 77, 82, 96, 117].

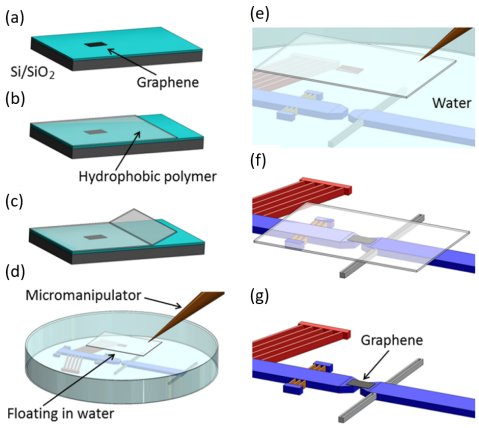

Figure 2.18: General wet transfer procedure adapter from [86]. (a) Graphene is produced onto a surface by e.g. mechanical exfoliation or CVD growth. (b) The membrane is covered in a type of hydrophobic polymer such as PMMA. (c) The membrane with the coating is wedged either chemically with a sacrificial layer underneath the graphene [42], or mechanically as presented in this figure. (d) The membrane is now set afloat on a liquid medium such as DI water with the target substrate submerged in it. (e-f) The membrane and substrate are aligned and brought towards each other. (g) transfer polymer is dissolved (e.g. uncrosslinked PMMA in acetone), then the device can be removed from the solvent by CPD if necessary [11, 10].

There exist many variants within the realm of wet transfer techniques, despite that there is one major issue regarding this project, surface tension. In most of the works using wet transfer techniques, there is no fragile MEMS device. If there is a MEMS device involved, it is typically not suspended (yet) at the moment of membrane transfer since the stresses caused by forces from surface tension can likely damage tiny fragile structures[43, 85]. In this project, the device fabrication had already been performed and thus there exist suspended, fragile structures. The surface tension of the liquid upon evaporation/removal tends to pull the electrostatic comb fingers towards each other. When this happens, the flake is severely strained (up to 33% which would result in fracture or major slip) *and* the fingers become stuck as shown in Figure E.1. A theoretical way to circumvent this would be by critical point drying (CPD) [122].

2.3. Experimental setup

The setup used to measure the dynamics of the membrane is in principle an interferometric measurement setup that uses two lasers. One for interferometry and one for optomechanical actuation. This setup is doped the "Enigma" and shall be explored in this section.

2.3.1. Obtaining data

With the suspended membrane device now ready to be strained, a method to drive and measure the membrane motion in the out-of-plane direction is required. There exist several methods to do so such as transconductive, capacitive- or optical (interferometric) readout [105]. Since the device at hand provides mechanical strain, there should be no need for another way to induce tension, for example by electrostatic tensioning. The method in this work uses an optical position-dependent readout and actuation scheme. As such, the dynamics will be probed by two different laser beams a red Helium-Neon ($\lambda = 632.8\,\text{nm}$) and blue diode ($\lambda = 405\,\text{nm}$), for readout and actuation respectively. A schematic of the setup is shown in Figure 2.19.

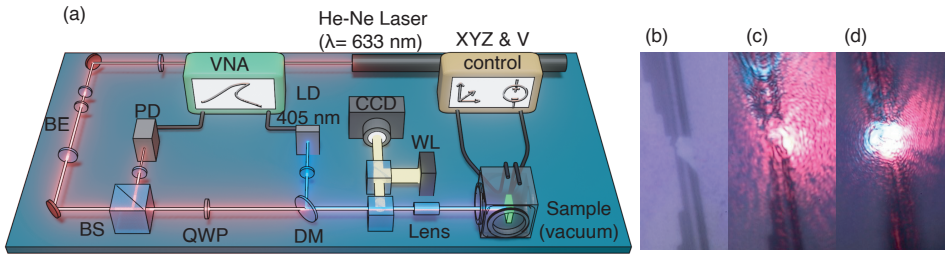

Figure 2.19: (a) 3D render of Fabry-Pérot interferometric setup. A red He−Ne $\lambda = 632.8\,\text{nm}$ is expanded through a beam expander (BE) and polarized through a quarter wave plate (QWP). Another laser diode projects a blue laser which is added into the path of the red laser through a dichroic mirror (DM). Lastly, white light (WL) is added to this path of the lasers. Through a lens, the laser bundle is focused on the membrane and interferes in the cavity formed by the membrane and the cavity bottom. The returning red is directed into a photodetector (PD). The blue laser stop at the red-pass filter in front of the PD. Part of the total beam bundle is redirected into a charge-coupled device (CCD) which allows for visual alignment of the device w.r.t. the lasers. (b) A membrane as viewed from the CCD. (c) The red laser on the membrane. (d) Red- and blue lasers are shone onto the membrane and brought into proper focus.

As shown, there are two main optical paths to follow, for the red and blue laser (RL and BL) respectively. In reality, there is another optical path into which an unfocused beam of white light is added to the laser beams. The reflections are caught by a camera sensor to obtain an optical image of the system which is required to position and align the sample w.r.t. the lasers. This optical path is neglected in the analysis as it is arbitrary and does not influence the measurements. The fundamental working principle is based on a Fabry-Pérot interferometer. The suspended membrane and the cavity surface form something similar to a Fabry-Pérot etalon. In this cavity interference of the RL with itself occurs as it reflects back from the cavity bottom. Depending on the depth of the cavity, this interference can be positive/negative or weak/strong. The membrane's out-

of-plane motion modulates the effective depth of the cavity and therefore the strength of the measured signal. If this signal is evaluated at many frequencies the experimental frequency response function (FRF) is obtained.

To achieve this, the path of both beams can be followed starting at the source (Figure 2.19(b)). The RL is directed through a beam expander (BE), which allows the for a smaller focus spot because it decreases the divergence, also it allows for easy gaussian filtering as this requires also a two-lens system. The beam then passively passes through a beam splitter (BS) and is circularly polarized by a quarter wave plate (QWP). The dichroic mirror (DM) has no effect on the RL beam. It is then focused on the cavity by a standard lens. At the cavity, it is reflected and interferes with itself which alters the intensity of the returning beam. The beam goes back through the lens, the DM, and the QWP and is this time reflected at the PBS into a photodiode (PD) to measure its intensity, which alters as a function of the membrane deflection.

In order to deflect the membrane in the out-of-plane direction, parametric excitation is employed. The parameter that is modulated is the (effective) stiffness of the membrane. By focusing a more powerful BL on the membrane the temperature can be increased. Due to the atomic thickness of these 2D material membranes, this can be done at extremely high frequencies. This laser has static and dynamic components such that.

$$P_{bl} = P_{bl,dc} + cos(\omega t) P_{bl,ac} \tag{2.12}$$

The static part ($P_{bl,dc}$) can be used to induce an extra pretension in membranes with negative thermal expansion coefficient, like graphene ($\alpha_{gr} \approx -7e{-}6\,K^{-1}$ at room temperature [98]) but mostly functions as an offset for the dynamic term ($P_{bl,ac}$) since the strain is exerted by the MEMS device. The beam is inserted into the system through the DM and filtered out by a red pass filter at the PD.

If now the outgoing signal of the BL is compared to the strength of the incoming signal of the RL for all frequencies, the FRF can be obtained. A single FRF as obtained by this setup is depicted in Figure 2.20.

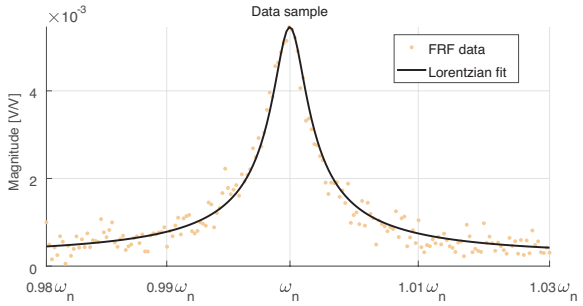

Figure 2.20: Data sample with depicted Lorentzian fit to extract the resonance frequency and quality factor

By fitting a Lorentzian/Cauchy function, the resonance frequency and quality factor can be obtained from the FRF.

$$L(\omega) = \frac{1}{\pi} \frac{\frac{1}{2}\Gamma}{(\omega - \omega_n)^2 + (\frac{1}{2}\Gamma)^2} \tag{2.13}$$

This function contains the fundamental frequency (ω_n) and a parameter specifying the width (Γ).

2.3.2. Calibration of data

Since the VNA only compares the frequency, phase and amplitude of both input and output signals, the results of the vibrational amplitude of the membrane are in relative units ([V/V]). There are many possible reasons to require the actual vibrational

amplitude, for example when deriving mechanical or thermal properties [74]. To calibrate the system such that the actual vibrational amplitude is known, there is the standard method of thermomechanical calibration [51]. For this method, the modal mass and temperature of the system are required. Obtaining the modal mass itself can be tricky as the influence of polymer contaminations can be very large [65, 13, 35]. However, this Fabry-Pérot interferometry setup allows another interesting method of calibration. Since the intensity of the reflected light is a periodic function of the membrane's position, that means that at high vibrational amplitudes of the membrane, the assumption of a linear transduction coefficient does not hold. This can be used advantageously towards calibration. It is possible to derive mathematical equations that relate the intensity ratios measured at the driving frequency and the next two harmonics ($\omega_{\text{measure}} = \omega_{\text{drive}}\&2\omega_{\text{drive}}\&3\omega_{\text{drive}}$), to the resonant amplitude and the cavity depth [34]. The VNA of the setup is described in Section 2.3 can perform heterodyne measurements (i.e. is capable of measuring these harmonics).

2.3.3. Practicalities

Having established the working principles of the transfer process, MEMS device and measurement setup, one will still encounter some practicalities that are to be tackled to obtain data. This section will present some of the main practicalities that should be understood if one wishes to reconstruct the experiments of this thesis.

Vacuum enclosures are used in two stages of the process. It is of great importance to make sure the enclosures as well as the pumps and connections stay performing up to specification. The first vacuum enclosure is found in the annealing setup. Which comprises two vacuum pumps (a pre-pump and a turbo-pump) and a long quartz tube. It is of great importance to minimize the contamination of these systems as much as possible. The first ritual to achieve this is by making sure the "boat" that holds the MEMS devices is handled in a fumehood with gloves. During transportation, it is held in a clean Petri dish. This "boat" is pushed into the tube with a clean, dust-free rod. The ritual happens during the annealing, where the sample is annealed under a slight flow of Argon (Ar) such that the decomposing polymer flushes into the gas outlet, rather than depositing onto the inside walls of the quartz tube.

For the interferometric setup doped as "Enigma", there is another vacuum environment in which the sample is loaded. The main precautions made here are to first of all handle everything with clean nitrile gloves. Secondly, the PCB that holds the chip carrier and device contains solder. This soldering has been done with minimal flux to prevent outgassing. After soldering, the device was ultrasonically cleaned in IPA to remove excess flux. The wires that connect the PCB to the outside world (to apply a voltage to the MEMS) are Kapton-covered wires since regular polymer-coated wires are known to outgas.

Automation of measurements is achieved by communicating with all involved equipment simultaneously through Matlab programming. This task is not too complicated there are only three devices that should be communicated with. The Attocube 3-DoF (x-y-z) stick-slip piezo position stage, the Rohde&Schwarz VNA and the Rigol programmable power supply. The process of doing so was the same for all three devices. First, a serial connection needs to be established. Their respective user manuals provided plenty of guidance to do so. The first two devices could be connected through a network hub and the power supply made this a licensed feature so had to be connected via USB. All devices could be talked to using SCPI commands which all have a clear (online) programming manual describing the available commands.

Alignment of the sample w.r.t. the optical path is achieved during measurements by the use of a 3-DoF (x, y & z) piezo stick-slip positioning stage that is enclosed in the vacuum environment. The remaining three DoF (R_x, R_y & R_z) can be tricky to align

adequately for a good interference signal. Until now, this was done by trial and error in positioning the Attocube vacuum enclosure. When the sample is in focus on the camera, some tilt can be seen usually on the back gate if sidewalls are visible. Adjusting the box adequately and refocusing the device to the optical path a couple of times typically tends to be sufficient to observe the resonance of the membrane. Once the alignment is satisfactory the Attocube can be clamped in place using a custom clamp made by me. This is to prevent the Attocube from drifting due to vibrations coming from the vacuum pump. Internally, the stick-slip piezos possess a feedback loop that can be switched on such that the piezo actuators themselves also remain aligned.

3

Results

The process of developping a method to transfer graphene (or other thermally stable 2D materials) onto the supplied MEMS devices has turned out to be a great challenge. Hence, the timeline of this project was shifted a bit. The main investigation of graphene dynamics was therefore done on a single device, as encircled in green in Figure 3.1. Keep in mind that the flake has been unclamped (only by van der Waals forces) which poses a great uncertainty on the boundary condition that there is no slippage. The following chapter presents the main experimental observations.

3.1. Graphene transfer

With the newly discovered transfer method as described in Chapter 2.1, two batches of MEMS devices with graphene were fabricated. After depositing the graphene onto the device, there was a substantial amount of PPC residue which can be seen in Figure 3.1. Despite the polymer residue, it is observed that the material has been deposited with adequate accuracy. The success rate of depositing the membranes using this method is estimated at 80%.

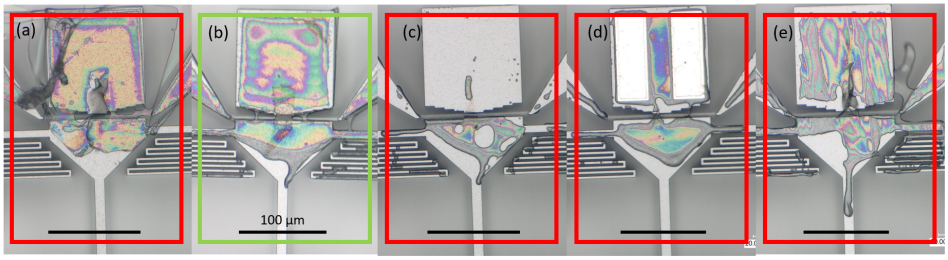

Figure 3.1: (a-e) MEMS devices post-transfer with deposited graphene and PPC residue. All scale bars are 100 μm

By virtue of the high thermal stability of graphene, the possibility to anneal the PPC arises. The bottleneck in this case would be the aluminium bond-pads that are present on the MEMS device. Conveniently enough, the highest reported thermal decomposition temperature of PPC reported in the literature is well below that of aluminium ($T_{td,PPC} = 278\,^{\circ}\mathrm{C}$) [76]. As follows from Figure 3.2, there is no charring of any kind and the PPC has been completely removed visually. The success rate of annealing the membranes is estimated to be 100%.

The final step to complete the MEMS device is to wire-bond the device so an external voltage can be applied. Although undesired, the wire-bonding had an effect on the flakes. Figure 3.3 shows how this process step alters the surface profile of the membrane.

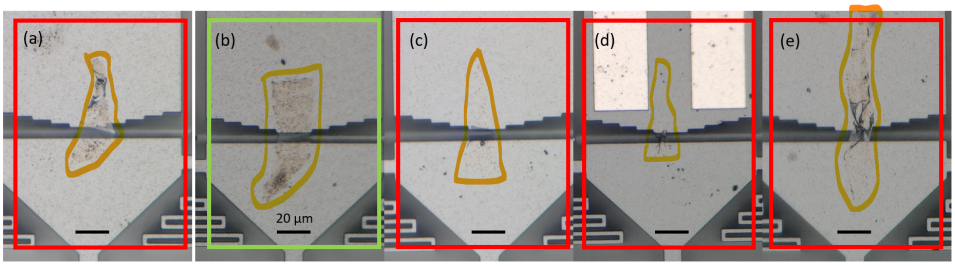

Figure 3.2: (a-e) MEMS devices post-anealing with deposited graphene. The graphene location is indicated by an orange enclosure. All scale bars are 20 μm

As can be observed, 1/5 membranes had ripped and the other 4/5 showed a change in morphology. The changes in surface morphology are highly undesirable as they most likely originate from slippage of the membrane which reduces pretension. Currently, the bottleneck of device manufacturing is therefore the wire-bonding process. A more detailed analysis of this failure mechanism is given in Section 4.1.

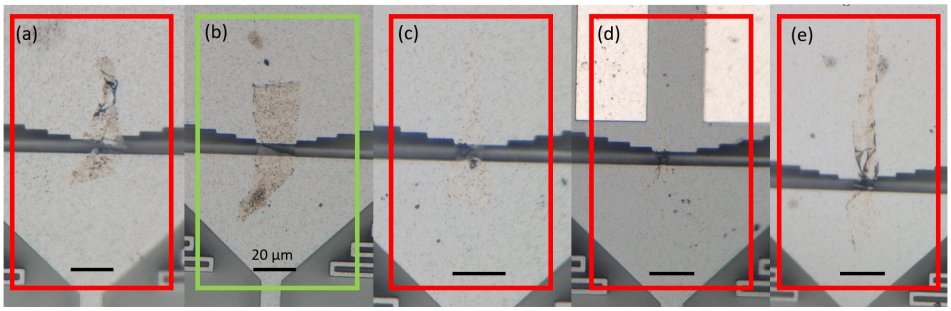

Figure 3.3: (a-e) MEMS devices post-wirebonding with deposited graphene. All scale bars are 20 μm

3.2. Stiffness simulation

In the design phase of this MEMS device, COMSOL was used to study the electromechanical- and vibrational behaviour of the device. For example, the modeshapes and corresponding Eigenfrequencies of the CD actuator can be simulated. This was done by a colleague and is described in his thesis [52]. Another important behaviour which was simulated was the voltage-deflection behaviour of the CD actuator. This is important since it determines the operating range of the voltage that can be applied across the CD actuator. This numerical simulation yielded a result that was somewhat counterintuitive for reasons as explained in Chapter 4.3, a bifurcation in the equilibrium position of the CD was expected but not obtained. This gave rise to the desire for a model that better describes the expected behaviour. For comparable MEMS devices, it is a well-known phenomenon that electrostatic softening occurs which leads to the so-called "pull-in" where the electrostatic softening dominates the stiffness so much the total stiffness turns negative which results in the snapping of fixed and movable CD fingers to one another. At this scale, van-der-Waals forces are typically larger than those in the flexures resulting in a MEMS device that is dysfunctional. "Pull-in" is thus to be prevented. To confirm this suspicion, an analytical model of the MEMS actuator is proposed using the equations presented in Section 2.1.1. Comparing this analysis to the numerical simulation is presented in the following Figure 3.4, where the analytical solution is displayed in orange and the numerical simulation discrete black circles.

A clear initial agreement between the analytical and numerical (COMSOL) simulation can be observed but after a certain voltage, the results deviate. The analytical solution shows the expected pull-in voltage and the numerical solution does not. A more detailed investigation of this result is given in Section 4.3.

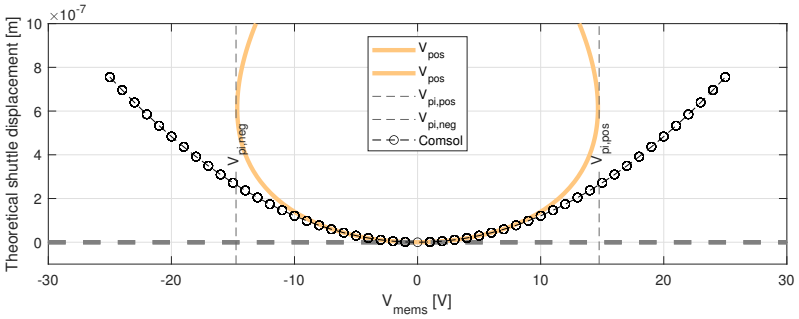

Figure 3.4: Comparison of COMSOL simulation (black) to the analytical solution (orange) of the voltage-deflection curve of the CD actuator. V_{pi} indicates the analytically obtained pull-in voltage

3.3. Linear dynamics experiments

Despite the final aim of this thesis being to investigate the effect of mechanical strain on the nonlinear dynamics, the linear dynamics show behaviour that is well worth analyzing. Understanding this acts as a good basis for interpreting the nonlinear behaviours later observed when the driving power is increased above a certain threshold. The results presented in this section correspond to the graphene sample as depicted in Figures 3.1,3.2,3.3 (b).

3.3.1. Frequency response

The frequency response of graphene resonators on the scale of this work (few μm's) starts to resonate around in the megahertz range [21]. This is orders of magnitude higher than the lowest resonance that was simulated and experimentally confirmed for the MEMS device attached to the membrane which is around 80 kHz [52]. Along with the observable fact that the mass of the suspended MEMS actuator is orders of magnitude greater than that of the resonating membrane, about 4.8e5 times. Given these two arguments, gives reason to assume that the interaction of the membrane modes towards actuator modes would be negligible.

The frequency response is measured using the setup described in Section 2.3. If the FRF for many different values of strain are plotted, the effect of the mechanical strain becomes apparent. This can be seen in Figure 3.5. Now there are three main behaviours observed.

Firstly, as the voltage starts to increase, the resonance frequency increases along. This effect is expected and already allows for the determination of the Young's modulus [93].

Secondly is the switching of an increasing ω_n to a decreasing ω_n after a certain voltage. Typically around $V_{\text{mems}} = 8\,\text{V}$, this is observed for the sample depicted in Figure 3.5.

Lastly, there is an observed hysteresis after performing a sweep up and back down in V_{mems}. This is apparent from two behaviours. Firstly, ω_n at $V_{\text{mems}} = 0\,\text{V}$ tends to drop after almost every experiment where the membrane is strained. Secondly, the up and down sweep of V_{mems} show a different path if the fundamental resonance frequency is followed. The possible cause of this hysteresis is further analysed in Section 4.4.1 and Appendices H and J.

3.3.2. Fitting the hardening behaviour

If the focus is now shifted to a single voltage sweep of these linearly resonating FRFs, some interesting effects can be noticed. An exemplary Vmems voltage sweep plotting the ω_n for all V_{mems} is given in Figure 3.6 (a).

The manner in which the voltage sweeps is described in Appendix E ($V_{\text{mems}} = 0 \rightarrow 13 \rightarrow 0 \rightarrow -13 \rightarrow 0\text{V}$). Therefore, if symmetry across the neutral voltage line is observed a couple of things can be concluded from this which are discussed in Section 4.4. This mea-

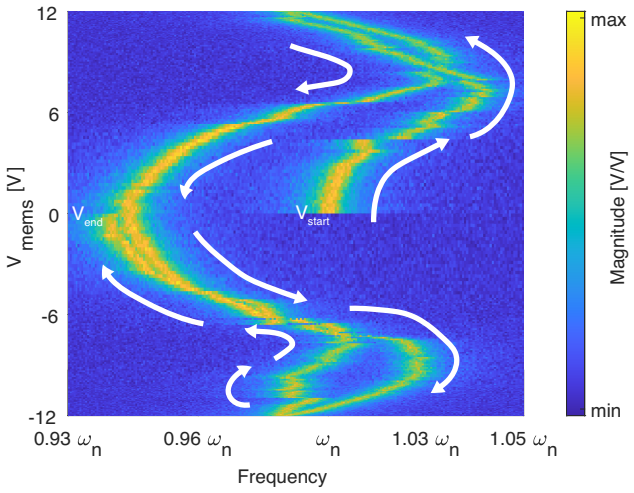

Figure 3.5: Frequency response of graphene flake that is being strained according to a voltage sweep that can be traced to the direction of the arrows.

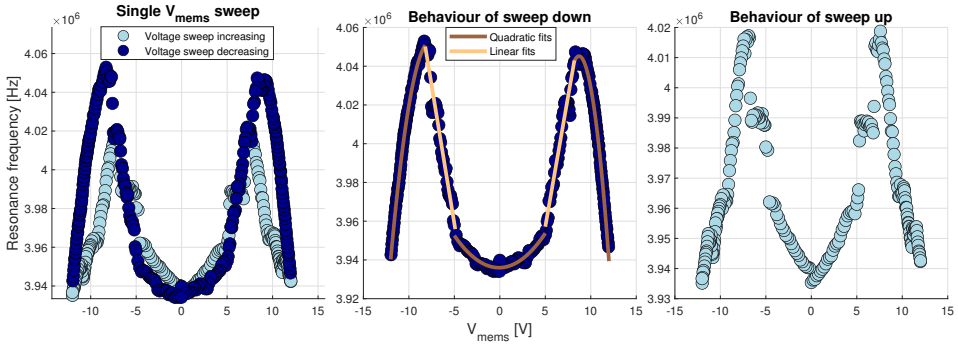

Figure 3.6: (a) Plot showing the resonance frequencies for the fitted linear FRFs for all V_{mems} values at $P_{blue} = -5\,\text{dBm}$. (b) Identification of linear and quadratic behaviour when the tension is released from the membrane, i.e. sweep down of V_{mems}. (c) Sweep up of V_{mems} for comparison. Note that the x and y axis are switched w.r.t. Figure 3.5.

surement was performed with quite some V_{mems} sweeps preceding it (≈ 15). Therefore most of the slipping has already occurred in the previous measurements such as the one depicted in Figure 3.5. The hysteresis observed in the measurement portrayed in Figure 3.6 is purely from straining and relaxing of the membrane. Despite the hysteresis, there is a remarkable behaviour that can be observed during the relaxation of the membrane, this is especially strongly pronounced (Figure 3.6). Three clear distinguishable areas can be identified. When scanning from $V_{mems} = 0 \rightarrow 13\,\text{V}$ it can be seen how there is an initial increasing quadratic relationship between V_{mems} and F_{res}. This is followed by a strongly linear increasing region which is then suddenly turned into a quadratically decreasing region. This is shown by overlaying the data with respective linear and quadratic polynomial fits.

The initial quadratic increasing behaviour is one that was to be expected and can be expected due to the relation between the straining force of the membrane and V_{mems} ($F_{\text{strain}} \propto k_{\text{eff}} \propto V_{\text{mems}}^2$). The effective stiffness is governed by the pretension of the membrane which should increase linearly with strain. Strain idealy scales linearly with the applied force which in turn scales quadratically with voltage (for small displacements). Now, this knowledge allows us to extract useful parameters from the hardening that is observed. Parameters such as the effective mass (m_{eff}) and the pretension (T_0). Let be given the dataset as presented in Figure 3.6 (b) with the voltage range such that

only the quadratically increasing domain is regarded ($|V_{mems}| \leq 5\,\mathrm{V}$). It is found that the effective mass is a factor of roughly 80-150 times (depending on the measurement set) the theoretical mass of the membrane. The pretension was found to range from 4.5e−5 N to 8.0e−5 N. The analysis had to make the assumption that the membrane was 20 layers of thickness ($\approx 7\,\mathrm{nm}$), which remains to be confirmed through an AFM measurement. The method that is used to obtain these two parameters is described in Appendix H. The value for the pretension seems at first sight a bit high compared to those reported in the literature [15]. More discussion w.r.t. the topic of effective mass and pretension can be found in Section 4.4.2 and Appendix H.

3.3.3. Modeshapes

The setup as described in Section 2.3 contains a vacuum chamber (Attocube) which has an internal 3-DoF (x-y-z) stick-slip piezo positioning system. This allows the sample to be conveniently aligned to the laser spot in these DoFs. What this furthermore allows is for measurement of the modeshapes. By obtaining an FRF for each point on the membrane, a modeshape image can be reconstructed. The modeshapes for the graphene sample are depicted in Figure 3.7.

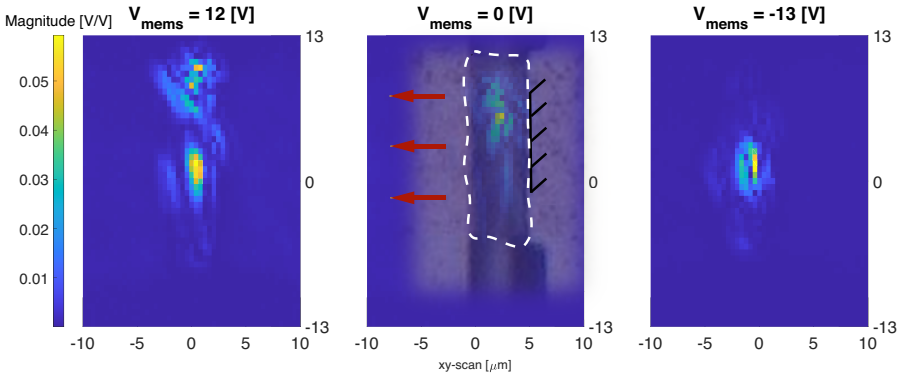

Figure 3.7: Modeshapes measured for three different values of V_{mems} with an indication of the flake orientation and straining direction.

Quantitatively there is nothing to take away from this experiment because the amplitude of vibration is not calibrated. Qualitatively one can observe how higher values of strain tend to converge the fundamental modeshape towards something that looks more like an expected symmetrical fundamental modeshape. Furthermore, the image seems to be distorted by interference lines which can be attributed to Fresnel diffraction. This effect is discussed in Section 4.4.4. Furthermore, it should be noted that the tilt of the sample w.r.t. to the (ideally) perpendicular optical path is important since tilts of only $\frac{1}{4}\lambda = 158.2\,\mathrm{nm}$ can have a tremendous effect on the magnitude of the measured interference signal.

3.4. Nonlinear dynamics experiments

Owing to the excellent mechanical properties of graphene and its (typically) miniature dimensions, it can easily be driven into the nonlinear regime using opto-thermal (parametric) actuation [84, 21]. In this work, it is shown how the nonlinear dynamics are tuned using opto-thermal, electrostatic and geometrical effects. The following Section will present the findings of a graphene membrane that is subjected to a moving suspension (CD shuttle) driven slightly and strongly in the nonlinear regime.

The original plan of this thesis was to obtain the Young's modulus from the nonlinear duffing-type response similar as described by Davidovikj et al. [24] and see how/if the mechanically applied force change would influence this.

3.4.1. Nonlinear stiffness tuning

Interesting behaviour is observed when probing the graphene membrane in the nonlinear regime. Figure 3.8 shows how the nonlinear response of the fundamental mode is affected by strain.

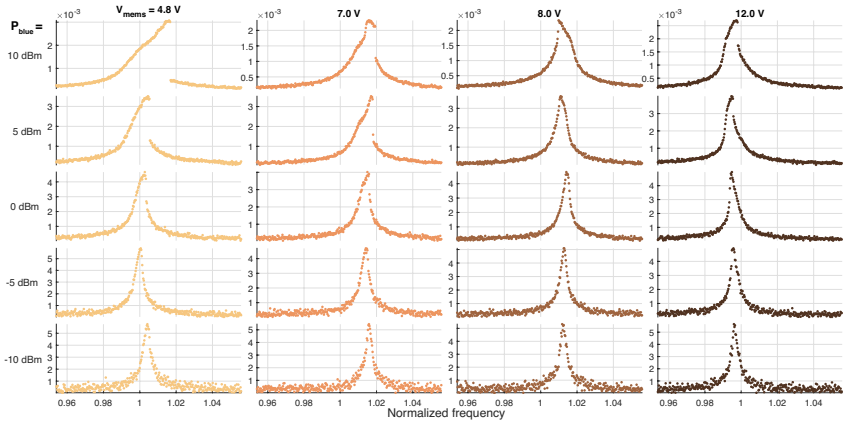

Figure 3.8: Plot array illustrating how the nonlinear frequency response shows initial spring hardening which then is dominated by a softening effect and again turns into a net hardening for larger strain values.

First, the onset of nonlinearity can be investigated, which corresponds to a driving power of $P_{blue} = 0$ dBm in Figure 3.8. It can here be observed how an initial nonlinear spring hardening (Figure 3.8 4.8V), which is gradually taken over by a softening type response (Figure 3.8 12V). In the preceding region, the competition between these hardening and softening can be observed and they cancel each other at this driving power for a straining voltage of 8V.

Next, the nonlinearity at large driving amplitudes can be investigated, which corresponds to a driving power of $P_{blue} = 10$ dBm in Figure 3.8. It can be observed how the composition of different stacked nonlinear effects changes as the membrane is strained. An initial spring hardening can be observed (Figure 3.8 4.8V) which is gradually taken over by a softening type response such that the combined hardening and softening response can be observed simultaneously (Figure 3.8 7V). This is referred to in other works as a partial cancellation of the duffing response [68]. Increasing the strain further allows the softening behaviour to dominate (Figure 3.8 8V). Finally at the largest strain values (Figure 3.8 12V), it can be observed that as the response starts to behave nonlinearly, the softening effect dominates but is dominated by hardening for higher driving forces. To summarise this, the high drive power behaviour comes down to a similar response as described for $P_{blue} = 0$ dBm but on top of that, a higher order nonlinear effect is visible which turns from hardening to softening to hardening.

Whether the total response is of a hardening or softening nature can be determined by estimating the sign of the (Duffing) nonlinearity constant k_3 [94]. That is assuming no higher-order nonlinearities are present. A general expression to find this Duffing constant is given here as such.

$$\omega_{nl} = \omega_{lin} + \frac{3}{8}\frac{k_{3,eff}}{m_{eff}\omega_{lin}}a_0^2 \tag{3.1}$$

Where ω_{nl} is the frequency at peak of the nonlinear response (Figure 3.8, $P_{blue} = 10$ dBm). Then ω_{lin} is the frequency at peak of the linear response (Figure 3.8, $P_{blue} = -10$ dBm). Then a_0 is the vibrational amplitude of the membrane. The measurement setup is not able to probe this value directly. In literature however it has been shown there is a way to calibrate the amplitude of vibration for a similar interferometric setup [34]. For determining whether the response is either hardening or softening, this is not required.

Here $k_{3,eff}$ is a cubic stiffness term that is corrected for the contribution of quadratic stiffness as such.

$$k_{3,eff} = k_3 - \frac{10}{9}\left(\frac{k_2}{\omega_{lin}}\right)^2 \tag{3.2}$$

Combining quadratic and cubic nonlinearities to effectively cancel one another has been shown in literature before [68, 84, 94, 48]. By comparing the peak locations from the linear and nonlinear response for all V_{mems}, allows the estimation of the term $\frac{k_{3,eff}}{m_{eff}}$ as such.

$$\frac{k_{3,eff}}{m_{eff}} = -\frac{8\omega_{lin}(\omega_{lin} - \omega_{nl})}{3a_0^2} \tag{3.3}$$

This value is now plotted for all voltages in Figure 3.9 and indeed it becomes apparent that a net hardening is partially cancelled by the softening to a net softening and back to a net hardening again. Note that this value thus represents the net tilt of the backbone curve that is influenced by geometric, opto-thermal and electrostatic nonlinear effects. The tuning of the resonance frequency up and down from the starting point is presented in Figure 3.6.

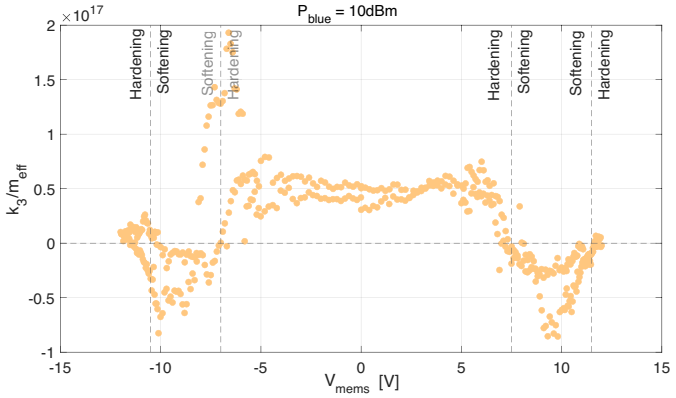

Figure 3.9: Scatter plot showing an indicative value k_3/m_{eff} whose sign determines if spring hardening (positive) or softening (negative) at the respective MEMS voltage. A full $V_{mems} = 0 \longrightarrow V_{max} \longrightarrow 0\,\text{V} \longrightarrow -V_{max} \longrightarrow 0\,\text{V}$ sweep is plotted.

4

Discussion

The results that were presented in Section 3 show that mechanical strain strongly alters dynamical response in both linear and nonlinear regimes. It is apparent that there is a tunability in both regimes which could be used to better understand the physical phenomena that are present in graphene but also other 2D materials. The initial thesis' goal was to obtain the Young's modulus from the nonlinear dynamical response, the data is theoretically there but the model that would isolate the Young's modulus as a fitting parameter remains to be finished.

4.1. Sample preparation

The method that was established to transfer graphene borrows ideas from the literature but is innovative nonetheless. It can transfer visually transparent graphene on a very fragile structure that is incompatible with fluids and has an extremely rough surface. It is hypothesised that the device layer of the MEMS device is covered with an anti-sticktion coating or surface treatment, although this statement remains unconfirmed. Despite that, this PPC-dome method has been shown to consistently overcome these problems. The use of PPC is not new, it has been used for the transfer of many 2D materials already [23, 39, 55, 64, 87, 102]. What is innovative are two factors.

1. A dome-shaped PDMS skeleton is used which allows for a very small contact area with the device, rather than a contact front. This is beneficial because of the fragile suspended structures on the device as shown in Section 2.1.1.

2. The PPC film is melted locally around the tiny contact area and is transferred along with the 2D material. This requires an extra post-processing step which is annealing. Due to the surface roughness, the 2D material is unable to find sufficient sticktion to the device and therefore always adheres to the PPC. This problem becomes irrelevant thanks to this technique.

The bottlenecks in the process of transferring are identified as well, and as such, are to be addressed in a future work.

1. The ability to find good flakes (thin and large enough). Especially if single-layer material is desired. Since the contrast of single-layer materials (especially for graphene) is generally very weak, i.e. it is almost transparent. There are however methods available to increase this contrast by tuning the thickness of the SiO_2 layer [7, 64].

2. The total time of device fabrication is dominated by the annealing step which requires the machine to gradually cool down over the time of 5 hours.

3. From the observed hysteresis (ω_n after measurement consistently drops) it can

be concluded that there is some slippage of the membrane. This deteriorates the maximum achievable strain values causing the device to become useless.

4. The wire-bonding process step seems to cause movement of the MEMS which makes the membrane slip (see differences in Figures 3.2&3.3 or Figure B.4). This alters the membrane's pretension (by a change in morphology) and can in some cases even lead to fracture.

Especially the clamping part poses a major limitation to this project. Since the membrane is free to slip (resisted by only small van der Waals forces), it is likely that the values of strain that are exerted in this project, are well below those that are actually achievable. The highest reported value of experimentally strained graphene is 14% [86]. The high surface roughness of the MEMS device is hypothesised to decrease the adhesion force of the membrane to the MEMS. This is counterintuitive since more roughness ideally results in a larger total adhesion area and friction coefficient due to morphological irregularities. Analogous to how a piece of wood slips easier along a fine-grid sandpaper w.r.t. coarse-grid sandpaper. However, during the stamping of the membrane, it is observed that the membrane conforms poorly to the roughness of the MEMS. This is observable with an optical microscope since the contrast of the membrane w.r.t. the surface is greatly reduced at the moment they make contact. Along the membrane's surface, it can however be observed that there are dark spots and areas where the contrast is larger than neighbouring areas. This most certainly shows that the membrane's surface poorly conforms to the rough surface. Such a schematic scenario is schematically portrayed in Figure 2.14 and can also be seen in Figure 3.2. The total effective contacting surface area is hence estimated to be smaller for the rough scenario compared to that of a lesser-rough surface and hence the hypothesis. Regardless of the validity of this hypothesis, slippage is observed (and is elaborated on in Section 4.4.1), which is the main problem that should be addressed.

In order to prevent the slippage of the membrane, an attempt was made to clamp the graphene. Unfortunately, this attempt was unsuccessful and is elaborated on in Appendix F along with ideas on how to overcome these issues. The continuation of this project shall therefore focus on clamping the membrane. Although this challenge is expectedly not too troublesome as it has been performed in literature plentiful [85, 86, 20, 21, 44, 122, 71]. Unfortunately, this has not been able to be investigated within the scope of this project but the predictions are positive that this can be achieved in a future project.

The next bottleneck, the wire-bonding process should also be improved upon. Unfortunately, this was not possible with the available means at the time of this project. From Figures 3.2 and 3.3 it becomes apparent that the comb drive has moved during the bonding process. In all cases, this resulted in a change of the surface profile of the membrane or even fracture. The explanation for this is that the wire bonder that was used is a ball-bonder (TPT HB05). In order to make the first bond (on the MEMS device), a spark is used to melt the wire which forms a ball on the wire before this is bonded. This high-voltage spark is provided by a ball-forming tool. In typical ball bonding, this ball can also be formed by electrical discharge such that the wire melts due to currents that flow. This ball is then pushed onto the bond pad with adjustable pressure and a small current in combination with ultrasonic vibrations and a heated bed cause the ball to fuse with the bond pad making a good electrical connection. The second bond is formed with ultrasonic vibrations, heat and pressure at the chip-carrier side, forming what is known as a wedge bond. Whether or not this machine is capable of forming ball-ball bonds rather than ball-wedge bonds remains to be investigated.

It is held possible that this spark could have caused the comb-drive shuttle to move significantly for a short moment. In theory, however, this spark should not affect the MEMS device. Another possibility is that the ultrasonic vibrations in combination with contact pressure on the device are too large. In one case, it was observed that the silicon beneath the bond pad had cracked, this is illustrated in Figure E.3 in Appendix E.

Another possible cause could be that there is a difference in electrostatic potential between the (isolated) comb-drive shuttle/static comb-fingers and the other side (chip-carrier). Which become connected when the second bond is formed. The solution to this issue should however not be too complicated. Wedge bonding for example does not use a spark and maintaining a proper ground connection at all times should solve the problem. Connecting the ground side (non-MEMS side) first, should allow for proper grounding at all times. The disadvantage is that the wedge bond has a larger footprint, which could cause an issue if the bond is not aligned properly. Reducing contact pressure and ultrasonic intensity are other parameters that should be optimized in the continuation of this project.

4.2. Derivation of EoM

In order to understand the observed dynamical behaviour of the graphene membrane, an effort was made to compare the results to an analytical model which gives the equations of motion (EoM). How they were obtained can be found in Appendix C.

4.2.1. Assumptions

In order to obtain the EoM, some assumptions and simplifications have to be made to keep the model analytically solvable. Some of which can have a large impact on the simulated behaviour. The main simplifications that were made are summarised below.

1. The mass of the CD shuttle is much larger than that of the graphene membrane ($M \gg m$). This should decouple the eigenmodes from the MEMS device and the membrane.
2. The membrane is rectangular of shape which enters a dimension of symmetry such that the 3D system can be handled in 2D (Figure C.1 xyz⟶xz).
3. The initial state of the membrane is flat. Such that is level with its supporting edges. There are no wrinkles, ripples or sag.
4. The initial out-of-plane stiffness comes from the pretension in the membrane, which is present. Although not modelled as van der Waals interactions with the sidewalls.
5. Bending energy of the membrane is neglected.
6. To analytically investigate the EoM, a Taylor expansion in the electrostatic force is made. This expansion only takes the constant and linear terms w.r.t. to the CD displacement u_l. That allows finding a simple explicit solution for $u_l = f(V)$ which can be substituted in the other EoM (Equations I.2 & I.3).

As for the first point; the mass ratio of the graphene w.r.t. the CD actuator is $\frac{M}{m} \approx 5e5$. The frequency of the fundamental resonance frequencies are in fact also orders of magnitude apart. Despite this, the dynamics of the CD shuttle can be affected by the motion of the membrane. As such, an experiment was performed where the CD shuttle was driven into resonance by actuating the graphene membrane. This experiment is elaborated on in Appendix D.1. This shows that the dynamics are in fact coupled, which is also analytically confirmed in Appendix I. Here the CD is mechanically driven into resonance by opto-thermally actuating the membrane. The measurement and actuation frequencies are the same in this scenario. That does not yet confirm that the eigenmodes are strongly coupled. Hypothetically and ideally they are decoupled but both Appendices D.1 & I show that there is a mechanical coupling. To confirm if the eigenmodes are coupled, this experiment could be elaborated on by actuating the membrane at resonance and measuring the FRF spectrum of the CD shuttle.

As for the second point; the suspended part of the membrane in question (see Figure 3.3 b), is very much rectangular. But there is a crease line (fold line) visible that has also changed visually during experiments. This naturally impacts the observed linear

and nonlinear behaviour. Thus the experimental geometry is non-flat, but geometry in the equations is assumed to be flat. A sold as such should have a large impact on the strain term of the membrane and also introduces a pre-deformation. But this crease line, as well as a pre-deformation are unaccounted for in the theoretical formulation of the membrane's EoM. It is later elaborated on how especially this pre-deformation might alter the dynamical behaviour which is discussed under the next point. The main effect of eliminating a DoF, is that the system is modelled as a string/beam, rather than a membrane. As such, one in-plane DoF (of the membrane in the direction of the trench, Figure C.1 y-direction) is neglected. This thus neglects the Poisson relationship between the two in-plane DoFs. This is not expected to have any significant impact on the EoM since pre-tension determines stiffness in the membranes [15, 105].

As for the third point; there is visually some oop deformation in unstrained configuration. The exact pre-deformation shape of the membrane is unknown but could be modelled as w_0. In the oop EoM and the strain formulation, there should be an extra term accounting for this deformation which thus respectively become the following [80]. The effect of this is discussed in more detail in Section 4.5.1.

$$m\ddot{w} - EA\left(\varepsilon_s\left(w' + w_0'\right)\right)' = 0 \tag{4.1}$$

$$\varepsilon_s = u' + \frac{1}{2}w'^2 + w'w_0' + \frac{1}{2}w_0'^2 + \varepsilon_0 \longrightarrow \frac{u_l}{l} + \frac{1}{l}\int_0^l \left(\frac{w'^2}{2} + w'w_0' + \frac{w_0'^2}{2}\right)\mathrm{d}x + \varepsilon_0 \tag{4.2}$$

As for the fourth point; the pretension ($l\varepsilon_0 = T_0$ [N]) is a parameter that is obtained by performing the fitting procedure as described in Appendix H. The values obtained in the low Young's modulus scenario ($T_0 \approx 6\mathrm{e}{-7}\,\mathrm{N} \longrightarrow 0.03\,\mathrm{N/m}$) are low but comparable to other values found in literature ranging from $0.015\,\mathrm{N/m}$ to $1\,\mathrm{N/m}$ [9, 38, 16, 15]. And as such is assumed to be a plausible result. By inserting the pre-strain as demonstrated, the assumption of a flat-level membrane (i.e. no pre-deformation) holds. So the effects of pre-deformation (wrinkles and sag) on the dynamics are not covered by the pretension term.

As for the fifth point; the bending energy is indeed neglected because this is a standard assumption in membrane theory [24, 27, 93, 94]. Although there is a limit to the thickness of a membrane where it is still considered a membrane. Castellanos-Gomez [15] states that for graphene membranes, their mechanics start displaying plate-like behaviour (bending rigidity) that should not be neglected when the thickness exceeds 15 layers. From the optical contrast, the sample in this work shows (see Figure 3.3 b), that the sample is most certainly not single- or double-layer. How thick it exactly is, remains to be confirmed with for example an AFM measurement. If the outcome is that it is of adequate thickness the bending energy shall be taken into account. Layer thickness is not the only factor that can contribute to bending rigidity, even single-layer graphene can have bending rigidity due to wrinkles, ripples and crumples [30]. To take into account the bending rigidity, there is again an alteration in the oop EoM and the strain formulation. Note that in the following equations, pre-deformation w_0 is neglected for clarity [80].

$$m\ddot{w} - EA(\varepsilon_s w')' + EIw'''' = 0 \tag{4.3}$$

$$\varepsilon_s = \varepsilon_m + z\varepsilon_b + \varepsilon_0 = u' + \frac{1}{2}w'^2 + z\left(w''\right) + \varepsilon_0 \tag{4.4}$$

Here, the newly introduced variable z describes the distance away from the midplane. In a deformed configuration ($w''(x) \neq 0$), there shall thus be a positive and negative contribution to the total strain energy coming from tensile and compressive strain respectively. The term EIw'''' describes the Young's modulus, the mass moment of inertia

($\frac{bh^3}{12}$) and the $w'''' = \frac{\partial^4 w}{\partial x^4}$ which combined gives the restoring force originating from the bending moment.

As for the sixth point; the Taylor expansion has only regarded constant and linear terms for simplicity's sake. Since the CD appears to deflect largely, the higher order should probably be accounted for. Otherwise, a similar problem might occur as described in Figure 3.4, especially for larger displacements ($u_l \geq 0.2\,\mu$m).

4.2.2. Static- dynamic analysis

Ideally, the MEMS device exerts mechanical force (resulting in strain) on the 2D membrane and nothing else. In this case, the dynamics and mechanics that are probed are fully originating from the membrane that is researched and isolated from the MEMS device (i.e. no mechanical/electrical coupling). To achieve this, there are a couple of main design features were implemented. The first one being that the relative sizes and masses of the CD shuttle and the membrane. For a large and thick graphene membrane, the mass ratio would be $\frac{M}{m} \approx$ 5e5. Secondly, the CD shuttle was designed to have a high oop stiffness compared to the ip stiffness. The area moment of inertia comes from the height and width of the suspended beam flexures, such that $I_{oop} \approx 56 I_{ip}$, more info on the device geometry is given in Section 2.1. The effect is that there should be little oop deflection of the CD shuttle and that the eigenfrequencies of oop membrane modes and oop CD shuttle modes are far apart such that the energy exchange between them should be negligible. Thirdly the device is designed to be able to exert great forces on the membrane due to the large electrostatic capacitive surfaces. In the ideal case where there is no initial sagging of the membrane and it being firmly clamped (i.e. no slip), the maximal achievable strain value is $\varepsilon_{\max} \approx 10\%$. This value is obtained using the rule-of-thumb for electrostatic MEMS devices stating that the "pull-in" occurs at $\approx \frac{1}{3}$ of the gap length which is $d_1 =$ 2e−6 m. For a MEMS device without graphene incorporated this rule-of-thumb can be confirmed by looking at Figure 3.4. This value of $\varepsilon_{\max} \approx 10\%$ is higher than some works have illustrated to obtain [44]. But also lower than others [86]. Given these three arguments (in particular the first two), the dynamics of the membrane should be isolated from that of the CD actuator.

In practice, this is however not the case. There is an observed electrostatic coupling in the nonlinear dynamics experiments. This should logically originate from the fact that there is a coupling between the ip displacement EoM (u_l) and the oop displacement EoM of the membrane (w). This is experimentally observed in multiple ways. Firstly from the electrostatic softening that arises in the nonlinear dynamics 3.8. Secondly, an interesting experiment that directly demonstrates this coupling is presented in Appendix D.1. Not only experimentally, but also analytically, this coupling arises the EoM. As is presented in Appendices I & K. This coupling is not necessarily a bad thing, with a proper and complete theoretical model of the system, this coupling could be utilized. Effectively, this system now thus forms a coupled resonator. Coupled resonators can be used in particularly sensitive resonant sensing applications. For example in radio communications they can be used as filters with extra sharp frequency response [60]. Also for theoretical research, they can for example be used to manipulate phonon populations and create intrinsically localized modes [114]. These are just some of the potential applications where (tunable) coupled resonators might appear. The coupled resonator created in this work is particularly interesting because the CD shuttle is controllable which should allow for tuning of the coupling strength.

4.3. stiffness simulation

For the analysis of the obtained frequency response data as tension to the membrane is applied, a good analysis of the voltage-displacement ($u_l(V)$) is required. When for example trying to obtain the effective mass and stiffness, this $u_l(V)$ data is required to estimate the tension exerted onto the membrane. This knowledge is furthermore important to protect the device and make sure no pull-in occurs. Recall the formula

describing the force that deflects the CD actuator in the in-plane (IP) direction.

$$F_e(V,u_l) = \left(\frac{nA\epsilon_0}{2(d_1-u_l)^2} - \frac{nA\epsilon_0}{2(d_2+u_l)^2}\right)V^2 = \frac{nA\epsilon_0(d_2^2+2u_l(d_1+d_2)-d_1^2)}{2(d1-u_l)^2(d_2+u_l)^2}V^2 \tag{4.5}$$

$$F_e(V,u_l) = k_{mems,ip}u_l \tag{4.6}$$

The corresponding parameters are described in Section 2.1.1. From this equation, it becomes apparent that the total force depends not only on the applied voltage but also on the displacement of the shuttle. It is this displacement which is responsible for the softening effect ($F_e(V,u_l)$). By equating this to the force in the flexures, the static equilibrium is obtained ($F_e(V,u_l) = k_{mems,ip}u_l$). This equation can unfortunately only be solved for V directly. Such that it is rewritten in the form $V(u_l)$. This can then be numerically inverted to obtain the relation that describes $u_l(V)$. Both analytical numerical (COMSOL) simulations are then plotted in Figure 3.4.

Here it can be observed how the numerical model has failed to simulate the expected electrostatic softening which results in pull-in. This effect is strongly nonlinear and the simulation software seems to have circumvented this. The hypothesis is that the reason for the numerical simulation to behave like this is because it progresses linearly through the stages of its physics. Firstly, the geometry is created and relevant physics are applied. In this case, solid mechanics and electrostatics, which combined result in electromechanical forces. A mesh is created after which the forces are calculated based on the physics and that mesh, then the deformation can be determined. The problem that arises here is that the force is dependent on its solution (those deformations).

In order to circumvent this issue, a moving mesh was implemented to model the geometry as continuously deforming with the arbitrary Lagrangian-Eularian (ALE) technique. The effect hereof is that a new mesh is computed whilst the component is in its deformed state after which the same conditions are applied. In theory, if this is allowed enough iterations, which are computationally much more expensive, the result should converge to that of the analytical solution. This is illustrated in Figure 4.1.

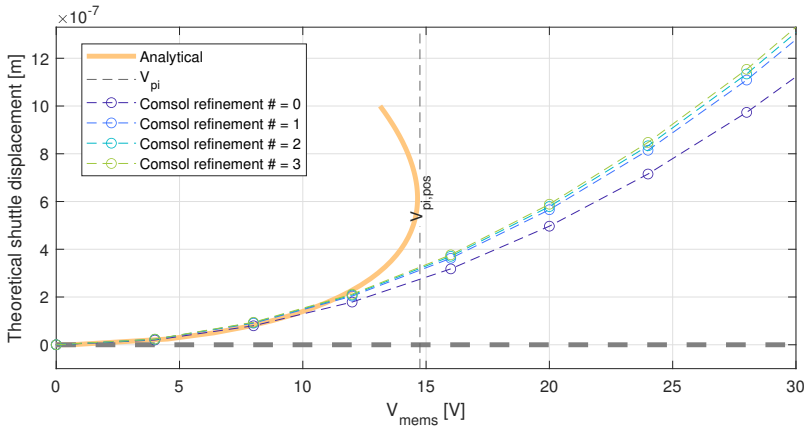

Figure 4.1: Comparison of analytical solution of the voltage-displacement curve to a COMSOL model with moving mesh refinement according to the arbitrary Lagrangian-Eularian (ALE) technique.

As can be seen in Figure 4.1, the numerical solution does start to bend towards the analytical solution but seems to do so not completely and quickly converge to an in-between solution still unable to capture the pull-in behaviour. Therefore, the analytical solution shall be used in order to describe the behaviour of the MEMS device in further analyses. It could be that for many extra computations, the numerical solution does converge, however, this is deemed unnecessary. For the simple reasons that this

is computationally to expensive and the theoretical model seems to provide a solution that corresponds better to the experimentally observed behaviour [52].

Now to further investigate the device, a graphene membrane's stiffness is introduced. If it was a perfectly flat membrane, firmly connected to the anchors (no slip), with 20 layers thickness and $E = 750\,\text{GPa}$, the pull-in voltage would be $V_{pi} \approx 296\,\text{V}$. Whereas for the same assumptions, but instead $E = 15\,\text{MPa}$, the pull-in voltage remains as raised in Figure 4.1. This shows the system is definitely not ideal (due to sag and wrinkles) and the actual effective Young's modulus is probably much closer to $E = 15\,\text{MPa}$. In the experiments, this pull-in was observed whilst straining on $V_{\text{mems}} = 13\,\text{V}$. This pull-in occurred multiple times on different devices during the modeshape measurements, as elaborated on in Section 4.4.4.

4.4. Linear dynamics experiments

When the driving power of the interferometric setup is not too large, the membrane oscillates in the linear regime. Applying mechanical strain already has a great influence in this region. In the initial measurements, before much slip occurred, a tunability of $5 \sim 8\%$ was identified. From the symmetry in positive and negative straining voltages (V_{mems}), it can be concluded that the MEMS device functions properly and there are no trapped charges that would give rise to an asymmetric bias.

4.4.1. Hysteresis and slipping

From the results of straining the membranes whilst linearly resonating, as presented in Figures 3.5 and 3.6. It becomes apparent that there are two effects causing issues in interpreting the data. These are hysteresis (from sliding, which is repeatable) and slipping (which is not repeatable).

Hysteresis is observed between sweeping up and down the straining voltage of the MEMS device (V_{mems}). As such, there is a slight difference observed in the resonance frequency at a certain voltage depending on whether the V_{mems} is being swept up or down. This cannot be contributed to trapped charges in the device since the resonance frequencies are not different at $V_{mems} = 0\,\text{V}$ (after doing a number of repetitions such that the response has settled). As can be observed, in one sweep of voltage ($V_{mems} = 0 \longrightarrow 13 \longrightarrow 0\,\text{V}$), two loops are drawn by the resonant frequencies (A sort-of figure eight). Split by the region of increasing to decreasing resonant frequency, which is attributed to the "electrostatic spring softening" effect. A (very) recently published work by Ying et al. [124] had found similar behaviour and attributed this hysteresis loop(s) to the sliding of the membrane from its clamped edges. The fact that the resonant frequency remains indifferent in the unstrained configuration, shows that this sliding is reversible, in such a scenario, there is thus no slip. This sliding is something that can best be understood as an effect of the Coulomb friction that causes a certain "virtual play". It would be interesting for future work to see if this effect still prevails when the membrane is firmly clamped at the boundaries. It hypothesised that in this firmly clamped scenario, there will be ideally no more hysteresis if it indeed arises from sliding. Furthermore, the fact that the hysteresis loop is repeatable, insinuates a certain IP compressive stiffness. Which can be explained by wrinkles and some finite bending stiffness in the membrane. These effects contribute to the hysteresis loop observed but are repeatable.

Slipping is a related effect but has a much more drastic outcome. Once slippage occurs, the effective length of the membrane increases. Due to the extremely low bending rigidity and thus compressive stiffness, this slippage is irreversible. It is clearly observed by how the unstrained resonance frequency consistently drops after straining and eventually settles ($f\text{res,start} \approx 8\,\text{MHz} \longrightarrow f\text{res,end} \approx 4\,\text{MHz}$). Assuming the effective mass has remained constant throughout measurements, tells us the pretension in the membrane has decreased by a factor of 4 through these occurrences. This slippage

could result in either a sag, wrinkles or sidewall adhesion of the membrane. It remains troublesome to isolate exactly what occurs. An analysis was performed on this in Appendix J. The first scenario is believed to be the most likely scenario. In a test sample of MoS_2 (not discussed in this thesis), it could be seen how the sample had adhered to the sidewall between experiments, but as soon as it was strained and relaxed, this sidewall adhesion had been converted into a sag. This sag seemed to be the more stable solution of the elongation in the suspended length of the membrane. These events were captured and are presented in Figure E.2 in Appendix E. Yet another possibility which is not analysed quantitatively is buckling. This can best be understood by imaging the membrane elongating due to slipping in tensioned configuration, and then ever-so-slightly buckling as tension is released. Naturally, it is also possible that a superposition of these phenomena occurs [10], making it difficult to establish what exactly happens. Although with great certainty it can be said the membrane slips when being tensioned.

4.4.2. Obtaining system parameters from hardening response

The initial increase in resonance frequency as mechanical force (inducing strain) is exerted on the membrane is a somewhat intuitive result. By straining the effective tension in the membrane would increase and thus the effective stiffness and thus the resonance frequency. This effective stiffness can be modelled such that it can be used to fit the data. How this has been done is described in Appendix H. The model that describes the effective stiffness was obtained from literature [15, 38]. This model however assumes an ideal membrane, with finite bending rigidity. This bending rigidity can be neglected as it contributes to $\approx 2\%$ of the effective stiffness (assuming large Young's modulus and 15-layer thickness). What is problematic, however, is the representation of wrinkles and sag in the expression for effective stiffness. From the experiments and analyses such as shown in Appendices H,J,K,G it can be concluded that there are in fact wrinkles and sag present in the sample, especially after doing a couple of straining repetitions. Obtaining the Effective mass and pretension from this model requires however the flake geometry and Young's modulus to be assumed. Assuming high $E = 750\,\text{GPa}$, yields $m_{\text{eff}} \approx 100 m_{\text{theoretical}}$ which could possibly be explained by contaminations like polymer residue and other small particles. The obtained pretension yields values are relatively large as well ($T_0 \approx 10\,\text{N/m}$). This value is a lot higher than values reported in Literature. Some literary values are summarised in Table 4.1. As such, this high value gives rise to the suspicion that the assumption of a high Young's modulus might be incorrect. Although a possible explanation for this high pretension is that the membrane is contaminated with unannealed polymers or adhered hydrocarbon molecules [12, 34, 35, 105].

Pretension [N/m]	**Shape and size (width*length) [μm^2]**	**Source**
0.006	Recangular, 2 by 1.2	[110]
0.1-0.16	Circular, r=2	[53]
0.1-1	n.a.	[15]
0.1	Rectangular, 3 by 2	[38]
0.015	Circular, r=5 (MoS_2)	[16]

Table 4.1: Indications of values obtained describing the (intrinsic) pretension of graphene membranes and a single MoS_2 for comparative purposes.

On the other hand, if the membrane is assumed to be clean of contaminations, the effective mass, should logically be somewhat equal to the theoretical mass. For a fully clamped rectangular membrane, it is known that $m_{\text{eff}} \approx \frac{1}{4} m_{\text{theoretical}}$, so for the double clamped scenario at hand, resonating at the fundamental mode, it ought to be $\frac{1}{2} m_{\text{theoretical}} \leq m_{\text{eff}} \leq m_{\text{theoretical}}$. Using this, the Young's modulus can be used as a fit parameter instead of the effective mass. This gives the result that $E \approx 15\,\text{MPa}$, which is orders of magnitude smaller. Although not unreasonable. Due to the slipping, wrinkles and sag are deemed to occur. Which have a tremendous impact on the effective

Young's modulus [82, 95]. Consequently, the result for the pretension in this scenario gives $T_0 \approx 0.1\,\mathrm{N/m}$, which is a very reasonable value compared to literature [15, 16, 110].

From this analysis, the second scenario (low E, low T_0) is the most plausible. This indicates that despite the increase in resonance frequency, there is little actual strain being applied. TWhich can be fortified with the idea that slip is observed. After the slip, the membrane shall thus sag and the actual strain thus is limited. This in turn also raises the question about the correctness of the stiffness expression in Equation H.11. In reality, there should logically be a separation between the two regimes. A region where strain is only reducing the sag, and a region where actual strain is applied (which in turn assumes no slip). Such bi-regime behaviour is observed for suspended graphene membranes before [95]. In a continuation to this thesis, provided proper clamping constraints are achieved, could investigate the difference between these regions and should see a significant change in the obtained Young's modulus for both.

4.4.3. Shape of resonance response

Typically, this electrostatic frequency softening is observed in suspended graphene membranes that use an electrostatic back-gate for tensioning (and sometimes drive but not necessarily). In the scenario as described, what is observed as the gate voltage is increased, is that the resonance frequency decreases, and then switches into an increasing behaviour. As the phase of the resonating membrane is such that its deflection is towards to gate, the electrostatic tensioning force increases which effectively slows the resonance. As this gate voltage is increased further, the tension rise in the membrane increases which then effectively increases resonance frequency much like tensioning a guitar string. This latter effect (the increase of resonance frequency) tends to be initially (low gate voltage) weaker than the former effect but dominates as the gate voltage is increased. If then a 2D plot is made with the positive and negative gate voltages on the x-axis and the resonance frequency on the y-axis, a "w" shape is observed [24, 19, 74].

In this work, the opposite shape is observed and thus represents more of an "m" shape (Figure 3.6). To understand this, one needs to think about what causes the softening effect in this work. Which comes from the electrostatic fingers of the CD shuttle. The electrostatic force (and thus displacements) scales quadratically with the voltage scaling linearly. It thus becomes apparent that the electrostatic force for is tiny for initially small V_{mems} and gets larger quadratically (even higher orders for displacements approaching the "pull-in" voltage V_{pi}) as the voltage is increased. As such, the increase in resonance frequency due to tensioning dominates for small V_{mems} and succumbs to the electrostatic frequency softening effect for larger V_{mems}. This idea can be fortified by the observation that the membrane slips. As such, the provoked internal tension in the membrane is limited (as the membrane slips) which allows the softening effect to become even larger w.r.t. the natural (geometric) frequency hardening effect as V_{mems} is increased.

4.4.4. Modeshape measurements

Although the modeshape measurements (Figure 3.7) do not provide any quantitative information about the flake (i.e. the results are presented in non-physical units), they do show some interesting behaviours. It can be seen from the way the modeshapes change as the MEMS device pulls one side of the membrane. Figure 3.7 shows that the right edge of the membrane remains fixed, and the left side moves about half a micron.

There are some initially wrinkled regions at ($V_{\mathrm{mems}} = 0\,\mathrm{V}$) that have little to no vibrational amplitude. But as the CD shuttle pulls ($V_{\mathrm{mems}} = 12\,\mathrm{V}$), these regions become untangled and show greater vibrational amplitude. In this scenario, the effects of con- and destructive interference are best visible. In these experiments (Figure 3.7), this interference is visible from the diagonal lines where no amplitude is measured. A colleague who also studied the same MEMS devices analysed this interference, which is presented in Appendix L. As such, the presence of Fresnel diffraction due to cavity geometry can

be established [52]. Accidentally, the MEMS manufacturer delivered a couple of devices without the cavity layer. These devices indeed showed no diffraction patterns, and are unfortunately unusable as MEMS devices (also presented in Appendix L). Another possible cause for the visible diffraction lines could be a tilt in the sample w.r.the (ideally) perpendicular optical path. Tilts of only $\frac{1}{4}\lambda = 158.2\,\text{nm}$ (deflections along the direction of the optical path) can have a tremendous effect on the magnitude of the measured interference signal. The observed diffraction patterns are likely a superposition of both effects.

As the strain is increased to ($V_{\text{mems}} = 13\,\text{V}$) a clear change in modeshape is observed where the vibrational energy concentrates to the middle of the flake. The actual strain in this scenario is however still probably limited due to identified slippage of the membrane. Some slight strain is certainly present but is limited by the friction of the adhered sides of the membrane to the SiO_2.

During some measurements of the modeshape at these larger voltages, it occurred that the mems device got "pulled-in". This is unexpected to observe at these voltages. In the ideal scenario where there is no slip and no pre-deformations, the pull-in voltage is calculated to lie at $V_{\text{mems}} = 296\,\text{V}$ (assuming 20 layers thickness and high E). The fact that this pull-in is observed multiple times during measurements subjected to only 13 V teaches us a couple of things.

Firstly, the effective ip stiffness of the membranes is very low. This is strongly linked to the geometry/morphology (wrinkles and sag). This can have several causes, the most likely of which is slipping at the supporting edges but also imperfections and forces during fabrication could contribute to this. Due to this low effective ip stiffness, the actual pull-in voltage is probably close to the theoretical prediction of $V_{pi} = 14.7\,\text{V}$ (Figure 4.1).

Secondly, there could be problems with the electrical grounding of the measurement setup. During some experiments, electrical shocks were perceived as the setup was touched. Since a physical shock could be felt, the electrostatic potential build-up on the optical table must be in the order of hundreds of Volts. This phenomenon was later contributed to a faulty power supply of the red He-Ne laser. This grounding issue has been attributed to an unused power supply and had adequately been addressed. Whether or not the pull-in occurred from outside influences remains inconclusive, but the possibility that there are static charges that create a potential on the CD actuator is not excluded.

Thirdly, the time that these devices were exposed to $V_{\text{mems}} = 13\,\text{V}$ was rather long, about 8 hours. In the tension-frequency response measurements (Figure 3.5), the device is also subjected to $V_{\text{mems}} = 13\,\text{V}$ many times repeatedly, but no "pull-in" occurred here. An explanation of this easier-than-expected "pull-in" could be that whilst the system was subjected to $V_{\text{mems}} = 13\,\text{V}$, the vibrations of the connected vacuum pump caused the CD shuttle to be slightly nudged and as such become "pulled-in". These vibrations occurred every 15 minutes and last about 2-3 seconds. Other explanations exist and shall be investigated by the next person who studies mechanically strained graphene with these MEMS devices.

4.5. Nonlinear dynamics

The nonlinear dynamics of graphene resonators can be used advantageously in for example sensing applications. The ability to tune the effective nonlinearities has been shown to increase dynamic range and mass resolution [84].

An initial hardening behaviour was expected for larger drive amplitudes. This effect can be explained by the geometric nonlinearity that occurs when the membrane deflects. In the deflected configuration, the surface area is by definition enlarged and thus internal tension increases, which in turn is directly related to the effective stiffness which therefore also increases. As such, the frequency of resonance increases. The subse-

quent softening behaviour that arises as the strain is further increased is hypothesised to originate from the electrostatic comb fingers. This electrostatic softening effect is something that is well understood and described in literature [24, 19, 74].

In the high-deflection amplitude resonance (nonlinear response of Figure 3.8 at 0 dBm) of the membrane, a similar effect occurs as described in Section 4.4.3 (which was the electrostatic frequency softening mechanism). In this nonlinearly resonating scenario, there is an initial nonlinear Duffing-type hardening observed. Which, as the V_{mems} is increased, turns into a net softening. This is again due to the inversely squared relation in the force-distance curve in the electrostatic combs. There is a point where a small deviation in the oop deflection of the membrane, has a large impact on the induced force by the CD. Because the oop motion of the membrane is coupled to the ip motion of the CD. giving rise to electrostatic softening that originates from the CD actuator.

In the highest-deflection amplitude resonance (nonlinear response of Figure 3.8 at 10 dBm) the same is observed with new effect added onto the response. In this case, an additional stronger nonlinear effect dominates the softening as previously described for large V_{mems}. Since the deflection amplitudes are (relatively) large at this driving amplitude, this dominating hardening could be attributed to higher order (quintic and up) geometric nonlinearities [88].

By repetition of these strained responses, it was shown that these nonlinear responses can be repeatably tuned and controlled. Although they were obtained from a single device. Repeating these experiments on another similar membrane could confirm the validity of these observations. Nevertheless, the behaviours that are observed in the nonlinear (large deflection amplitudes) regime can be intuitively explained. There is a clear competition between electrostatic softening effects and geometric hardening effects. Since the geometric nonlinearities are governed by the geometry of the membrane, it is unlikely that a new graphene membrane will show the exact same behaviour, although competition between nonlinearities should be present. Further improving boundary conditions (clamping of the membrane) is expected to result in a particularly stronger tuning of the geometric hardening nonlinearities.

4.5.1. Simulating the nonlinear behaviour

In order to understand the nonlinear behaviour that was observed, the Equations of Motion (EoM) as derived in Appendix C are investigated. Recall that these equations assumed no initial sag and neglected the bending moment of the membrane. By performing a first-order Taylor expansion on the electrostatic force, assuming a mode-shape in that is commonly assumed for a doubly clamped plate [115] $\phi(x,t) = \sqrt{\frac{2}{3l}}(1 - cos\left(\frac{2\pi}{l}x\right))q(t)$ and utilizing the Galerkin approximation. It is possible to obtain an expression for the out-of-plane stiffness $k_1 q(t)$ & $k_3 q^3(t)$. The procedure and results of this analysis are elaborated on in Appendix K. This analysis has yielded two main results.

1. The hardening turning to softening as observed experimentally (Figure 3.8, P_{blue} = 0 dBm) is confirmed analytically. The experimental behaviour observed at higher amplitudes (Figure 3.8, P_{blue} = 10 dBm) is however not grasped by this model. This can be explained by the assumptions that were made in the derivations.

   The first, and perhaps the most important, is that the geometry of the membrane is assumed to be flat in the derivations. This has a large effect towards the derived EoM. Slippage of the membrane is however clearly observed, therefore it is highly likely that the membrane is not flat, but sagged instead. The OOP deflection is described by the EoM with $w(x,t)$ (for simplicity just w). Now if there is an initial sag, that means the total OOP deflection would be offset such that $w_{tot} = w + w_0$. Revisiting the EoM and the formulation of the strain would be

altered and yield.

$$m\ddot{u} - EA\varepsilon_s' = 0 \tag{4.7}$$

$$M\ddot{u}_l + ku_l + EA\varepsilon_s = F_{cd} \tag{4.8}$$

$$m\ddot{w} - EA\left(\varepsilon_s\left(w' + w_0'\right)\right)' = 0 \tag{4.9}$$

$$\varepsilon_s = u' + \frac{1}{2}w'^2 + w'w_0' + \frac{1}{2}w_0'^2 + \varepsilon_0 \longrightarrow \frac{u_l}{l} + \frac{1}{l}\int_0^l \left(\frac{w'^2}{2} + w'w_0' + \frac{w_0'^2}{2}\right)\mathrm{d}x + \varepsilon_0 \tag{4.10}$$

This would translate into more factors that contribute to the cubic nonlinear stiffness as well as the addition of quadratic nonlinearities which then possibly could confirm the experimentally observed nonlinear switching behaviour observed at high P_{blue}. This remains to be investigated by simulation of the equations. In normal high-deflection thin and long beam mechanics of a simple doubly clamped beam, the geometrical nonlinearity k_3q^3 is always a positive value when it originates from elongation which thus "hardens" the beam [18]. In the case of a predeformation, this elongation can just as well be a compression during the vibrational cycle of the membrane. This adds another reason to believe that an (unknown) pre-deformation ($w_0(x)$) is missing from the mathematical model. Additionally, the combination of positive and negative nonlinearities gives rise to buckling behaviour

The second would be neglecting bending energy. Despite being a common assumption for membrane mechanics, its contribution can cause nonlinearities, especially when the membrane is not atomically thin and undergoes large deformations. Including this energy in the OOP would result in an extra term contributing to this respective EoM 4.9, yielding.

$$m\ddot{w} - EA(\varepsilon_s(w' + w_0'))' + EI\left(w'''' + w_0''''\right) = 0 \tag{4.11}$$

The bending moment as is presented $EI\left(w'''' + w_0''''\right)$, should only contribute to the linear OOP stiffness. Because by performing the Galerkin approximation and using the modeshape which only linearly depends on the oop displacement variable $q(t)$, should thus only contribute to the linear stiffness analytically. Intuitively, the bending moment could add contribute to nonlinearities of the coupled EoM.

The third assumption affecting the behaviour is that there is no slippage occurring. After the first couple of measurements, a distinct drop in unstrained resonance frequency is observed. This has been investigated in further detail in Appendix J. This gives a well-supported belief that there is a sag in the membrane and that the applied strain is less than the EoM suggests.

2. From the transition point and the voltage where the device seems to "pull-in" in the nonlinear analysis, it can be concluded that the effective Young's modulus in the experimental sample is much lower than most intrinsic reported values in literature. The value obtained from the adjusted linear fit (Appendix H, $E \approx 15\,\mathrm{MPa}$) seems to describe observed behaviour much better compared to a more accepted intrinsic value of $E \approx 750\,\mathrm{GPa}$. This also strongly points to there being wrinkles and sag in the experimental sample [82]. That being said, the nonlinear model used here is still to be expanded such that pre-deformations and perhaps the effect of sidewall adhesion are included.

This analysis has not investigated the presence of damping mechanisms. Linear viscous damping ($F_{\mathrm{d,lin}} = -\tau_{\mathrm{lin}}\dot{w}$) usually dominates the effective damping. Although recent works have shown that the effects of nonlinear damping of for example van-der-Pol type ($F_{\mathrm{d,nl}} = -\tau_{\mathrm{nl}}w^2\dot{w}$) can have considerable effects, particularly when there is an internal resonance between modes [62].

To summarise the simulation of the nonlinear behaviour, the cancellation of geometrical nonlinearities with electrostatic nonlinearities for a flat membrane is presented. This partially explains the observed experimental behaviour. There are however in the experimental system, more sources of nonlinearities present that remain unmodelled. These can arise from pre-deformation, slippage, bending energy, damping mechanisms and possibly more. Having a complete analytical description of the nonlinear effects is crucial when it is for example desired to obtain material parameters such as the Young's modulus.

5

Conclusions and recommendations

5.1. Conclusions

Reflecting on the purpose of this thesis, many lessons were learned. Recall the goal of this research as presented in Section 1.2. As such, the research question was proposed to be "Does mechanical tensile strain affect the nonlinear dynamic characterization of graphene's Young's modulus". This research question has quite a definite yes-or-no answer, but to obtain this, an extensive process precedes from which many other lessons can be learned regarding the behaviour of suspended graphene subjected to a mechanical straining force. The main motivation to investigate mechanical strain is that it is the best manner to probe purely the intrinsic mechanical properties of graphene. Despite this, there is little research performed in this manner. This can logically be explained by the challenging manufacturing process. Contrary to electrostatic tensioning, which is therefore the most commonly described. Section 1.2 also presents the main drawback(s) to this method which urges to go the route of mechanical straining.

To perform the planned experiments to obtain a nonlinear dynamical response of a resonating graphene sheet, the device that had been pre-fabricated needs to be incorporated with graphene. This turned out to be a particularly challenging process due to two main problems described in Section 2.2. The persistency to overcome these issues has yielded a new transfer technique that has not been described in the literature before and allows the placement of multiple flakes of exfoliated 2D materials in close vicinity to one another ($\approx 250\,\mu$m apart) each in a desired orientation. This in itself is a success and opens up the path to explore the possibilities of other devices that are present on the same MEMS die.

With samples fabricated, wire-bonded and connected to a programmable power supply, the dynamics as a function of mechanically applied force was investigated. This should in theory deliver the data required to answer the research question. The dynamics can be split into two regions, linear and nonlinear. The understanding of the lower amplitude linear vibrations gives a good foundation to explain behaviours observed at higher amplitude nonlinear vibrations. These experiments were performed on two devices, incorporated with graphene MoS_2 (both thicknesses unconfirmed). The results of the latter are not presented in this thesis as there were many "pull-in" events of the CD that make the results questionable.

From the first set of linear dynamics experiments on graphene, a couple of main conclusions were drawn. Firstly, there was an observed repeatable hysteresis loop when sweeping V_{mems} up and down (Figure 3.6). This effect has recently been analysed in literature [124] and can be attributed to for example Coulomb friction. The second

observations was a hysteresis that was not repeatable (Figure 3.5). After each sweep of V_{mems}, the resonance frequency kept steadily dropping (8 MHz $\longrightarrow$ 3.5 MHz) until it eventually settled. This observation is attributed to slip and is what made interpreting and mathematical modelling of the data a lot more difficult. The Third observation was made in the high V_{mems} region. An unexpected drop in resonance frequency was consistently observed which indicates that the dynamics of the membrane are coupled to that of the CD. This was later confirmed experimentally and mathematically.

From this data (Figure 3.5) it was possible to obtain the effective mass (M_{eff}) and pretension (ε_0) if the Young's modulus is assumed. Assuming a high Young's modulus yielded surprisingly large values for M_{eff} & ε_0. This can be substantiated by polymer residues but is deemed unlikely. If instead a reasonable M_{eff} is assumed, then a reasonable ε_0 follows and a very tiny Young's modulus ($\approx$ 15 MPa). This second scenario can be substantiated by the slipping that is observed. The extremely low bending rigidity of (near) 2D materials then logically explains the low values for the obtained Young's modulus. Hence, this scenario is deemed the most likely.

Next, there were experiments in the high-deflection nonlinearly behaving regime. Depending on the driving strength, different nonlinear effects were observed of hardening, softening and combined behaviour. Plausible physical explanations for these are given in Section 4.5. A mathematical model was proposed to possibly obtain system parameters (Appendix K). It was however found that this model was only valid for understanding the low Young's modulus and the coupling of the membrane and CD actuator dynamics. To obtain more nonlinearities in the model, the initial sag of the membrane should be incorporated.

Furthermore, an experiment was performed to analyse the modeshape of the membrane and see how this alters as it is tensioned. The conclusions drawn from this experiment are that the vibrational energy is more centred in the middle for a tensioned configuration. Also, clear optical diffraction effects were observed and attributed to Fresnel diffraction due to the cavity geometry that forms a suitable aperture (Appendix L). This experiment further confirmed the suspicion of slippage since the membrane did not fracture upon the CD actuator getting "pulled-in".

To come back to the original research question "Does mechanical tensile strain affect the nonlinear dynamic characterization of graphene's Young's modulus". The answer remains unrevealed. The bottleneck that prevents finding the answer is the membrane slipping upon being tensioned. This effectively changed the system parameters (stiffness, pretension, sag) after every experiment until it settled to a configuration where only barely strain is applied. Despite this, the overall result of this work can be regarded positively. Using this new transfer method. New samples can be created with a high success rate. Furthermore, the identified coupling (between the membrane and CD shuttle) and nonlinearities arising from graphene and MEMS give a clear idea of what needs to be incorporated in an expanded mathematical formulation of the system.

5.2. Recommendations

A continuation of this work is recommended. If the original research question is to be answered, one manufacturing issue should inevitably be addressed, namely the clamping. Appendix F proposes a couple of methods that are worth pursuing. The clamping shall prevent slippage of the membrane and thus result in real strain in the membrane. To confirm the magnitude of strain, Raman spectroscopy can be used in the future [44, 86].

The mathematical formulation of the system could be improved upon by incorporating a pre-deformation (w_0) and possibly bending moments. These differential equations can then be numerically integrated, simulated or perturbed to be used to fit the experimentally obtained data.

Lastly, there are different types of MEMS devices available on the die provided in this thesis. These can apply shear and compress in addition to tension. Also, an electrostatic back-gate is provided that can be used to measure capacitive effects or even form another coupled resonator.

Bibliography

[1] Youngkun Ahn et al. “Thermal annealing of graphene to remove polymer residues”. In: *Materials Express* 6.1 (2016), pp. 69–76.

[2] Deji Akinwande et al. “A Review on Mechanics and Mechanical Properties of 2D Materials - Graphene and Beyond”. In: *Extreme Mechanics Letters* 13 (2016).

[3] A. U. Alam, M. M. R. Howlader, and M. J. Deen. “The effects of oxygen plasma and humidity on surface roughness, water contact angle and hardness of silicon, silicon dioxide and glass”. In: *Journal of Micromechanics and Microengineering* 24.3 (2014), p. 035010. ISSN: 0960-1317 1361-6439.

[4] M. Annamalai et al. “Elastic and nonlinear response of nanomechanical graphene devices”. In: *Journal of Micromechanics and Microengineering* 22.10 (2012), p. 105024. ISSN: 0960-1317 1361-6439.

[5] Dario Antonio, Damián H. Zanette, and Daniel López. “Frequency stabilization in nonlinear micromechanical oscillators”. In: *Nature Communications* 3.1 (2012), p. 806. ISSN: 2041-1723.

[6] J. Bauer et al. *Surface tension and adhesion of photo- and electron-beam resists*. Conference Paper. 1997. DOI: 10.1117/12.275865.

[7] P. Blake et al. “Making graphene visible”. In: *Applied Physics Letters* 91.6 (2007), p. 063124.

[8] J. S. Bunch and M. L. Dunn. “Adhesion mechanics of graphene membranes”. In: *Solid State Communications* 152.15 (2012), pp. 1359–1364. ISSN: 0038-1098.

[9] J. Scott Bunch et al. “Electromechanical Resonators from Graphene Sheets”. In: *Science* 315.5811 (2007), pp. 490–493.

[10] Guoxin Cao and Yunpeng Ren. “A paradox in mechanical property characterization of multilayer 2D materials based on existing indentation bending model”. In: *International Journal of Mechanical Sciences* 187 (2020), p. 105912. ISSN: 0020-7403.

[11] Ke Cao et al. “Elastic straining of free-standing monolayer graphene”. In: *Nature Communications* 11.1 (2020), p. 284. ISSN: 2041-1723.

[12] Santiago Cartamil Bueno. “Freestanding 2D Materials and their Applications: From Lab to Fab”. 10.4233/uuid:44e23602-611f-4d43-81b4-f468c80749e0. Thesis. 2017. DOI: 10.4233/uuid:44e23602-611f-4d43-81b4-f468c80749e0. URL: http://resolver.tudelft.nl/uuid:44e23602-611f-4d43-81b4-f468c80749e0.

[13] Santiago J. Cartamil-Bueno et al. “Mechanical characterization and cleaning of CVD single-layer h-BN resonators”. In: *npj 2D Materials and Applications* 1.1 (2017), p. 16. ISSN: 2397-7132.

[14] Andres Castellanos-Gomez et al. “Deterministic transfer of two-dimensional materials by all-dry viscoelastic stamping”. In: *2D Materials* 1.1 (2014), p. 011002. ISSN: 2053-1583.

[15] Andres Castellanos-Gomez et al. “Mechanics of freely-suspended ultrathin layered materials”. In: *Annalen der Physik* 527.1-2 (2015), pp. 27–44. ISSN: 0003-3804.

[16] Andres Castellanos-Gomez et al. “Single-Layer MoS2 Mechanical Resonators”. In: *Advanced Materials* 25.46 (2013), pp. 6719–6723. ISSN: 0935-9648.

[17] A. H. Castro Neto et al. “The electronic properties of graphene”. In: *Reviews of Modern Physics* 81.1 (2009), pp. 109–162.

[18] D. Cattiaux et al. “Geometrical nonlinearity of circular plates and membranes: An alternative method”. In: *Journal of Applied Physics* 128.10 (2020), p. 104501.

[19] Changyao Chen. “Graphene NanoElectroMechanical Resonators and Oscillators”. Thesis. 2013. DOI: https://doi.org/10.7916/D8TT4Z6J.

[20] Changyao Chen et al. “Graphene mechanical oscillators with tunable frequency”. In: *Nature Nanotechnology* 8.12 (2013), pp. 923–927. ISSN: 1748-3395.

[21] Changyao Chen et al. “Performance of monolayer graphene nanomechanical resonators with electrical readout”. In: *Nature Nanotechnology* 4.12 (2009), pp. 861–867. ISSN: 1748-3395.

[22] Yu-Cheng Chiou et al. “Direct Measurement of the Magnitude of the van der Waals Interaction of Single and Multilayer Graphene”. In: *Langmuir* 34.41 (2018), pp. 12335–12343. ISSN: 0743-7463.

[23] J. W. Christopher et al. “Monolayer MoS2 Strained to 1.3% With a Microelectromechanical System”. In: *Journal of Microelectromechanical Systems* 28.2 (2019), pp. 254–263. ISSN: 1941-0158.

[24] D. Davidovikj et al. “Nonlinear dynamic characterization of two-dimensional materials”. In: *Nat Commun* 8.1 (2017), p. 1253. ISSN: 2041-1723 (Electronic) 2041-1723 (Linking).

[25] D. Davidovikj et al. “Visualizing the Motion of Graphene Nanodrums”. In: *Nano Lett* 16.4 (2016), pp. 2768–73. ISSN: 1530-6992 (Electronic) 1530-6984 (Linking).

[26] Dejan Davidovikj et al. “On-chip Heaters for Tension Tuning of Graphene Nanodrums”. In: *Nano Letters* 18.5 (2018), pp. 2852–2858. ISSN: 1530-6984.

[27] S. De, A. Van Der Zande, and N. R. Aluru. “Intrinsic dissipation due to mode coupling in two-dimensional-material resonators revealed through a multiscale approach”. In: *Physical Review Applied* 14.3 (2020). ISSN: 23317019 (ISSN).

[28] R. De Alba et al. “Tunable phonon-cavity coupling in graphene membranes”. In: *Nature Nanotechnology* 11.9 (2016), pp. 741–746. ISSN: 1748-3395.

[29] C. R. Dean et al. “Boron nitride substrates for high-quality graphene electronics”. In: *Nature Nanotechnology* 5.10 (2010), pp. 722–726. ISSN: 1748-3395.

[30] Shikai Deng and Vikas Berry. “Wrinkled, rippled and crumpled graphene: an overview of formation mechanism, electronic properties, and applications”. In: *Materials Today* 19.4 (2016), pp. 197–212. ISSN: 13697021.

[31] electronic Diener. Web Page. URL: https://www.plasma.com/en/cleaning-with-plasma/.

[32] R. J. Dolleman et al. “High-Frequency Stochastic Switching of Graphene Resonators Near Room Temperature”. In: *Nano Letters* 19.2 (2019), pp. 1282–1288. ISSN: 1530-6992 (Electronic) 1530-6984 (Linking).

[33] R. J. Dolleman et al. “Squeeze-Film Effect on Atomically Thin Resonators in the High-Pressure Limit”. In: *Nano Letters* 21.18 (2021), pp. 7617–7624. ISSN: 15306984 (ISSN).

[34] Robin J. Dolleman et al. “Amplitude calibration of 2D mechanical resonators by nonlinear optical transduction”. In: *Applied Physics Letters* 111.25 (2017), p. 253104.

[35] Robin J. Dolleman et al. “Mass measurement of graphene using quartz crystal microbalances”. In: *Applied Physics Letters* 115.5 (2019), p. 053102. ISSN: 0003-6951.

[36] Robin J. Dolleman et al. “Opto-thermally excited multimode parametric resonance in graphene membranes”. In: *Scientific Reports* 8.1 (2018), p. 9366. ISSN: 2045-2322.

[37] Alexander Eichler et al. “Parametric Amplification and Self-Oscillation in a Nanotube Mechanical Resonator”. In: *Nano Letters* 11.7 (2011), pp. 2699–2703. ISSN: 1530-6984.

[38] I. W. Frank et al. “Mechanical properties of suspended graphene sheets”. In: *Journal of Vacuum Science & Technology B: Microelectronics and Nanometer Structures Processing, Measurement, and Phenomena* 25.6 (2007), pp. 2558–2561. ISSN: 1071-1023.

[39] Riccardo Frisenda et al. “Recent progress in the assembly of nanodevices and van der Waals heterostructures by deterministic placement of 2D materials”. In: *Chemical Society Reviews* 47.1 (2018), pp. 53–68. ISSN: 0306-0012.

[40] A. K. Geim and K. S. Novoselov. “The rise of graphene”. In: *Nature Materials* 6.3 (2007), pp. 183–191. ISSN: 1476-4660.

[41] MicroChemicals GmbH. *Substrate Preparation*. Web Page. 2022. URL: `https://www.microchemicals.com/technical_information/substrate_cleaning_adhesion_photoresist.pdf`.

[42] M. Goldsche et al. “Fabrication of comb-drive actuators for straining nanostructured suspended graphene”. In: *Nanotechnology* 29.37 (2018), p. 375301. ISSN: 1361-6528 (Electronic) 0957-4484 (Linking).

[43] Matthias Goldsche et al. “Low-temperature compatible electrostatic comb-drive actuators with integrated graphene”. In: pp. 251–255.

[44] Matthias Goldsche et al. “Tailoring Mechanically Tunable Strain Fields in Graphene”. In: *Nano Letters* 18 (2017).

[45] HQ-Graphene. Web Page. URL: `http://www.hqgraphene.com/TransferSystem.php`.

[46] Fen Guan et al. “Tuning strain in flexible graphene nanoelectromechanical resonators”. In: *Applied Physics Letters* 107.19 (2015), p. 193102. ISSN: 0003-6951.

[47] Johannes Güttinger et al. “Energy-dependent path of dissipation in nanomechanical resonators”. In: *Nature Nanotechnology* 12.7 (2017), pp. 631–636. ISSN: 1748-3395.

[48] A. Z. Hajjaj et al. “Linear and nonlinear dynamics of micro and nano-resonators: Review of recent advances”. In: *International Journal of Non-Linear Mechanics* 119 (2020), p. 103328. ISSN: 0020-7462.

[49] V. Harinarayana and Y. C. Shin. “Two-photon lithography for three-dimensional fabrication in micro/nanoscale regime: A comprehensive review”. In: *Optics & Laser Technology* 142 (2021), p. 107180. ISSN: 0030-3992.

[50] William S. Harley et al. “Advances in biofabrication techniques towards functional bioprinted heterogeneous engineered tissues: A comprehensive review”. In: *Bioprinting* 23 (2021), e00147. ISSN: 2405-8866.

[51] B. D. Hauer et al. “A general procedure for thermomechanical calibration of nano/micro-mechanical resonators”. In: *Annals of Physics* 339 (2013), pp. 181–207. ISSN: 0003-4916.

[52] Izak de Heer. “Studying the effect of strain on the mechanical properties of wrinkled graphene”. Thesis. 2022.

[53] Vesa-Matti Hiltunen et al. “Ultrastiff graphene”. In: *npj 2D Materials and Applications* 5.1 (2021), p. 49. ISSN: 2397-7132.

[54] S. Huang et al. “Single-layer graphene membranes by crack-free transfer for gas mixture separation”. In: *Nat. Commun.* 9 (2018), p. 2632.

[55] Zhujun Huang et al. “Versatile construction of van der Waals heterostructures using a dual-function polymeric film”. In: *Nature Communications* 11.1 (2020), p. 3029. ISSN: 2041-1723.

[56] Md Akibul Islam et al. “Exfoliation mechanisms of 2D materials and their applications”. In: *Applied Physics Reviews* 9.4 (2022), p. 041301.

[57] Stoffel D. Janssens et al. “Boundary curvature effect on the wrinkling of thin suspended films”. In: *Applied Physics Letters* 116.19 (2020), p. 193702.

[58] Lei Jiang et al. “Surface wettability of oxygen plasma treated porous silicon”. In: *J. Nanomaterials* 2014 (2014), Article 8. ISSN: 1687-4110.

[59] Fernando de Juan, Juan L. Mañes, and María A. H. Vozmediano. “Gauge fields from strain in graphene”. In: *Physical Review B* 87.16 (2013), p. 165131. ISSN: 1098-0121 1550-235X.

[60] J. Juillard et al. “Ultimate Limits of Differential Resonant MEMS Sensors Based on Two Coupled Linear Resonators”. In: *IEEE Transactions on Ultrasonics, Ferroelectrics, and Frequency Control* 65.12 (2018), pp. 2440–2448. ISSN: 1525-8955.

[61] S. Kalem et al. “Controlled thinning and surface smoothening of silicon nanopillars”. In: *Nanotechnology* 20.44 (2009), p. 445303. ISSN: 0957-4484.

[62] Ata Keşkekler et al. “Tuning nonlinear damping in graphene nanoresonators by parametric-direct internal resonance”. In: *Nature Communications* 12.1 (2021), p. 1099. ISSN: 2041-1723.

[63] Donghwan Kim et al. “Wettability of graphene and interfacial water structure”. In: *Chem* 7.6 (2021), pp. 1602–1614. ISSN: 2451-9294.

[64] Kei Kinoshita et al. “Dry release transfer of graphene and few-layer h-BN by utilizing thermoplasticity of polypropylene carbonate”. In: *npj 2D Materials and Applications* 3.1 (2019), p. 22. ISSN: 2397-7132.

[65] Jan N. Kirchhof et al. *Nanomechanical spectroscopy of 2D materials*. Electronic Article. Mar. 2022. URL: https://ui.adsabs.harvard.edu/abs/2022arXiv220307025K.

[66] Lakshmi S. Kocherlakota, Brad A. Krajina, and René M. Overney. “Communication: Local energetic analysis of the interfacial and surface energies of graphene from the single layer to graphite”. In: *The Journal of Chemical Physics* 143.24 (2015), p. 241105. ISSN: 0021-9606.

[67] S. P. Koenig et al. “Ultrastrong adhesion of graphene membranes”. In: *Nat Nanotechnol* 6.9 (2011), pp. 543–6. ISSN: 1748-3387.

[68] I. Kozinsky et al. “Tuning nonlinearity, dynamic range, and frequency of nanomechanical resonators”. In: *Applied Physics Letters* 88.25 (2006), p. 253101.

[69] E. Kramer et al. “Strain-dependent damping in nanomechanical resonators from thin MoS2 crystals”. In: *Applied Physics Letters* 107.9 (2015). ISSN: 0003-6951 1077-3118.

[70] C. Lee et al. “Measurement of the elastic properties and intrinsic strength of monolayer graphene”. In: *Science* 321.5887 (2008), pp. 385–8. ISSN: 1095-9203 (Electronic) 0036-8075 (Linking).

[71] Martin Lee et al. “Sealing Graphene Nanodrums”. In: *Nano Letters* 19.8 (2019), pp. 5313–5318. ISSN: 1530-6984.

[72] Max C. Lemme et al. “Nanoelectromechanical Sensors Based on Suspended 2D Materials”. In: *Research* 2020 (2020), p. 8748602. ISSN: null.

[73] Yung-Chang Lin et al. “Graphene Annealing: How Clean Can It Be?” In: *Nano Letters* 12.1 (2012), pp. 414–419. ISSN: 1530-6984.

[74] H. Liu et al. *Tension tuning of sound and heat transport in graphene*. Electronic Article. Apr. 2022. URL: https://ui.adsabs.harvard.edu/abs/2022arXiv220406877L.

[75] J. H. Los, A. Fasolino, and M. I. Katsnelson. “Mechanics of thermally fluctuating membranes”. In: *npj 2D Materials and Applications* 1.1 (2017). ISSN: 2397-7132.

[76] Gerrit A. Luinstra and Endres Borchardt. “Material Properties of Poly(Propylene Carbonates)”. In: *Synthetic Biodegradable Polymers*. Ed. by Bernhard Rieger et al. Berlin, Heidelberg: Springer Berlin Heidelberg, 2012, pp. 29–48. ISBN: 978-3-642-27154-0. DOI: 10.1007/12_2011_126. URL: https://doi.org/10.1007/12_2011_126.

[77] R. Lukose et al. “Influence of plasma treatment on SiO2/Si and Si3N4/Si substrates for large-scale transfer of graphene”. In: *Scientific Reports* 11.1 (2021), p. 13111. ISSN: 2045-2322.

[78] E. H. Mansfield. *The bending and stretching of plates*. 1989.

[79] T. M. G. Mohiuddin et al. “Uniaxial strain in graphene by Raman spectroscopy: *G* peak splitting, Grüneisen parameters, and sample orientation”. In: *Physical Review B* 79.20 (2009), p. 205433.

[80] Fehmi Najar et al. “Parametric resonance of bi-directional axial loads shallow arch microresonators”. In: *Journal of Micromechanics and Microengineering* 32.5 (2022), p. 054004. ISSN: 0960-1317 1361-6439.

[81] R. J. Nicholl et al. “The effect of intrinsic crumpling on the mechanics of free-standing graphene”. In: *Nat Commun* 6 (2015), p. 8789. ISSN: 2041-1723.

[82] R. J. T. Nicholl et al. “Hidden Area and Mechanical Nonlinearities in Freestanding Graphene”. In: *Phys Rev Lett* 118.26 (2017), p. 266101. ISSN: 1079-7114 (Electronic) 0031-9007 (Linking).

[83] P. J. Olver. *The Calculus of Variations*. 2021.

[84] M. M. Parmar, P. R. Yasasvi Gangavarapu, and A. K. Naik. “Dynamic range tuning of graphene nanoresonators”. In: *Applied Physics Letters* 107.11 (2015), p. 113108.

[85] H. Hugo Pérez Garza et al. “Controlled, Reversible, and Nondestructive Generation of Uniaxial Extreme Strains (>10%) in Graphene”. In: *Nano Letters* 14.7 (2014), pp. 4107–4113. ISSN: 1530-6984.

[86] Héctor Hugo Pérez-Garza et al. “Highly strained graphene samples of varying thickness and comparison of their behaviour”. In: *Nanotechnology* 25.46 (2014), p. 465708. ISSN: 0957-4484 1361-6528.

[87] Filippo Pizzocchero et al. “The hot pick-up technique for batch assembly of van der Waals heterostructures”. In: *Nature Communications* 7.1 (2016), p. 11894. ISSN: 2041-1723.

[88] P. M. Polunin et al. “Characterization of MEMS Resonator Nonlinearities Using the Ringdown Response”. In: *Journal of Microelectromechanical Systems* 25.2 (2016), pp. 297–303. ISSN: 1941-0158.

[89] M. Poot and H. S. J. van der Zant. “Nanomechanical properties of few-layer graphene membranes”. In: *Applied Physics Letters* 92.6 (2008), p. 063111.

[90] Parmeshwar Prasad, Nishta Arora, and A. K. Naik. “Parametric amplification in MoS2 drum resonator”. In: *Nanoscale* 9.46 (2017), pp. 18299–18304. ISSN: 2040-3364.

[91] Huasong Qin et al. “Mechanical properties of wrinkled graphene generated by topological defects”. In: *Carbon* 108 (2016), pp. 204–214. ISSN: 0008-6223.

[92] Sami Ramadan et al. “Enhancing Structural Properties and Performance of Graphene-Based Devices Using Self-Assembled HMDS Monolayers”. In: *ACS Omega* 6.7 (2021), pp. 4767–4775.

[93] B. Sajadi et al. “Experimental characterization of graphene by electrostatic resonance frequency tuning”. In: *J. Appl. Phys.* 122.23 (2017), p. 234302. ISSN: 0021-8979.

[94] C. Samanta, N. Arora, and A. K. Naik. “Tuning of geometric nonlinearity in ultrathin nanoelectromechanical systems”. In: *Applied Physics Letters* 113.11 (2018), p. 113101. ISSN: 0003-6951.

[95] Ali Sarafraz et al. “Nonlinear elasticity of wrinkled atomically thin membranes”. In: *Journal of Applied Physics* 130.18 (2021), p. 184302.

[96] Grégory F. Schneider et al. “Wedging Transfer of Nanostructures”. In: *Nano Letters* 10.5 (2010), pp. 1912–1916. ISSN: 1530-6984.

[97] Ali Shariati et al. “On the nonlinear dynamics of viscoelastic graphene sheets conveying nanoflow: Parametric excitation analysis”. In: *Mechanics Based Design of Structures and Machines* (2020), pp. 1–18. ISSN: 1539-7734.

[98] V. Singh et al. “Probing thermal expansion of graphene and modal dispersion at low-temperature using graphene nanoelectromechanical systems resonators”. In: *Nanotechnology* 21.16 (2010), p. 165204. ISSN: 0957-4484.

[99] Vibhor Singh et al. “Negative nonlinear damping of a multilayer graphene mechanical resonator”. In: *Physical Review B* 93.24 (2016), p. 245407.

[100] Makars Šiškins et al. “Sensitive capacitive pressure sensors based on graphene membrane arrays”. In: *Microsystems & Nanoengineering* 6.1 (2020), p. 102. ISSN: 2055-7434.

[101] A. D. Smith et al. “Piezoresistive properties of suspended graphene membranes under uniaxial and biaxial strain in nanoelectromechanical pressure sensors”. In: *ACS Nano* 10 (2016), p. 9879.

[102] Suhan Son et al. “Strongly adhesive dry transfer technique for van der Waals heterostructure”. In: *2D Materials* 7.4 (2020), p. 041005. ISSN: 2053-1583.

[103] Xuefeng Song et al. “Stamp Transferred Suspended Graphene Mechanical Resonators for Radio Frequency Electrical Readout”. In: *Nano Letters* 12.1 (2012), pp. 198–202. ISSN: 1530-6984.

[104] J. Sonntag et al. “Engineering Tunable Strain Fields in Suspended Graphene by Microelectromechanical Systems”. In: *2019 20th International Conference on Solid-State Sensors, Actuators and Microsystems & Eurosensors XXXIII (TRANSDUCERS & EUROSENSORS XXXIII)*, pp. 266–269. ISBN: 2167-0021.

[105] Peter G. Steeneken et al. “Dynamics of 2D material membranes”. In: *2D Materials* 8.4 (2021). ISSN: 2053-1583.

[106] G. Strang. “Calculus of Variations chapter”. In: 2006.

[107] Z. J. Su et al. “Tunable parametric amplification of a graphene nanomechanical resonator in the nonlinear regime”. In: *Nanotechnology* 32.15 (2021), p. 155203. ISSN: 1361-6528 (Electronic) 0957-4484 (Linking).

[108] P. Z. Sun et al. “Limits on gas impermeability of graphene”. In: *Nature* 579.7798 (2020), pp. 229–232. ISSN: 1476-4687.

[109] Amorn Thedsakhulwong and Warawoot Thowladda. “Removal of Carbon Contamination on Silicon Wafer Surfaces by Microwave Oxygen Plasma”. In: 18 (2008).

[110] Floriano Traversi et al. “Elastic properties of graphene suspended on a polymer substrate by e-beam exposure”. In: *New Journal of Physics* 12.2 (2010), p. 023034. ISSN: 1367-2630.

[111] Richard Van Noorden. “Production: Beyond sticky tape”. In: *Nature* 483.7389 (2012), S32–S33. ISSN: 1476-4687.

[112] Warner J. Venstra, Hidde J. R. Westra, and Herre S. J. van der Zant. “Stochastic switching of cantilever motion”. In: *Nature Communications* 4.1 (2013), p. 2624. ISSN: 2041-1723.

[113] G. J. Verbiest et al. “Tunable coupling of two mechanical resonators by a graphene membrane”. In: *2D Materials* 8.3 (2021). ISSN: 2053-1583.

[114] G. J. Verbiest et al. “Tunable mechanical coupling between driven microelectromechanical resonators”. In: *Applied Physics Letters* 109.14 (2016), p. 143507.

[115] Gerard Verbiest et al. “Detecting Ultrasound Vibrations by Graphene Resonators”. In: *Nano Letters* 18 (2018).

[116] D. V. Vertyanov et al. “Effects of Gold-aluminum Intermetallic Compounds on Chip Wire Bonding Interconnections Reliability”. In: *2020 IEEE Conference of Russian Young Researchers in Electrical and Electronic Engineering (EIConRus)*, pp. 2216–2220. ISBN: 2376-6565.

[117] S. Wagner et al. “Graphene transfer methods for the fabrication of membrane-based NEMS devices”. In: *Microelectronic Engineering* 159 (2016), pp. 108–113. ISSN: 0167-9317.

[118] P. Weber et al. “Coupling graphene mechanical resonators to superconducting microwave cavities”. In: *Nano Lett* 14.5 (2014), pp. 2854–60. ISSN: 1530-6984.

[119] ZiXiong Wei et al. “Peeling of graphene/molybdenum disulfide heterostructure at different angles: A continuum model with accommodations for van der Waals interaction”. In: *Composites Part A: Applied Science and Manufacturing* 150 (2021), p. 106592. ISSN: 1359-835X.

[120] M. Will et al. “High Quality Factor Graphene-Based Two-Dimensional Heterostructure Mechanical Resonator”. In: *Nano Letters* 17.10 (2017), pp. 5950–5955. ISSN: 1530-6984.

[121] C. L. Wong et al. “Characterization of nanomechanical graphene drum structures”. In: *Journal of Micromechanics and Microengineering* 20.11 (2010), p. 115029. ISSN: 0960-1317 1361-6439.

[122] Yong Xie et al. “Straining and Tuning Atomic Layer Nanoelectromechanical Resonators via Comb-Drive MEMS Actuators”. In: *Advanced Materials Technologies* 6.2 (2021), p. 2000794. ISSN: 2365-709X.

[123] Fan Yang et al. “Spatial Modulation of Nonlinear Flexural Vibrations of Membrane Resonators”. In: *Physical Review Letters* 122.15 (2019), p. 154301.

[124] Yue Ying et al. “Sliding nanomechanical resonators”. In: *Nature Communications* 13.1 (2022), p. 6392. ISSN: 2041-1723.

[125] Stav Zaitsev et al. “Nonlinear damping in a micromechanical oscillator”. In: *Nonlinear Dynamics* 67.1 (2012), pp. 859–883. ISSN: 1573-269X.

[126] Hang Zhang et al. “Transport in suspended monolayer and bilayer graphene under strain: A new platform for material studies”. In: *Carbon* 69 (2014), pp. 336–341. ISSN: 0008-6223.

[127] Q. Zhang et al. “Adhesion Behavior of Graphene Exfoliated from Silicon Substrate by Atomic Calculation”. In: *2018 IEEE 13th Annual International Conference on Nano/Micro Engineered and Molecular Systems (NEMS)*, pp. 532–537. ISBN: 2474-3755.

A

Rougness analysis MEMS device and coating

In an attempt to decrease surface roughness to improve membrane-to-substrate adhesion, the MEMS device was coated in a layer of gold (Au). The idea is opposite as described in Section 2.2.2. Instead of removing material to form a flat surface, it is added. The deposition consists of a 5 nm layer of chrome (Cr) followed with a 100 nm layer Au. Depositing the materials is done by evaporating them in a chamber using an electron beam (E-beam) with the MEMS device close by. The Cr is there to perform adhesion between the SiO_2 and Au This deposition process was performed by Roberto Pezone MSc. Since the deposition can be thought of as a flow of particles approaching non-laminarly from the top, the expected result is that the deep trenches of the roughness profile will "catch" more deposits than the peaks. This is somewhat the reverse of what was expected from etching. The expected behaviour of this coating is shown in Figure A.1.

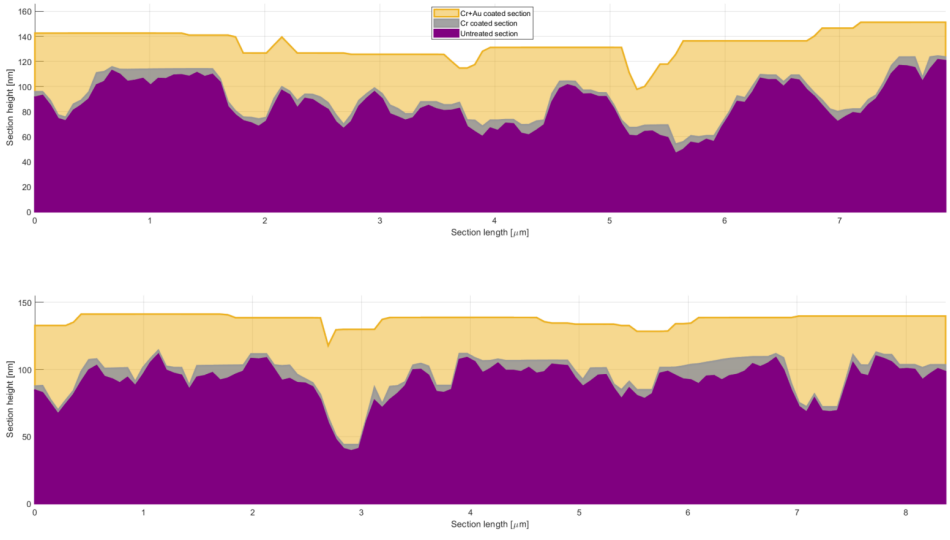

Figure A.1: Simulation on raw AFM data indicating how a coating treatment would alter surface roughness of SiO_2 for two different profile lines. Gray indicates the Cr layer and yellow indicates the Au layer.

After performing this deposition, the devices were inspected by means of atomic force microscopy (AFM). These AFM measurements pointed out that quite the contrary had occurred. These measurements are depicted in Figure A.2.

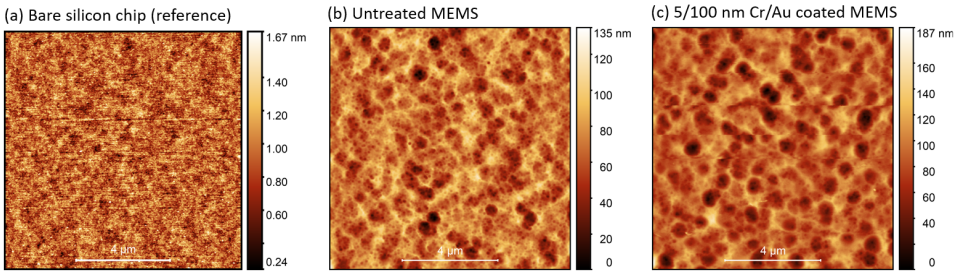

Figure A.2: AFM measurements of (a) Bare Si with 600 nm SiO_2. (b) Untreated MEMS device. (c) Coated MEMS device.

The goal was to reduce roughness to promote adhesion. A glance at the colour bar in Figure A.2 (b&c) shows that the difference between high and low has most certainly not decreased. If anything, it has increased. Also, the "pitted"/"bombarded" structure remains similar. It seems that the Au particles did not deposit into the pits as expected and rather preferred to stick to the sides of the pits which in turn made the pits even deeper. There exist many methods to quantify a surface's roughness but such analysis is not required here. A possible improvement that could be made is to deposit a thicker Au coating, although the outcome of that can be drawn into question when this relatively thin coating has shown no signs of improvement. Furthermore, no noticeable improvement in the adhesion of graphene to gold was observed.

Besides the fact that roughness had not improved, another problem arose due to the Au coating. A gold-aluminium intermetallic is formed where the Au coating meets the edges of the Al bond pads, as depicted in Figure A.3. There are several types of such Au−Al intermetallics. Several types exist such as Au_5Al_2 and $AuAl_2$ (known as white- and purple plague in the Semicon industry), but other forms exist as well. Irrespective of which intermetallic is present at hand here, they all share similar undesirable properties. Such as poor electrical conductivity and volume reduction compared to separate metals, hence creating cavities. A mix of these intermettalic compounds is likely to be present as this tends to occur at the annealing temperature that was used (305 °C) [116].

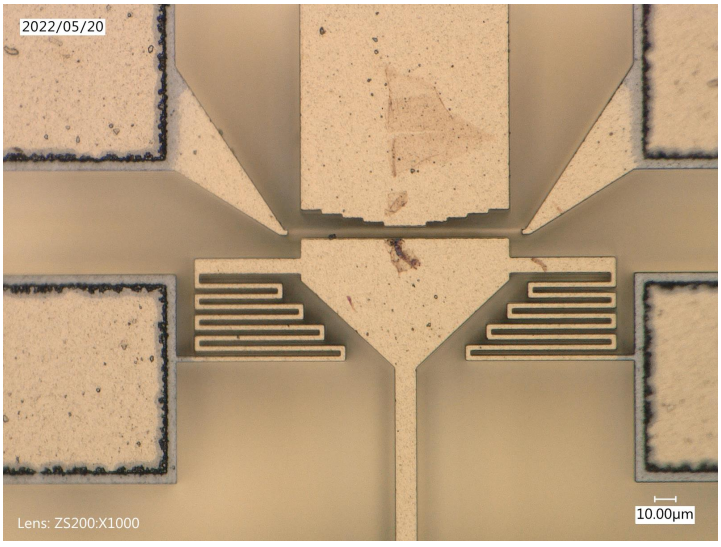

Figure A.3: Formation of Aluminum-Gold Intermetallics visible after annealing the device that was Au coated.

B

Graphene transfer

The following section aims to sketch a visual idea for the reader into what it looks like to transfer the graphene onto such a fragile MEMS device with poor surface adhesion. To start, there is the setup used for the transfer. This setup is depicted in Figure B.1. The basic principle of operation is that there are two parties, a target substrate (bottom) and a donor stamp (top). This stage can precisely position these two parties w.r.t. each other with sub-micrometre precision in all desired degrees of freedom (DOF). Furthermore, this setup can control the temperature of the target substrate on the bottom plate. The top stamp is clamped in place whereas the target substrate is often too fragile for this so it is held in place by a vacuum cavity. A digital microscope is mounted from the top in order to observe the target substrate. Logically to do so, the stamp must be (largely) transparent.

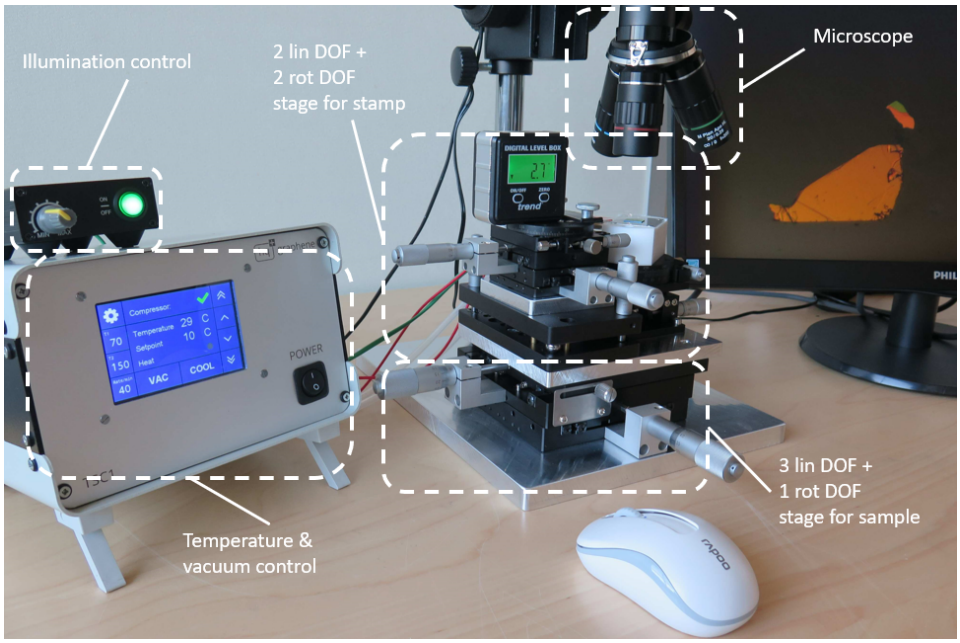

Figure B.1: 2D material transfer setup. Adapted from retailers website [45].

Figure B.2 depicts what it looks like to stamp in this case a graphene membrane onto the fragile MEMS device. From B.2 (a-c) it can be seen how to flake is brought into contact with the substrate. The actual contact area turns in this case into a dark shade of green. In B.2 (d&e) it can be seen how the heated substrate causes the PPC film to melt along the edges of the contact area. Subsequently in B.2 (f-h) is shown how this

area separates from the film and thus stays behind on the target substrate along with the desired material.

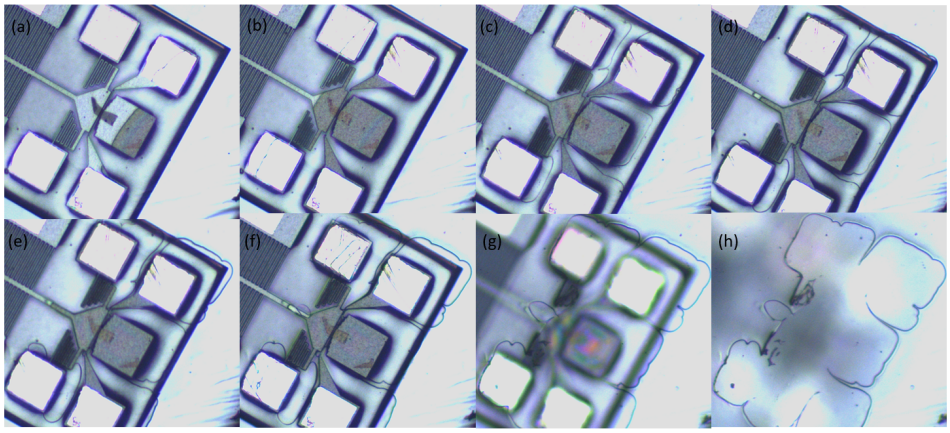

Figure B.2: (a-g) Chronologic representation of what it looks like to stamp the graphene onto the MEMS device where it can be seen that the PPC film on the transfer stamp locally gets transferred along with the graphene flake.

With the transfer of the 2D material completed, some post-processing is required. To remove the PPC polymer, the sample is annealed in a setup depicted in Figure B.3. The annealing process is schematically shown in Figure 2.11. This setup consists of a quartz tube in which the sample is loaded. The pressure in this tube is reduced to a pressure in the order of 1e−8 mbar using 2 different vacuum pumps. Then the sample is constantly flushed with a small flow of Ar gas (≈ 100 ml/min) to prevent the decomposing polymer from reacting with O_2. With the exterior conditions in place, the sample is heated by moving the heater along the tube onto the sample. Once the sample has been exposed to the desired temperature for the desired length of time, the heater is turned off and slowly (± 6 hours) cools down to room temperature to prevent a thermal shock to the MEMS device.

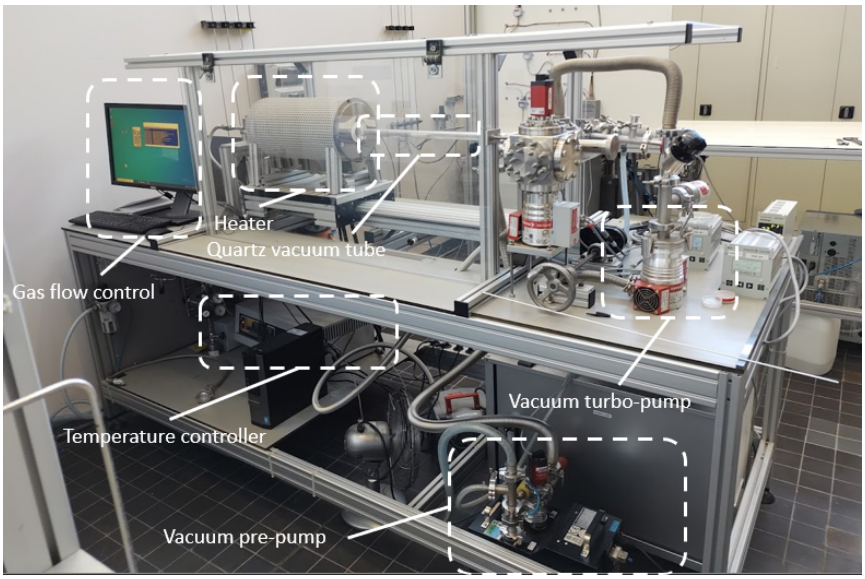

Figure B.3: Photograph of the annealing setup.

Before it was established that this functioned properly, the same process was performed with an overpressure of Ar gas which consumed a lot more than the improved method as portrayed in Figure 2.11. Effectively the only difference turns out to be the direction

of the gas flow, which is arbitrary. The annealing process has only returned good results as can be seen in Figure B.4.

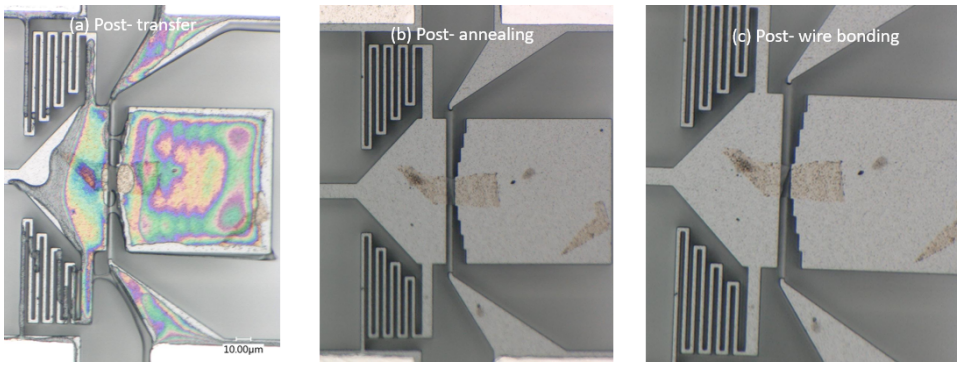

Figure B.4: Images of the MEMS device (a) directly after the transfer (b) after annealing (c) after wire-bonding.

C

Derivation of the Equations of Motion

To explain the experimental data that was obtained, a model describing the dynamical behaviour is required. Such a model in this project will be a set of differential equations referred to as the Equations of Motion (EoM). To obtain them, the first step is to make a schematic of the situation at hand with the relevant forces and displacements. This is depicted in Figure C.1. Note that the system is modelled in 2 dimensions ($\boldsymbol{x}$&$\boldsymbol{z}$). Here it is shown that there are three degrees of freedom (DoFs) where $u(x,t)$ is the axial component, $w(x,t)$ is the transverse displacement and $u_l(x,t)|_{x=l} = u_l(l,t)$ is the displacement of the comb-drive.

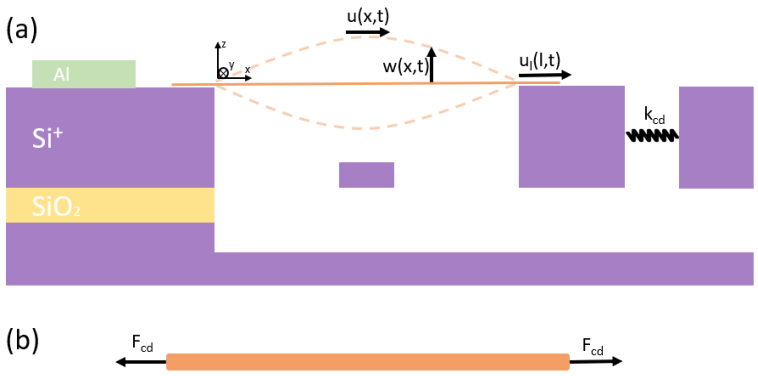

Figure C.1: (a) Illustration of system with relevant degrees of freedom and (b) a free-body diagram of the suspended 2D material flake.

In order to now derive the EoM, the path of Lagrangian mechanics is chosen. The EoM for each respective DoF ($\boldsymbol{q} = [u; w; u_l]$) in its most compact form is given by.

$$\frac{\mathrm{d}}{\mathrm{d}t}\left(\frac{\partial \mathscr{L}}{\partial \dot{\boldsymbol{q}}_i}\right) = \frac{\partial \mathscr{L}}{\partial \boldsymbol{q}_i} \tag{C.1}$$

Where $\mathscr{L}$ is what is known as the Lagrangian. This is described as the kinetic energy of a system (T) minus the potential energy (V). Which in this particular system can be

described by the following expressions.

$$T = \frac{1}{2}\int_0^l m(\dot{u}^2 + \dot{w}^2)\mathrm{d}x + \frac{1}{2}M\dot{u}_l \tag{C.2}$$

$$V = \frac{1}{2}EA\int_0^l \varepsilon_s^2\mathrm{d}x + \frac{1}{2}ku_l^2 + F_{cd}u_l \tag{C.3}$$

The terms in these equations have physical representations. The dot $\dot{}$ denotes a derivation w.r.t. time and a prime $'$ w.r.t. the axial DoF x. The first term in T; ($\frac{1}{2}\int_0^l m(\dot{u}^2 + \dot{w}^2)\mathrm{d}x$) is the kinetic energy of the membrane in axial and transverse directions where m is the mass of the membrane. The second term here ($\frac{1}{2}M\dot{u}_l$) denotes the kinetic energy of the suspended comb-drive in the axial direction where M is the mass of the comb-drive which is much larger than that of the membrane ($M \gg m$). The first term in V; ($\frac{1}{2}EA\int_0^l \varepsilon_s^2\mathrm{d}x$) represents the strain energy in the membrane which deflects both in- and out-of-plane. Here, the strain ($\varepsilon_s = u' + \frac{1}{2}w'^2 + \varepsilon_0$) where the first two terms ($u' + \frac{1}{2}w'$) follow from the Föppl-von Kármán equations plus an added compressive pre-strain term (ε_0) since this is what determines the out-of-plane stiffness for a membrane since there practically zero bending stiffness [57, 113]. It is because of this that there is no bending energy term ($\frac{1}{2}EI\int_0^l \varepsilon_b^2\mathrm{d}x$) in the potential energy. The second term ($\frac{1}{2}ku_l^2$) is the elastic spring energy stored in the folded-beam flexures that attach to the comb drive with a specific linear stiffness k as derived in Chapter 2.1.1. The last term ($F_{cd}u_l$) is the work done by the system. Now that the energy terms are known, they can be plugged into Equation C.1 to yield the following equation that needs to be solved for the three DoFs.

$$\frac{\mathrm{d}}{\mathrm{d}t}\left(\frac{\partial T}{\partial \dot{\boldsymbol{q}}_i}\right) + \frac{\partial V}{\partial \boldsymbol{q}_i} = 0 \tag{C.4}$$

The first term in this equation ($\frac{\mathrm{d}}{\mathrm{d}t}\left(\frac{\partial T}{\partial \dot{\boldsymbol{q}}_i}\right)$) is easily solved for the three DoFs and yields respectively.

$$\frac{\mathrm{d}}{\mathrm{d}t}\left(\frac{\partial T}{\partial \dot{u}}\right) = m\ddot{u} \tag{C.5}$$

$$\frac{\mathrm{d}}{\mathrm{d}t}\left(\frac{\partial T}{\partial \dot{u}_l}\right) = M\ddot{u}_l \tag{C.6}$$

$$\frac{\mathrm{d}}{\mathrm{d}t}\left(\frac{\partial T}{\partial \dot{w}}\right) = m\ddot{w} \tag{C.7}$$

For the second term in the Lagrange equation ($\frac{\partial V}{\partial \boldsymbol{q}_i}$) things become a bit more complicated. Since the function for the potential energy contains terms in the form of $\int_0^l \frac{\partial u(x,t)}{\partial x}\&\frac{\partial w(x,t)}{\partial x}\mathrm{d}x$ and their derivative is required with respect to $u(x,t)\&w(x,t)$. This is a problem addressed in the mathematical department known as the calculus of variations. Here calculus problems can be addressed that are in complicated forms such as.

$$P(y(x)) = \int F(x, u(x), u'(x))\mathrm{d}x \tag{C.8}$$

For the problem at hand, it is slightly less complicated since the potential energy function only contains a derivative.

$$P(u,w) = \frac{1}{2}EA\int_0^l \varepsilon_s^2 \mathrm{d}x = \frac{1}{2}EA\int_0^l \left(\frac{\partial u(x,t)}{\partial x} + \frac{1}{2}\frac{\partial w(x,t)}{\partial x}^2 + \varepsilon_0\right)^2 \mathrm{d}x \tag{C.9}$$

$$= \frac{1}{2}EA\left(\int_0^l u'^2\mathrm{d}x + \int_0^l u'\frac{1}{2}w'^2\mathrm{d}x + \int_0^l 2\varepsilon_0 u'\mathrm{d}x + \frac{1}{4}\int_0^l w'^4\mathrm{d}x + \int_0^l \varepsilon_0 w'^2\mathrm{d}x + \int_0^l \varepsilon_0^2\mathrm{d}x\right) \tag{C.10}$$

Since we are dealing with a type of minimization problem, the point (or function in this case) is sought after for which the derivative is 0, indicating an extremum. Typically this is a minimum in such physical systems. For the system $P(u)$ this would be $P'(u) = \frac{\partial P(u)}{\partial u}$ and is referred to as the "first variation" or the "Euler-Lagrange equation" and can be expressed in a strong and a weak form. The weak form is particularly useful in Finite Element Methods (FEM) [83, 106]. In order to find this derivative one shall perform a thought experiment. When there is a function that describes the minimal energy path connecting two points w.r.t. to some kind of gradient field. This minimal function can be perturbed slightly by a test function $\delta u(x,t)$. Such that $P(u) \longrightarrow P(u+\delta u)$. Then by comparing $P(u)$ to $P(u+\delta u)$ there will be a term in the difference which is linearly dependent on δu, which must be zero. This term is then the derivative that was sought after. Such variation is depicted in Figure C.2.

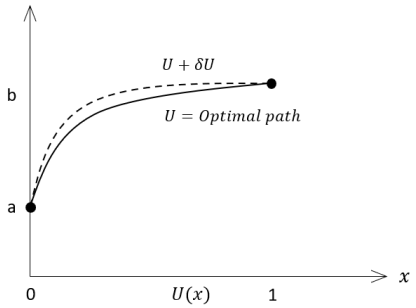

Figure C.2: Principle illustrating the perturbation of the optimal path, note that the begin- and endpoints coincide i.e. the variation is zero here

The derivation for this variation can be for a generic set of equations as shown in Equations C.11 to C.16

$$P(U) = \int_0^1 F(U,U')\mathrm{d}x \quad U(0) = a \;\&\; U(1) = b \tag{C.11}$$

$$\textbf{Inside integral } F(U+\delta U, U'+\delta U') = F(U,U') + \delta U\frac{\partial F}{\partial u} + \delta U'\frac{\partial F}{\partial U'} + \;\ldots \tag{C.12}$$

$$\textbf{After integrating } P(U+\delta U) = P(U) + \int_0^1 \left(\delta U\frac{\partial F}{\partial U} + \delta U'\frac{\partial F}{\partial U'}\right)\mathrm{d}x \tag{C.13}$$

$$\textbf{Weak form } \frac{\partial P}{\partial U} = \int_0^1 \left(\delta U\frac{\partial F}{\partial U} + \delta U'\frac{\partial F}{\partial U'}\right)\mathrm{d}x = 0 \quad \text{for all } \delta U \tag{C.14}$$

Since an expression is required for which a variation of δU yields zero, the weak form needs to be converted such that $\delta U' \longrightarrow \delta U$. This is taken care of by integrating by parts to yield the following.

$$\textbf{Weak form - By parts } \frac{\partial P}{\partial U} = \int_0^1 \left(\delta U\frac{\partial F}{\partial U} - \delta U\frac{\mathrm{d}}{\mathrm{d}x}\left(\frac{\partial F}{\partial U'}\right)\right)\mathrm{d}x + \left[\delta U\frac{\partial F}{\partial U'}\right]_0^1 = 0 \tag{C.15}$$

Extra care should be taken in performing mathematical operations correctly i.e. use of the chain rule in the $-\delta U\frac{\mathrm{d}}{\mathrm{d}x}\left(\frac{\partial F}{\partial U'}\right)$ term. This weak form allows to δU term simply to

be factored out and leave the expression for $\frac{\partial P}{\partial U}$ which was sought for in the Lagrange equations. Depending on the boundary conditions, this weak form can be further simplified to obtain the so-called "strong form"/"Euler-Lagrange equation" Recall that the variation must be zero at begin- and endpoints as shown in Figure C.2. The boundary conditions containing the term ($\left[\delta U \frac{\partial F}{\partial U'}\right]_0^1$) then disappear and yields the strong form.

$$\textbf{Strong form}\ \frac{\partial P}{\partial U} = \frac{\partial F}{\partial U} - \frac{\mathrm{d}}{\mathrm{d}x}\left(\frac{\partial F}{\partial U'}\right) = 0 \tag{C.16}$$

Now returning to the problem of the strained membrane that was being investigated. There are six terms in the integral describing the strain energy stored as potential energy. Unfortunately, the strong form can not be directly applied. This is because we are not sure about the boundary condition at the end of the membrane $U_l = l + \delta l$. Which depends on the tension in the membrane and the force from the comb drive, which in turn depends on the displacement of the comb drive. The boundary condition term, therefore, contains important information that cannot be neglected.

With this knowledge, it is now possible to solve the potential energy term in the Lagrange equation C.1 ($\frac{\partial V}{\partial \boldsymbol{q}_i}$). The terms that follow from this are such.

$$\frac{\partial V}{\partial u} = -EA\varepsilon_s' \tag{C.17}$$
$$\frac{\partial V}{\partial u_l} = ku_l + EA\varepsilon_s - F_{cd} \tag{C.18}$$
$$\frac{\partial V}{\partial w} = -EA(\varepsilon_s w')' \tag{C.19}$$

Besides the Lagrangian terms, there also exist boundary equations for this system. As modelled in Figure C.1, some rather standard, similar to beam mechanics boundary conditions become.

$$u|_{x=0} = w|_{x=0} = w'|_{x=0} = 0 \tag{C.20}$$
$$w|_{x=l} = w'|_{x=l} = 0 \tag{C.21}$$
$$u|_{x=l} = u_l \tag{C.22}$$

The two boundary equations $u|_{x=0} = 0$ & $u|_{x=l} = u_l$ are particularly interesting combined with the knowledge of general beam mechanics. The membrane system at hand can in certain ways be compared to an extremely slender beam. For slender beams, it is a given that vibrations in the longitudinal direction are of much higher natural frequency than those of the transverse direction [80]. Resultingly, the longitudinal displacements $u(x,t)$ is mostly resulting from transverse motion which is determined by pretension and inertia of membrane and comb drive. This allows the strain to be rewritten into an averaged form along the membrane.

$$\varepsilon_s = u' + \frac{1}{2}w'^2 + \varepsilon_0 \longrightarrow \frac{u_l}{l} + \int_0^l \frac{w'^2}{2}\mathrm{d}x + \varepsilon_0 \tag{C.23}$$

The final three equations of motion therefore become.

$$m\ddot{u} - EA\varepsilon_s' = 0 \tag{C.24}$$
$$M\ddot{u}_l + ku_l + EA\varepsilon_s = F_{cd} \tag{C.25}$$
$$m\ddot{w} - EA(\varepsilon_s w')' = 0 \tag{C.26}$$

If now the in-plane vibrations are neglected (i.e. $\ddot{u} = 0$), which was possible because the longitudinal inertia is small, then Equation I.1 finds that $\varepsilon_s' = 0$. Which allows us to find longitudinal displacement $u(x,t)$ as such.

$$u'' = -\left[\frac{w'^2}{2} + \varepsilon_0\right]' \tag{C.27}$$

$$u' = \frac{w'^2}{2} + \varepsilon_0 + c_1 \tag{C.28}$$

$$u(x,t) = -\int_0^x \left[\frac{w'^2}{2} + \varepsilon_0\right] \mathrm{d}x + c_1 x + c_2 \tag{C.29}$$

Using the boundary conditions earlier specified in Equation C.20 ($u|_{x=0} = 0$ & $u|_{x=l} = u_l$), the integration constants can be determined as.

$$c_1 = \frac{u_l}{l} + \int_0^l \frac{w'^2}{2} \mathrm{d}x + \varepsilon_0 \tag{C.30}$$

$$c_2 = 0 \tag{C.31}$$

And as such, the EoMs have been derived and can be used to interpret the experimental data that was obtained. To arrive at these equations some simplifications have been made. The system was regarded as two-dimensional, which neglects any Poisson's related effects. Furthermore, it is assumed that longitudinal vibrations occur at much higher frequencies than transverse ones. Returning to the other two equations of motion (Equation I.2 & I.3) now allows us to investigate any nonlinear behaviour, which is done in Section I.

D

Additional results

D.1. Coupling of device and membrane

Despite the mass of the CD shuttle compared to the graphene membrane being $\frac{M}{m} \approx$ 5e5, it is possible for the graphene to drive the CD actuator into resonance. From a previous study [52], it was found using base-actuation and interferometry that the fundamental resonance frequency of the MEMS device is ≈ 80 kHz. Here, no membrane was attached to the shuttle. In this work, we demonstrate that it is possible to actuate the CD shuttle of the MEMS device by actuating merely the attached graphene. This proves the out-of-plane (oop) dynamics of the graphene are indeed coupled to the in-plane (ip) dynamics of the MEMS device. This is also theoretically confirmed in Appendix I.

Now in order to measure the ip motion of the CD, an interesting technique is employed. The interferometric setup as described in 2.3 is used. The measurement principle (in the intended scenario) is that there is a modulation of the measured laser strength due to interference that is altered by the oop movement of the 2D material membrane. Now, if the measurement laser is positioned on half of the CD and half on the cavity, the ip motion of the shuttle can cause this modulation of signal strength. Although this is not the intended method for this measurement setup, it works nevertheless. This setup is schematically depicted in Figure D.1.

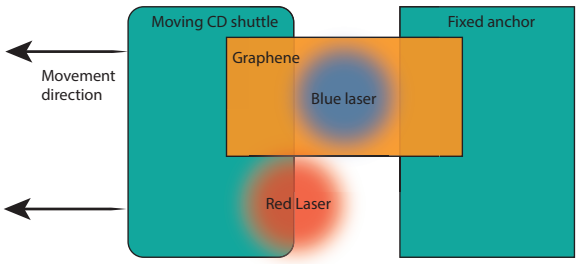

Figure D.1: Schematic setup of the alternate configuration of the measurement setup used shown in Figure 2.19. The blue laser drives the graphene membrane and the strength of the red laser is measured.

The drawback of this configuration is that as the CD moves from the voltage that is applied to it, the signal strength decays. Since this is not the intended configuration, the initial optimal signal strength is already low, but present nevertheless. The data that is obtained with this experiment is presented in Figure D.2

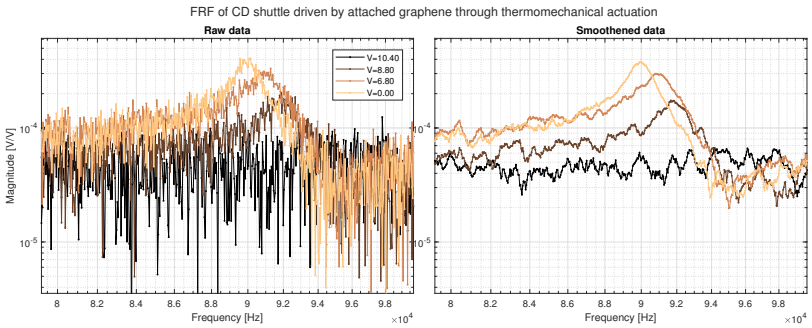

Figure D.2: FRF of the CD for distinct values of V_{mems}. Raw data and smoothened data are shown to make the behaviour more observable. Smoothing is performed according to the principle of a moving mean.

Indeed the decay as expected is visible. Along with an initial increase in resonance frequency. This is interesting because that indicates an increase in the effective stiffness of the CD actuator due to the electrostatic force that is applied. For larger V_{mems} it is hypothesised that there should be electrostatic spring softening present. This is not observed in this measurement, likely due to the decay of signal strength.

This experiment confirms that there is a coupling between the dynamics of 2D material and CD actuator, which thus should be accounted for in any theoretical formulations of membrane dynamics.

E

Sample deterioration

In response to the observed hysteresis in resonance frequency, the samples had to remain closely observed. Since the membranes are suspended and held in place purely by surface adhesive forces (Van der Waals forces which in turn facilitate frictional forces) there is nothing to rigidly prevent slippage as strain is applied. Such as depicted in for example Figure B.4. Generally, the hysteresis observed does not permanently alter the suspended membrane visibly. In a single sweep of the MEMS voltage ($V_{mems} = 0 \rightarrow 13 \rightarrow 0 \rightarrow -13 \rightarrow 0$V), there is typically a hysteresis observed. But if the positive sweep is compared to the negative sweep, they are often symmetric (As portrayed in Figure 3.6). This indicates that the repeatable hysteresis did not cause any permanent changes in the suspension/pretension in the membrane. However, in some cases, major changes in resonance frequency can be observed after certain "events". In some cases for example the flake comb drive (CD) device managed the fingers to get "pulled-in". The fact that the membranes do not rip after such an event is a strong reason to believe slippage occurs. This "pull-in" happens typically in electrostatic MEMS devices since they rely on relatively large surface areas to create the attractive force that moves the CD. Recall the formula for this electrostatic force being given in Equation 2.3.

$$F_e = \frac{nA\epsilon_0}{2(d_1 - u_l)^2} V_{mems}^2 \tag{E.1}$$

From this equation, it should be noted that the force scales quadratically with the Voltage (V_{mems}) and quadratically inverse with the gap decreasing gap size ($d_1 - u_l$). This results in an unstable equilibrium point where the fingers will snap to a stable equilibrium in the form of $d_1 - u_l = 0$. Once this "pull-in" event occurs, the Van der Waals forces keeping the moving fingers stuck to the static ones are larger than the restoring spring force. The device loses its functionality in typical scenarios. Figure E.1 illustrates this event.

To prevent this some MEMS devices have an "end-stop" implements to physically prevent this from happening. The device for this thesis unfortunately does not have such a feature. Remarkably enough, for the device of this thesis, it was discovered that the device was able to be restored after being "pulled-in" by applying some arbitrary amount of force in the out-of-plane direction using a probe station setup.

As a rule of thumb, this "pull-in" event occurs when the displacement is about $\frac{1}{3}$ of the total initial gap $d_1 = 2\,\mu$m which would be $u_{l,pi} = 0.67\,\mu$m. This can also be derived analytically without much effort but is not relevant to this thesis. To prevent this event a safety factor on the maximum voltage was implemented making the maximum achievable displacement about $u_{l,max} = 0.5\,\mu$m. In a perfect zero pre-strain membrane, this would therefore yield a maximum achievable strain of $\varepsilon_{max} = \frac{\Delta L}{L_0} = \frac{0.5\,\mu\text{m}}{6\,\mu\text{m}} = 0.0833 \approx$

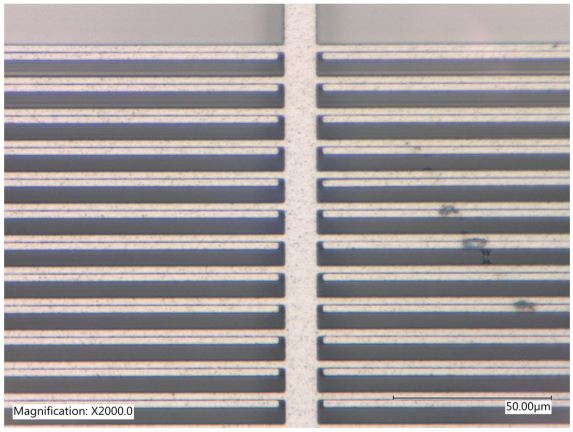

Figure E.1: Optical microscope image of a situation where the CD fingers have become "pulled-in" and remain in this state as a result of Van der Waals forces.

8%. Which is well below the maximum theoretical value for the elastic straining of graphene when nonlinearities are included in simulations [11] of 20%-26%. These high values of strain have however not been reported experimentally. Therefore the MEMS device should be well able to apply plenty of strain to the membrane to study the effects hereof on the nonlinear dynamics.

As mentioned, the membrane material sits freely on the surface and is held in place by molecular adhesive forces giving rise to frictional forces upon elongation. Despite that, slippage does occur, particularly for larger displacements ($u_l \geq 0.2\,\mu$m) or "pull-in" events. Besides the sometimes irreversible shifts in unstrained resonance frequency, the suspended membrane situation also visibly deforms as a result. The effect of the repeated experimenting on a membrane can be seen in Figure E.2

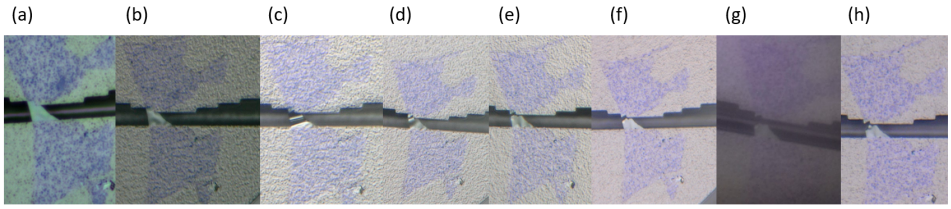

Figure E.2: Chronological array of optical microscope images recording the change in the membrane situation. (a) Shows the newly deposited MoS_2 membrane, (c) the membrane after wire-bonding the MEMS device and (g) an image of the membrane where the MEMS has "pulled-in".

It can be seen that the membrane in some scenarios tends to adhere to the sidewall of the CD/anchor. Although it also releases hereof when pulled. As long as the MEMS device has not yet "pulled in", their amount of achievable strain should remain high enough to investigate the effect of mechanical strain on such membranes. The true value of the strain however can not be determined from the displacement of the CD since there is strong reason to believe slippage is occurring.

Another event that sometimes occured is damage from bonding. The cause hereof is discussed the Chapter 4. An example of what this excessive contact pressure does to the MEMS device is illustrated in Figure E.3.

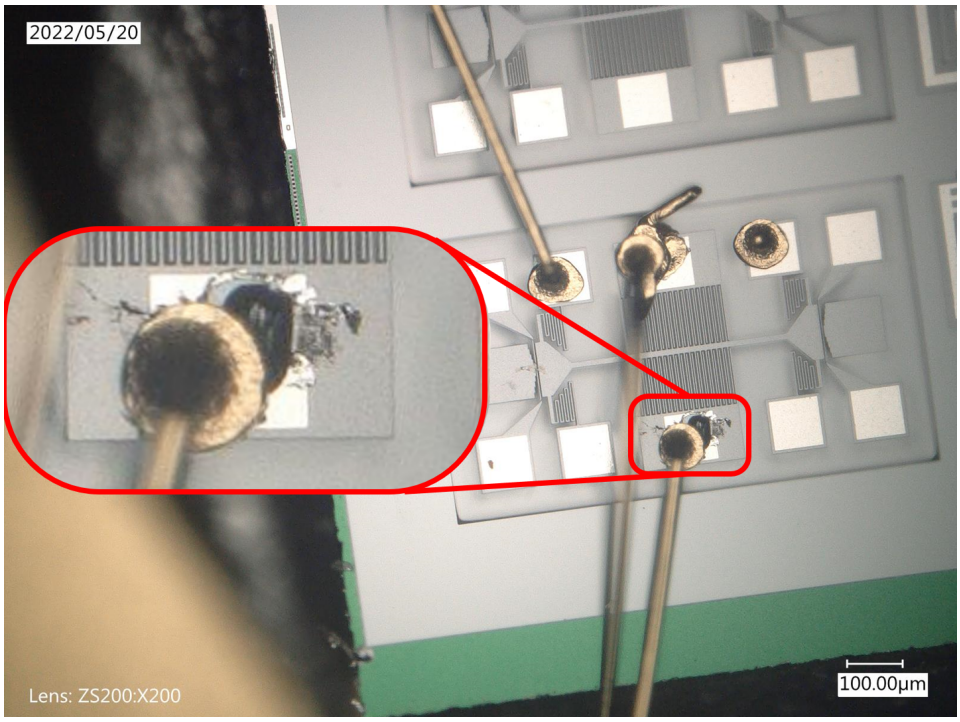

Figure E.3: Damaged bond pad showing cracking of the silicon pillar that supports it.

F

Clamping of the membrane

Clamping conditions govern the dynamics of this vibrating membrane system. Since the intention is to strain the membrane, there is a risk of slippage when certain strain values are achieved. In the measurements, this slipping is observed with high certainty. On some devices, this could be observed visually as in Figure E.2 where the surface profile had clearly been deformed. In other cases, it became apparent from the measurement data due to the consistently decreasing frequency of the fundamental resonance frequency such as depicted in Figure 3.5. Let the fundamental resonance frequency be described with $\omega_n = \sqrt{\frac{k_{eff}}{m_{eff}}}$. Assuming the effective mass stays constant, there must be a decrease in effective stiffness, i.e. pretension for membranes. The logical explanation for this is that slippage is observed.

There is work performed in literature to quantify the adhesive properties of graphene both analytically and experimentally. For multilayer graphene, it was found by pressurised blister testing that the adhesion energy is $(0.31 \pm 0.03)\,\mathrm{Jm}^{-2}$ [67, 127]. Nevertheless, irreversible hysteresis is observed so the necessity for clamping is present. In previous works, this has been performed using various techniques. One is to integrate graphene a layer of PMMA in the (photo-)lithographic production steps of the MEMS device [42, 44]. Another method is by applying micro epoxy droplets on either side of the membrane [85, 86]. Although suspicion is raised here since the reported values of experimentally achieved strain are much greater than presented in other works. A possible explanation could be that the epoxy creeps onto the membrane while it sets. Or finally, the clamping can also be left out, as is done in [11]. If the SiO_2 surface is extremely flat, and the flake sufficiently large, the Van der Waals forces are strong enough to support the straining of the membrane until fracture. Unfortunately, experiments have shown that this is not the case for this project. There are two arguments why.

1. The surface area of the membrane(s) on the anchor sides is insufficiently large.
2. The roughness of the SiO_2 is too great for the graphene to properly conform to the surface which greatly reduces the Van der Waals interactions.

In this work, we tried something new. The idea was to print onto the MEMS device using two-photon polymerization (2PP/TPP). This process allows to 3D-print structures onto the MEMS device at the required resolution. A photoresist is deposited onto the device which is polymerized using a focused laser beam. Only within the focal spot of the laser, the density of photons is high enough such that the threshold is reached to polymerize the photoresist. This allows for printing at nanoscale resolution [49]. A schematic for this process is depicted in Figure F.1.

What becomes apparent from Figure F.2, are both negative and positive things. Here it was attempted to print on the MEMS device. As can be seen, there are printed cubes on

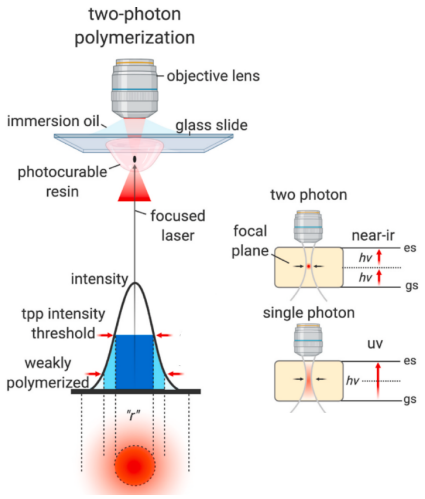

Figure F.1: Schematic illustration of the lithographic TPP process. Image adapted from [50].

the device, which indicates that good sticktion to the substrate is possible. Although it was a tricky task since the machine used (Nanoscribe Photonic Professional GT2) had problems finding the interface of the material which is important since the focus spot of the laser is so small. With high certainty, this is a result of the surface roughness of the device as mentioned by the manufacturer of the machine. The interface is found by detecting an interference of the reflected light when the object is near the focal distance. This problem however can be manually mitigated if some test prints are made around the focal distance.

The biggest problems arise from the viscous forces involved in this process. The sample is dipped in a viscous resin, whose residue has to be dissolved away after polymerization. This produces viscous forces along the membrane sample which might cause it to move (remains to be tested). Furthermore, during the evaporation of the liquid used for the last processing step (Isopropyl alcohol/Novec HFE 7500 3M™) the surface tension of the liquid causes the electrostatic comb fingers to get pulled into each other. In the case where the flake is clamped, this would likely cause a fracture since this corresponds to 33% strain. To circumvent this, a process called critical point drying (CPD) could be used. Here a liquid is evaporated at its critical point such that there is no surface tension. This however remains to be tested.

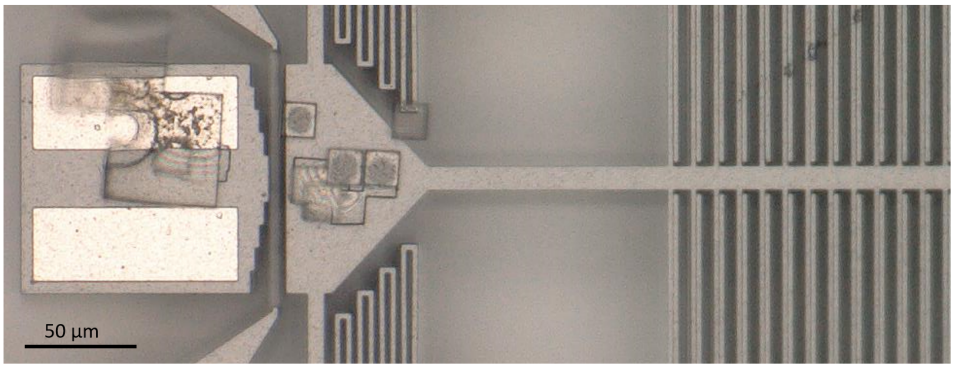

Figure F.2: Optical microscope image of the MEMS device after attempting to print clamps using 2PP technology

Another method that is simple in essence is to "glue" the edges of the membrane to the device [86, 122]. Using a very accurate micropipette or hollow AFM cantilever, one can deposit an adhesive. An example of such an alternative clamping method can be found

in Figure F.3. This method is probably less likely to do damage to the membrane and device as there is only very local contact with the deposits.

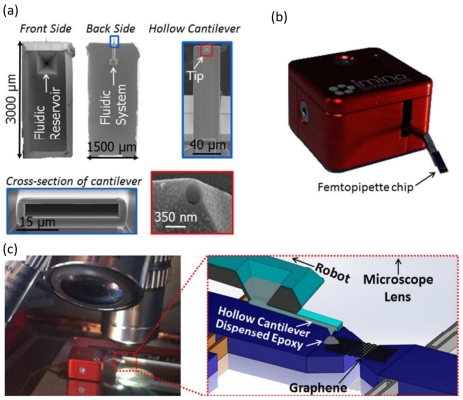

Figure F.3: Epoxy deposition technique adapted from [86]. (a) Images showing a Femtopipette with a hollow AFM cantilever with a nozzle at the tip through which adhesive can be dispensed. (b) A 4 DOF robot to accurately align the nozzle on the device. (c) an optical microscope to keep visual control.

Yet another method that could be used is Electron Beam Induced Deposition (EBID). This has been used in literature before to clamp graphene in place [71]. EBID can be used to deposit a wide range of materials, including metals, semiconductors, and insulators. The main challenge to overcome when performing EBID clamping is the potential difference that inevitably occurs when working with an electron beam. When electrons hit the sample, there is a potential difference created between the static and dynamic parts of the CD. This causes the shuttle to move which is disastrous for the 2D material sample as it will lead to slipping, or even fracture. This problem can be addressed by creating a short circuit across the comb. This can be done in many ways but should be reversible since the device will need to be loaded with a controllable potential to apply mechanical tension. This charging problem will therefore also occur in related techniques such as Scanning Electron Microscopy (SEM), Transmission Electron Microscopy (TEM) and Focussed Ion Beam (FIB).

G

Numerical modeshapes

The modeshapes that the membrane would exhibit can be numerically investigated using a software package such as Comsol. This is done to compare the obtained modeshape images to perhaps conclude something about the membrane parameters which are adjustable in the numerical computations. Such parameters include the direction(s) and magnitude of the pre-strain (or pretension which are directly correlated), and the Young's modulus. It is hypothesised that the pretension in the membrane sample as depicted in Figure 3.2, is mainly along the direction of the supporting edges. This is because the pretension is hypothesised to originate from van der Waals forces between the membrane and the sidewalls. Especially in the case where the membrane is strained, the tension shall be dominant in this direction. In the following figures, this direction corresponds to the y axis unlike other analyses performed in this thesis. It should be noted that pretension in both planar (x&y) directions are coupled through the Poissons ratio. So it is expected to obtain modes that break symmetry in both directions.

G.1. Model

Using Comsol software, a membrane model was built to resemble as much as possible the situation of the graphene sample at hand. With a longitudinal length (clamp to clamp) of 6 μm and a width (free edge to free edge) of 20 μm. The respective constraints are applied and summarised below.

1. On the supporting edge two different constraints are applied. One side is fixed, and the other side is subjected to a prescribed load/inertia equal to the mass of the CD actuator (9.0045e−10 kg).

2. Within the membrane there is are the material paramters E,ρ,ν,ε_0. Which are the Young's modulus, mass density, Poisson ratio and pre-strain respectively. The numerical values for $E = 750$ GPa, $\rho = 2267 kg/m^3$ and $\nu = 0.16$ are obtained from literature [**cao2018**] and are assumed to apply for this model. ε_0 Was obtained from experiments, which also requires other assumptions to be made, see Appendix H.

These are the basic geometric and physical constraints to model the resonating membrane. It should be noted that other constraints/effects can be modelled. Examples of this include: straining the membrane, gravity, adding wrinkles and initial deformations. But for now, these effects shall remain ignored. The effect of a thermal gradient, leading to inhomogeneous stresses is neglected. The thermal conductivity should be great enough that the spreading of the local heat applied from the optothermal actuation spreads at much faster rates than the eigenfrequencies [74].

G.2. Results

For the basic case with pre-strain only in the longitudinal direction (clamp-clamp) and the constraints as summarised above, the modeshapes can be obtained. They are depicted in Figure G.1.

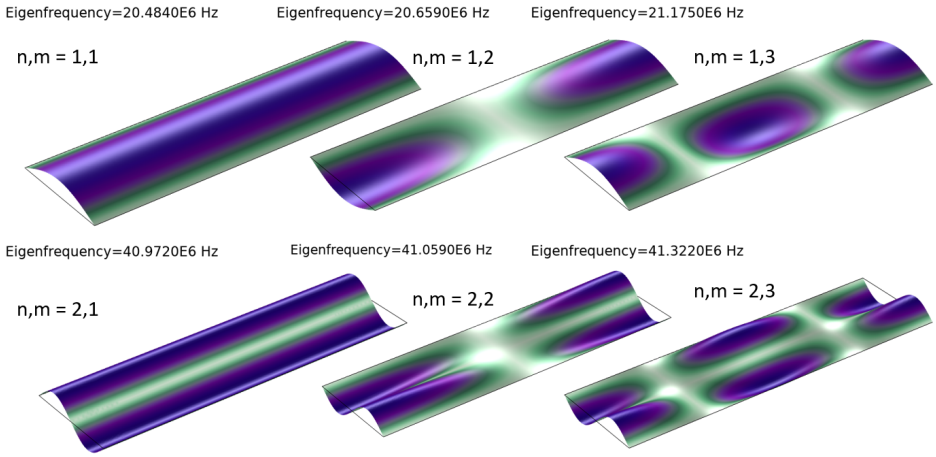

Figure G.1: Grid of modeshapes calculated using Comsol. The grid shows clear separation between modes in two directions labelled as "n"&"m"

There are a couple of things to take away from these simulations, which are summarised below.

1. The fundamental modeshape (n,m = 1,1) shows a simple doubly clamped membrane moving up and down as a whole.
2. The second mode tells us that the interference signal strength will be stronger around the free edges of the membrane and very weak in the middle. This is in fact confirmed in measurements.
3. The frequencies of the modes are much higher than those found in experiments, which indicates that in the experimental scenario, either the effective- stiffness and mass are respectively lower and higher than that in the simulation. Possible explanations are;

   The used E and ε_0 are not the same as in the experimental setup.

   The model does not describe the correct morphological scenario. In reality, there are wrinkles, ripples and sag as well as sidewall adhesion and possible contaminations.
4. The n&m directions of the modeshapes are caused by coupling from the pretension in longitudinal (clamp-clamp) direction into the transverse (free-free) direction through the Poisson's ratio.

H

Fitting the initial hardening response

H.1. Additional tensioning of the membrane

As has become apparent from Figure 3.6, there is an initial response where the resonance frequency increases quadratically (shown by fitting an arbitrary quadratic curve in Figure 3.6 (b)). This makes sense if one would assume that the effective mass is a constant, and the effective stiffness is solely dependent on the pre-strain of the doubly-clamped membrane. These are fairly common assumptions since membrane theory suggests neglecting the bending rigidity [51, 78]. Therefore, if the membrane would be strained its effective stiffness (K_{eff}) would increase linearly with the force applied to the membrane. For small deflections of the MEMS device, the exerted force scales with the square of the voltage applied (V_{mems}). This comes down to $k_{eff} \propto F_{strain} \propto V_{mems}^2$. The force that is applied to the membrane, can be calculated from the static equation that equilibrates the electrostatic force to that in the beam flexures and the membrane. Let n be the number of CD actuator fingers, A_{mems}&A_{gr} be the area of the parallel plate MEMS and the cross-sectional surface of the membrane respectively. d_1&d_2 Are the initial gap sizes of the CD actuator (see Figure 2.2), x_L the displacement of the shuttle. ϵ_0 is the permittivity of vacuum. E is the Young's modulus of graphene which is assumed to be 750 GPa. This value corresponds to the theoretical strength of graphene, with a correction factor to compensate for any imperfections. Whether or not it is a good assumptions will become clear later in the process.

$$F = kx \tag{H.1}$$

$$F_{el} = (k_{mems} + \frac{EA_{gr}}{L})x_L \tag{H.2}$$

$$\left(\frac{nA_{mems}\epsilon_0}{2(d_1 - x_L)^2} - \frac{nA_{mems}\epsilon_0}{2(d_2 + x_L)^2}\right)V^2 = (k_{mems} + \frac{EA_{gr}}{L})x_L \tag{H.3}$$

Since the force in the membrane is directly related to the displacement of the shuttle (x_L), an expression in the form of $x_L(V)$ is required. Unfortunately, this is not analytically possible. What is however possible is to obtain an expression in the form of ($V(x_L)$).

$$V(x_L) = \pm\frac{2^{\frac{1}{2}}(d_2 + x_L)^2(d_1 - x_L)^2(\frac{(A_{mems}\epsilon_0 n x_L(d_1+d_2)(k_{mems}L + A_{gr}E)(d_2 - d_1 + 2x_L))}{(L(d_2+x_L)^2(d_1-x_L)^2)})^{\frac{1}{2}}}{A_{mems}\epsilon_0 n(-d_1^2 + 2x_L d_1 + d_2^2 + 2x_L d_2)} \tag{H.4}$$

This expression can then be plotted, and transposed by 90 deg to obtain the graph that describes $x_L(V)$. Since there is no exact function to describe $x_L(V)$, this graph is fitted within the quadratic regime with a polynomial. This is illustrated in Figure H.1. The idea is that a fit is made of a full tenth-order polynomial which is then reduced to one where only even powers play a role and the constant term is set to zero (corrected polynomial). This is because the expected behaviour is symmetric around $V = 0$ and quadratic in nature.

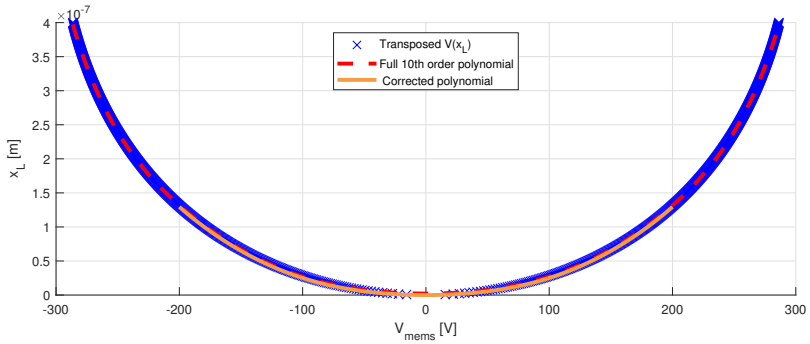

Figure H.1: Polynomial fit of transposed data describing $V(x_L)$ to obtain $x_L(V)$ numerically. Value used for Young's modulus $E = 750\,\text{GPa}$.

This describes what the relationship between the CD shuttle displacement (x_L) and the voltage on the CD actuator ($V_{mems} = V$) is, and is described with a polynomial. It is now possible to define a model that should explain the quadratic increase in resonance frequency $f_n(V^2)$ where the only unknown is the fit parameter of interest.

H.2. Effective mass

In order to find the effective mass from the increase in resonance frequency from straining, we start a the beginning. Let there be given the standard expression for the resonance frequency.

$$f_n = \frac{1}{2\pi}\sqrt{\frac{k_{eff}}{m_{eff}}} \tag{H.5}$$

From the literature, a formulation of this effective stiffness in out-of-plane (OOP) direction was found that describes the situation at hand; a doubly clamped rectangular membrane subjected to variable tension [15, 38, 11]. In this work, the effective stiffness is given as such.

$$k_{eff} = \frac{30.78 W t^3}{L^3} E + \frac{12.32}{L} T \tag{H.6}$$

Where $W, t \& L$ are the width, thickness and length of the membrane. E is the Young's modulus and T the tension in the membrane. Such that T can be subdivided into two types, pretension (T_0), and added tension from straining (T_e).

$$T = T_0 + T_e \tag{H.7}$$

This formula for describing the effective stiffness contains as can be seen two terms. These terms follow from both bending rigidity (plates) and IP tension (membranes). If a high value for the Young's modulus is assumed ($E = 750\,\text{GPa}$), a typical value for pretension ($T_0 = 20\,\mu\text{N}$ [15]) as well as a certain thickness of the membrane (20 layers $= 7\,\text{nm}$). It can be found that in unstrained configuration.

$$k_{eff} = k_{plate} + k_{membrane} \tag{H.8}$$

$$k_{plate} = \frac{30.78 W t^3}{L^3} E = 0.7332\,\mathrm{Nm}^{-1} \tag{H.9}$$

$$k_{membrane} = \frac{12.32}{L} T = 40.07\,\mathrm{Nm}^{-1} \tag{H.10}$$

From this, it can be concluded that the plate-mechanics contribution can be neglected compared to that of the membrane. For a smaller Young's modulus (which is expected in reality due to the hidden area [82]), or when strain is applied, this difference only grows.

Similarly, the effective stiffness can now be subdivided into two types.

$$k_{eff} = k_0 + k_e \tag{H.11}$$

$$k_0 = \cancel{\frac{30.78 W t^3}{L^3} E} + \frac{12.32}{L} T_0 \tag{H.12}$$

$$k_e = \frac{12.32}{L} T_e \tag{H.13}$$

Now recall that a polynomial expression for $x_L(V)$ was obtained assuming a certain Youngs modulus E. That expression can be used to describe the added tension in the membrane simply by using the mechanics of a beam/plate/membrane under tensile load.

$$T_e = \frac{E A_{gr}}{L} x_L \tag{H.14}$$

Where A_{gr} represents the cross-sectional area of the membrane. This all comes together to describe the resonance frequency as such.

$$f_n = \frac{1}{2\pi} \sqrt{\frac{\frac{12.32}{L}(T_0 + \frac{E A_{gr}}{L} x_L)}{m_{eff}}} \tag{H.15}$$

This equation has however two unknowns in it the effective mass and the pretension (and the Young's modulus but this one was assumed to be 750 GPa). It is possible to fit this formula to the quadratic region of the obtained data (Figure 3.6 (b)). However, having two fit parameters makes fitting a tricky process to automate. Although not impossible with proper conditioning of the minimization algorithm, there is a better way to address the issue. Let be known the initial resonance frequency that is where no strain is applied ($T_e = 0$).

$$f_{n,0} = \frac{1}{2\pi} \sqrt{\frac{k_0}{m_e f f}} \tag{H.16}$$

Which can be rewritten to obtain k_0 as.

$$k_0 = m_{eff} 4\pi^2 f_{n,0}^2 \tag{H.17}$$

Now substituting this back into the full expression H.15 gives.

$$f_n = \frac{1}{2\pi}\sqrt{\frac{m_{eff}4\pi^2 f_{n,0}^2 + \frac{EA_{gr}}{L}x_L}{m_{eff}}} \tag{H.18}$$

Since $f_{n,0}$ is a known data point, the resulting equation now has only one fit parameter, the effective mass. Which is now easily obtained.

H.3. Pretension

Obtaining now the second initially unknown parameter, the pretension, is surprisingly uncomplicated. Since the effective mass is now known, Equation H.15 can be reevaluated such that the only unknown is the pretension.

H.4. Results

Now performing the procedures as described. The data that was used here is the same dataset as depicted in Figure 3.6 within the regime that shows quadratic behaviour (±5V). Yields the parameters as presented in Figure H.2.

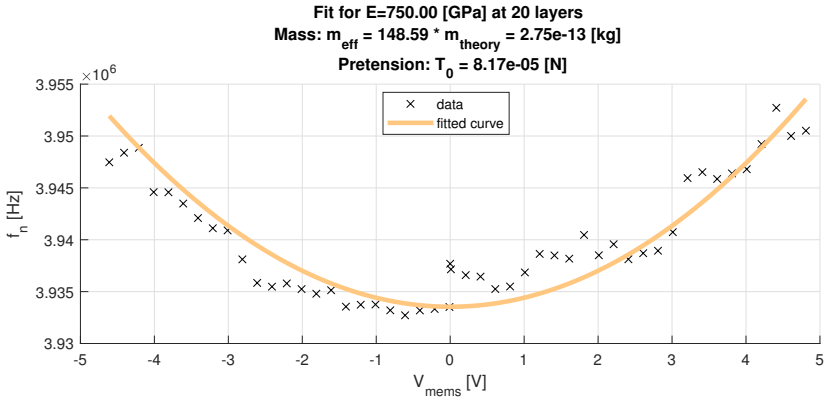

Figure H.2: Result of described fitting procedure on dataset depicted in Figure 3.6 (b) on the quadratic region.

Now if instead a larger region of data is used, the results change greatly. Such is illustrated in Figure H.3.

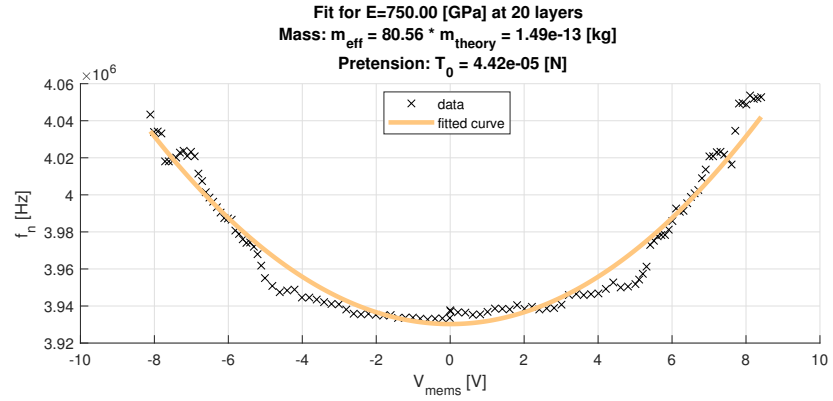

Figure H.3: Result of described fitting procedure on dataset depicted in Figure 3.6 (b) on the quadratic and linear regions.

Interestingly enough, the obtained parameters differ quite largely from one another. Despite that, the main observation that is taken from this is that the effective mass is very large. For a regular (fully clamped rectangular) membrane, its effective mass is only $\frac{1}{4}m_{theory}$ where m_{theory} is the actual mass of the membrane. For simplicity, that

is roughly a factor of 400 difference with the values obtained here. It should be noted however that for the theoretical mass of the membrane, it has been assumed that the membrane is 20 layers of thickness. This assumption has yet to be checked by AFM measurements

Now the assumptions of the Young's modulus are revisited and criticised. Let us assume that the value to be obtained for the effective mass, should be approximately the theoretical mass of the membrane. With that in mind, the Young's modulus can be used as a fitting parameter. It is known that the wrinkles, ripples and sagginess of the membrane have an enormous impact on the observed Young's modulus [10, 82, 30], especially the latter would cause issues in this low-strain region of ± 6V. The sagging and wrinkling have to be overcome fully before any strain shall occur. This is confirmed by putting more weight on the correctness of the fit in the region of larger voltage. To obtain a better fit there, a higher Young's modulus is found compared to the lowly strained area. The results are presented in Figure H.4.

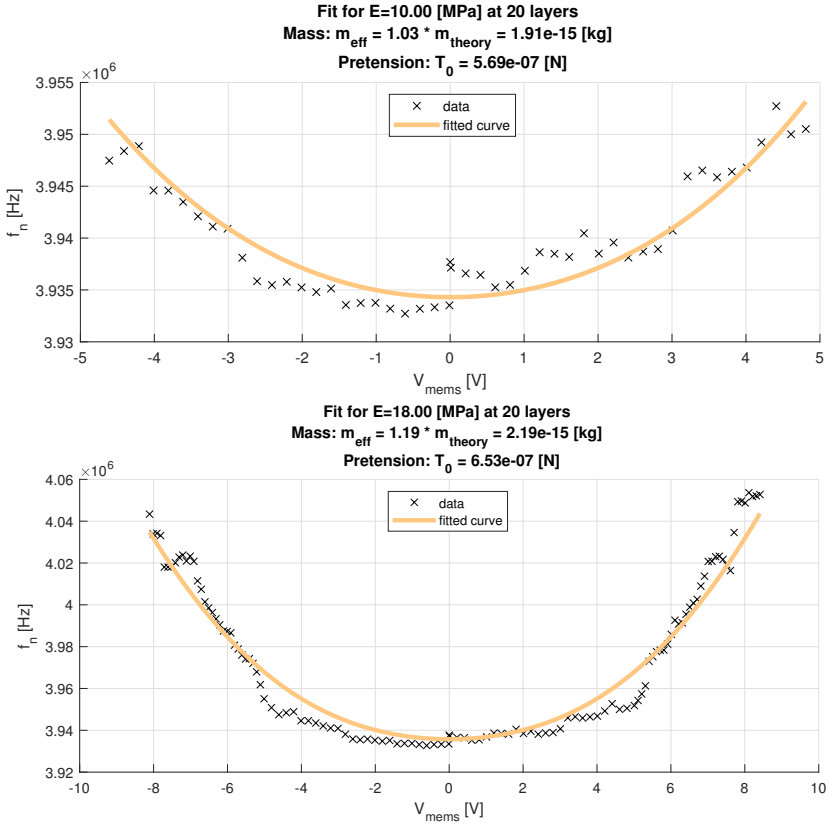

Figure H.4: Results of fitting the Young's modulus to the increase in resonance frequency under the condition that the effective mass shall be approximately the theoretical mass.

Investigating the EoM

With a model that schematically represents the situation of the system that strains the membrane, it was possible to derive three equations of motion (EoM). This was performed in Appendix C. They respectively represent the in-plane (IP - u) movement of the membrane, the IP movement of the shuttle (u_l) and the out-of-plane (OOP - w) movement of the membrane along its longitudinal direction.

$$m\ddot{u} - EA\varepsilon_s' = 0 \tag{I.1}$$
$$M\ddot{u}_l + ku_l + EA\varepsilon_s = F_{cd} \tag{I.2}$$
$$m\ddot{w} - EA(\varepsilon_s w')' = 0 \tag{I.3}$$

In this equation, E and A are the Young's modulus and the cross-sectional area of the graphene. k is the IP stiffness of the MEMS actuator in the longitudinal direction (see Section 2.1.1). $F_{CD}(u_l, V)$ is the electrostatic force that strains the membrane and is dependent on the displacement u_l and the applied voltage V. m and M represent respectively the mass of the membrane and the mass of the shuttle. For the sample as presented in Figure 3.7, these values are (again assuming 20 layers thick graphene).

$$m = lWt\rho_{gr} = 6\text{e}{-6}\ 20\text{e}{-6}\ 7\text{e}{-9}\ 2267 = 1.9043\text{e}{-15}\,\text{kg} \tag{I.4}$$
$$M = V_{CD}\,\rho_{\text{Si}^+} = 3.8646\text{e}{-15}\ 2328 = 8.997\text{e}{-10}\,\text{kg} \tag{I.5}$$

The final expression in the EoM is the strain term ε_s. This is described by the sum of three strains. The actual longitudinal strain caused by the MEMS actuator (u'), the strain caused by OOP deflection (w') and a pre-strain term (ε_0) which is important in membrane mechanics since there is (almost) no bending stiffness. If these components are averaged along the longitudinal direction of the membrane we obtain.

$$\varepsilon_s = u' + \frac{1}{2}w'^2 + \varepsilon_0 \longrightarrow \frac{u_l}{l} + \int_0^l \frac{w'^2}{2l}\mathrm{d}x + \varepsilon_0 \tag{I.6}$$

Now the purpose of this appendix is to simulate the behaviour that is observed by separating the motion in static and dynamic scenarios. This will be done by separating the DoF of the system into static and dynamic components.

$$u(x,t) = u_s(x) + u_d(x,t) \tag{I.7}$$
$$u_l(x=l,t) = u_{l,s} + u_{l,d}(t) \tag{I.8}$$
$$w(x,t) = w_s(x) + w_d(x,t) \tag{I.9}$$

Besides that, this separation subsequently also alters the strain formulation to the following.

$$\varepsilon_s = \varepsilon_0 + \frac{u_{l,s} + u_{l,d}(t)}{l} + \int_0^l \frac{(w_s(x) + w_d(x,t))'^2}{2l} \mathrm{d}x \tag{I.10}$$
$$= \varepsilon_0 + \frac{u_{l,s} + u_{l,d}(t)}{l} + \int_0^l \frac{w_s'^2(x) + \cancel{w_d'^2(x,t)} + 2w_s'(x)w_d'(x,t)}{2l} dx \tag{I.11}$$

Now the term $w_d'^2(x,t)$ will be ignored as it is nonlinear and its contribution shall be small compared to the static and linear dynamic deflection.

I.1. Static analysis

In the scenario where the membrane is not being actuated, it is subjected to random Brownian motion. This can give rise to small deflections, especially that of the mode-shapes [25]. For simplicity, the membrane is assumed to be completely stationary. In this case, all time-derivative components of the EoM become zero such that.

$$\cancel{m\ddot{u}} - EA\varepsilon_s' = 0 \tag{I.12}$$
$$\cancel{M\ddot{u}_l} + ku_{l,s} + EA\varepsilon_s = F_{cd} \tag{I.13}$$
$$\cancel{m\ddot{w}} - EA(\varepsilon_s w_s')' = 0 \tag{I.14}$$

From I.12 can quickly be deduced that the variation of the strain $\varepsilon_s' = 0$.

I.2. Dynamic analysis

Expanding on the static behaviour is the dynamic behaviour. Neglecting therefore the time derivative components of the static deflections yields the following EoM. For simplicity's sake, the indicator of position and time (x,t) will be left out.

$$m\ddot{u}_d - EA\varepsilon_s' = 0 \tag{I.15}$$
$$M\ddot{u}_{l,d} + k\left[u_{l,s} + u_{l,d}\right]u_{l,s} + EA\varepsilon_s = F_{cd}(V, u_s, u_d) \tag{I.16}$$
$$m\ddot{w}_d - EA(\varepsilon_s(w_s' + w_d'))' = 0 \tag{I.17}$$

especially the second and third EoM here are of interest. The Forcing term F_{cd} can be Taylor expanded to obtain.

$$F_{cd}(V, u_s, u_d) \approx F_{cd}(u_{l,s}) + \frac{\partial F_{cd}}{\partial u_{l,s}} u_{l,d} \tag{I.18}$$

If now the expanded strain formulation is applied to these two dynamic EoM, a coupling between equations becomes apparent.

$$M\ddot{u}_{l,d} + k\left[u_{l,s} + u_{l,d}\right] + EA\left[\varepsilon_0 + \frac{u_{l,s} + u_{l,d}(t)}{l} + \int_0^l \frac{w_s'^2(x) + 2w_s'(x)\, w_d'(x,t)}{2l} dx\right] = F_{cd}(V, u_s, u_d) \tag{I.19}$$

$$\begin{aligned} &m\ddot{w}_d - EA(\varepsilon_s(w_s' + w_d'))' = 0 \\ &= m\ddot{w}_d - EA\left(\left[\varepsilon_0 + \frac{u_{l,s} + u_{l,d}(t)}{l} + \int_0^l \frac{w_s'^2(x) + 2w_s'(x)w_d'(x,t)}{2l} dx\right](w_s' + w_d')\right)' \end{aligned} \tag{I.20}$$

From this, it becomes apparent that the dynamic ip & oop dynamics are coupled under the assumption that there are ever-so-slight deformations in the membrane which would mean that $w_s' \neq 0$.

J

Analysis of slippage and sidewall adhesion

From an observed declining initial resonance frequency ($\omega_n|_{V=0}$) of the main graphene sample, an important question arose. For this one specific sample, the resonance frequency has dropped by approximately 50% between the very first and final measurements. One explanation could be a sudden increase in the effective mass due to contamination of any kind that could have occurred whilst loading the device in and out of the interferometric measurement setup. Unfortunately, this is something which can not be checked visually. In addition, the decline of $\omega_n|_{V=0}$ is observed after each voltage sweep, therefore, this assumption is ruled out.

That being so, means that a major decrease occurred in the effective stiffness of the membrane, which is predominantly governed by the pretension. Therefore there are two pathways open to analyse this. One is that this decrease can be attributed to irreversible slippage of the membrane which would cause an elongation of the membrane across the gap. The other possibility is that this decrease could come from a peeling of the sidewall which would also decrease the pretension [8, 22, 56, 66, 74, 119].

Another possibility, that is however not analysed quantitatively, is that there is sag that has led to buckling. This can be comprehended by imaging the membrane slipping when tensioned, and then making an ever-so-slight fold/buckle when tension is released. This can drastically impact $\omega_n|_{V=0}$ but is too complicated to estimate analytically. It adds however another pathway to explain the behaviour that is observed.

J.1. Slippage analysis

If the assumption is made that the effective mass (m_{eff}) of the membrane is constant between experiments, then the decrease in resonance frequency can be attributed to a change in effective stiffness (k_{eff}). To extract the effective mass, a number of assumptions were made such as the Young's modulus (E) and sample thickness (t). This is described in Appendix H. The obtained effective mass is a point of discussion in itself which is relevant to this analysis.

The idea is that this decrease in pretension would find its origin in hysteresis caused by irreversible slippage. If that would be so, this slippage can be found by attributing the tension drop to an axial elongation of the membrane. The axial stiffness of a membrane is simply given by.

$$k_g = EA/l_0 \tag{J.1}$$

Where E is the Young's modulus, $A = wt$ is the cross-sectional area and l_0 is the unstrained length which is $6\,\mu$m. Now in order to find the decrease in stiffness, the fundamental resonance frequencies before ($\omega_{n,0}$) and after ($\omega_{n,1}$) straining are compared. This gives that.

$$\Delta F_n = \frac{1}{2\pi}\sqrt{\frac{\Delta k_{eff}}{m_{eff}}} \tag{J.2}$$

$$\omega_{n,1} - \omega_{n,0} = \sqrt{\frac{\Delta k_{eff}}{m_{eff}}} \tag{J.3}$$

$$\Delta k_{eff} = (\omega_{n,1} - \omega_{n,0})^2 m_{eff} \tag{J.4}$$

Note that the unit of effective stiffness is in N/m per unit membrane width. Therefore the change in tension is equal to.

$$\Delta T = \Delta k_{eff} w \ \text{[N]} \tag{J.5}$$

If this axial stiffness of graphene (k_g) is used to describe this change can be found using.

$$\Delta L = \Delta T \frac{l_0}{EA} \tag{J.6}$$

If this result is plotted for many measurements it can be seen how this model can translate an elongation of the membrane. Note that to do so, these two assumptions are important. The Young's modulus and the effective mass. Because of this, the result of this analysis is but an indication of the feasibility of the parameters. Let be assumed now a relatively high E and a high m_{eff} which was obtained according to this E.

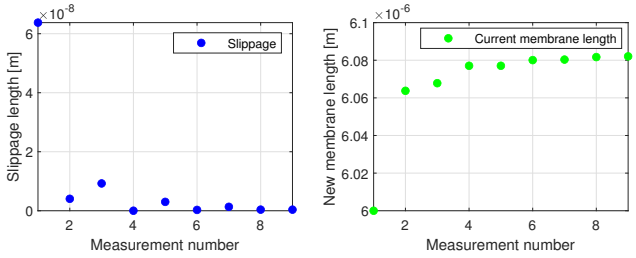

Figure J.1: Progression of membrane length after repetitions of straining for $E = 750\,$GPa and $m_{eff} = 100 m_{theory}$ assuming 20 layer of thickness.

From the fitting of the hardening response, it was found that for extraordinarily low $E = 15\,$MPa $\Longrightarrow m_{eff} \approx m_{theory}$. The results of the slippage values are naturally much larger in this scenario. First of all, the pretension drop would be a factor $\sqrt{100}$ smaller. But due to the much lower E, the elongation increases to compensate for the drop in pretension.

J.2. Sidewall adhesion

Another factor that contributes to the pretension in the membrane, is the van der Waals forces between the membrane and the sides of the trench over which it is suspended. From intuition, it is these forces that could very well be responsible for the repeatable hysteresis loop as presented in Figure 3.6. Upon tensioning ($V_{mems} = 0 \longrightarrow 13\,$V), the membrane is stuck to the sidewall, and peels loose, the overall pretension, and thus resonance frequency is higher. Upon relaxation ($V_{mems} = 13 \longrightarrow 0\,$V), the membrane is still peeled from these walls until the induced sag allows this stickage to occur. Hence, the pretesion is overall smaller and the resonance frequency lower. Also upon relaxation, there are repeatable points, where a sudden sidewall adhesion surge seems to

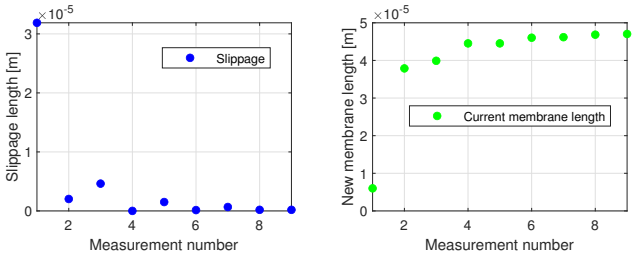

Figure J.2: Progression of membrane length after repetitions of straining for $E = 15\,\text{MPa}$ and $m_{eff} \approx m_{theory}$ assuming 20 layer of thickness.

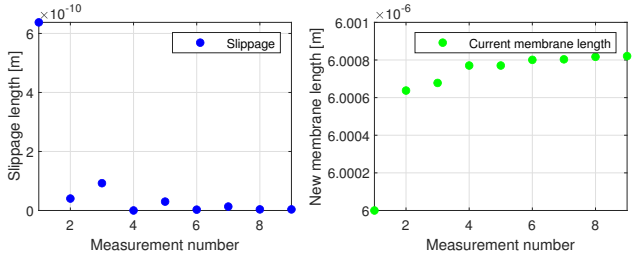

Figure J.3: Progression of membrane length after repetitions of straining for $E = 750\,\text{MPa}$ and $m_{eff} \approx m_{theory}$ assuming 20 layer of thickness.

occur, which intuitively makes sense. This effect of sidewall adhesion is presented in the literature before [10]. And such hysteresis loops are also observed and analysed recently [124].

The van der Waals interaction (per unit area) between two surfaces can typically be described using the Hamaker constant and is given by [56].

$$W = \frac{A}{12\pi D^2} \tag{J.7}$$

Where A is the Hamaker constant between the two surfaces, and D is the distance between the two surfaces. Now if rather the total force is required, it is related to the van der Waals interaction as such.

$$F_{\text{adhesion}} = -\frac{\partial W}{\partial D} = \frac{-A}{6\pi D^3} \tag{J.8}$$

Now in the specific scenario at hand, where the membrane perceives a tensile force at the edge of the adhered area (that goes down into the trench), the force required to peel it loose shall intuitively be smaller than the total adhesive force. This force required to peel the membrane (per unit area) is related to the adhesion force as such.

$$F_{\text{peel}} = F_{\text{adhesion}} \frac{D}{2d} \tag{J.9}$$

Where d now represents the in-plane length, typically much larger than the interlayer distance D. It is this mechanism that makes the exfoliation of 2D materials possible [119, 22]. The Hamaker constant A between SiO_2 and graphene was found to be $A_{gr-SiO_2} = 1.350\text{e}{-19}\,\text{J}$ [66]. Where the thickness of the membrane plays a significant role, but quickly saturates towards the value of bulk graphite around 10 layers ($\approx 3.5\,\text{nm}$). Using these values and equations, it was found that sidewall adhesion alone can not be responsible for the total drop in pretension throughout the measurements. As this would require the depth to be unreasonably large. It is however an effect that intuitively and logically is present in the sample of this thesis.

K

Nonlinear stiffness analysis

In the experiments where the actuation power was great enough to drive the membrane into the nonlinear domain, interesting behaviours were observed. The main observation is depicted in Figure 3.8. As the straining voltage (V_{mems}) is increased, a sequential hardening to softening to hardening is observed. To explain this behaviour, the EoM are consulted yet again, for the sake of analysis, slippage and pre-deformation are discarded. Recall from Appendix C the schematic layout of the system and the dynamical EoM for the 3 DoF of the system being.

$$m\ddot{u} - EA\varepsilon_s' = 0 \tag{K.1}$$

$$M\ddot{u}_l + ku_l + EA\varepsilon_s = F_{cd} \tag{K.2}$$

$$m\ddot{w} - EA(\varepsilon_s w')' = 0 \tag{K.3}$$

Where the strain consists of three main components. The pre-strain, the in-plane (ip) deflection and out-of-plane (oop) deformation.

$$\varepsilon_s = u' + \frac{1}{2}w'^2 + \varepsilon_0 \longrightarrow \frac{u_l}{l} + \int_0^l \frac{w'^2}{2l}\mathrm{d}x + \varepsilon_0 \tag{K.4}$$

And the electrostatic force which is described by.

$$F_{cd}(V,u_l)\hat{\boldsymbol{i}} = \left(\frac{nA\epsilon_0}{2(d_1-u_l)^2} - \frac{nA\epsilon_0}{2(d_2+u_l)^2}\right)V^2 = \frac{nA\epsilon_0(d_2^2+2u_l(d_1+d_2)-d_1^2)}{2(d1-u_l)^2(d_2+u_l)^2}V^2 \tag{K.5}$$

From observations, there must apparently be nonlinear softening and hardening terms in the oop stiffness. Since the oop response is measured, and the ip stiffness is modulated there must be a coupling to this modulation voltage $V_{mems} = V$. In order to investigate this coupling and find a formulation for the nonlinear stiffness, the following can be performed.

1. Assume a modeshape shape $w_m(x)$ and amplitude $q(t)$.
2. Perform something on the forcing term F_{cd} such that u_l can be isolated from the ip EoM
3. Substitute the ip EoM into the oop EoM
4. Solve the linear and cubic stiffness terms that express the introduced deflection $q(t)$

For the first step, the modeshape ($\phi(x,t)$) that can be chosen is done such that the integral over the length squared is equal to 1. This is a commonly assumed modeshape for a doubly clamped slender beam [114].

$$w(x,t) \longrightarrow \sqrt{\frac{2}{3l}}(1-cos\left(\frac{2\pi}{l}x\right))q(t) = \phi(x,t) \tag{K.6}$$

$$w'(x,t) = \frac{2\pi}{l}\sqrt{\frac{2}{3l}}sin\left(\frac{2\pi}{l}x\right)q(t) \tag{K.7}$$

$$w''(x,t) = \frac{4\pi^2}{l^2}\sqrt{\frac{2}{3l}}cos\left(\frac{2\pi}{l}x\right)q(t) \tag{K.8}$$

Now this allows the reformation of the strain expression into the following

$$\frac{u_l}{l} + \int_0^l \frac{w'^2}{2l}\mathrm{d}x + \varepsilon_0 \longrightarrow \frac{u_l}{l} + \frac{2\pi^2}{3l^3}q^2 + \varepsilon_0 \tag{K.9}$$

The next problem to be addressed is that of the forcing term F_{cd}. Given the analytical expression, it is impossible to isolate the variable u_l. Therefore a Taylor expansion w.r.t. $u_l = 0$ is made where only the constant and linear terms are kept and higher order nonlinear terms are neglected.

$$F_{cd}(V,u_l) = F_{cd,1} - F_{cd,2} \tag{K.10}$$

$$F_{cd,1} = \frac{F_{cd,1}(V,0)}{0!} + \frac{\frac{\partial F_{cd,1}(V,0)}{\partial u_l}}{1!}u_l + \cancel{\frac{\frac{\partial^2 F_{cd,1}(V,0)}{\partial u_l^2}}{2!}u_l^2} + \cancel{\frac{\frac{\partial^3 F_{cd,1}(V,0)}{\partial u_l^3}}{3!}u_l^3} + \cancel{\ldots} \tag{K.11}$$

$$F_{cd,1} = \frac{nA_{fingers}\epsilon_0 V^2}{2d_1^2} + \frac{nA_{fingers}\epsilon_0 V^2}{d_1^3}u_l \tag{K.12}$$

$$F_{cd,2} = \frac{F_{cd,2}(V,0)}{0!} + \frac{\frac{\partial F_{cd,2}(V,0)}{\partial u_l}}{1!}u_l + \cancel{\frac{\frac{\partial^2 F_{cd,2}(V,0)}{\partial u_l^2}}{2!}u_l^2} + \cancel{\frac{\frac{\partial^3 F_{cd,2}(V,0)}{\partial u_l^3}}{3!}u_l^3} + \cancel{\ldots} \tag{K.13}$$

$$F_{cd,2} = \frac{nA_{fingers}\epsilon_0 V^2}{2d_2^2} - \frac{nA_{fingers}\epsilon_0 V^2}{d_2^3}u_l \tag{K.14}$$

$$F_{cd,tay} = \frac{nA_{fingers}\epsilon_0 V^2}{2d_1^2} + \frac{nA_{fingers}\epsilon_0 V^2}{d_1^3} + \frac{nA_{fingers}\epsilon_0 V^2}{2d_2^2} - \frac{nA_{fingers}\epsilon_0 V^2}{d_2^3} \tag{K.15}$$

$$F_{cd,tay} = F_{cd,tay,0} + F_{cd,tay,1}u_l \tag{K.16}$$

All this can now be substituted into the ip EoM to obtain the (static) solution.

$$ku_l + EA\left(\frac{u_l}{l} + \frac{2\pi^2}{3l^3}q^2 + \varepsilon_0\right) = F_{cd,tay,0} + F_{cd,tay,1}u_l \tag{K.17}$$

Which can be rewritten to isolate u_l as.

$$u_l = \frac{F_{cd,tay,0} - EA\left(\frac{2\pi^2}{3l^3}q^2 + \varepsilon_0\right)}{k + \frac{EA}{l} - F_{cd,tay,1}} \tag{K.18}$$

With this degree of freedom isolated, it is now substituted into the oop EoM which had substituted in the expression for strain. This yields the strain equation to be.

$$m\ddot{w} - EA(\varepsilon_s w')' = 0 \tag{K.19}$$

$$m\ddot{w} - EA\left(\frac{u_l}{l} + \frac{2\pi^2}{3l^3}q^2 + \varepsilon_0\right)\frac{4\pi}{l^2}\sqrt{\frac{2}{3l}}cos\left(\frac{2\pi}{l}x\right)q(t) = 0 \tag{K.20}$$

$$m\ddot{w} - EA\left(\frac{\frac{F_{cd,tay,0} - EA\left(\frac{2\pi^2}{3l^3}q^2 + \varepsilon_0\right)}{k + \frac{EA}{l} - F_{cd,tay,1}}}{l} + \frac{2\pi^2}{3l^3}q^2 + \varepsilon_0\right)\frac{4\pi^2}{l^2}\sqrt{\frac{2}{3l}}cos\left(\frac{2\pi}{l}x\right)q(t) = 0 \tag{K.21}$$

There is still a dependency on the longitudinal variable x. Therefore the Galerkin approximation is consulted. To obtain this, the left-hand side of the above equation is multiplied with the oop modeshape $\frac{\psi}{q(t)} = \sqrt{\frac{2}{3l}}(1 - cos\left(\frac{2\pi}{l}x\right))$. This is then integrated along the membrane length. This leaves the equation simplified and two indicators of magnitude remain, $q(t)$ & $q^3(t)$. The coefficients in front of these factors thusly describe the linear and nonlinear (Duffing) type stiffness.

K.1. Results

Factoring out these two factors describing the amplitude of the linear and cubic stiffness (k_1&k_3) is a tedious process in which tiny mistakes are likely to be made. Therefore the "symbolic math" toolbox in MATLAB programming software was consulted to perform these isolations. The resulting two expressions hence become.

$$k_1 = \frac{4\,A_{\mathrm{gr}}\,\mathrm{E}\,\pi^2\left(\frac{-3\,A_{\mathrm{mems}}\,e_0\,n\,V^2\,{d_1}^3\,d_2\,l^3 + 3\,A_{\mathrm{mems}}\,e_0\,n\,V^2\,d_1\,{d_2}^3\,l^3 + 6\,A_{\mathrm{gr}}\,\mathrm{E}\,\varepsilon_0\,{d_1}^3\,{d_2}^3\,l^3}{2\,A_{\mathrm{gr}}\,\mathrm{E}\,{d_1}^3\,{d_2}^3 + 2\,{d_1}^3\,{d_2}^3\,k_{\mathrm{mems}}\,l - 2\,A_{\mathrm{mems}}\,V^2\,{d_1}^3\,e_0\,l\,n - 2\,A_{\mathrm{mems}}\,V^2\,{d_2}^3\,e_0\,l\,n} + 3\,\varepsilon_0\,l^3\right)}{9\,l^5} \tag{K.22}$$

$$k_3 = \frac{4\,A_{\mathrm{gr}}\,\mathrm{E}\,\pi^2\left(2\pi^2 - \frac{4\,A_{\mathrm{gr}}\,\mathrm{E}\,{d_1}^3\,{d_2}^3\,\pi^2}{2\,A_{\mathrm{gr}}\,\mathrm{E}\,{d_1}^3\,{d_2}^3 + 2\,{d_1}^3\,{d_2}^3\,k_{\mathrm{mems}}\,l - 2\,A_{\mathrm{mems}}\,V^2\,{d_1}^3\,e_0\,l\,n - 2\,A_{\mathrm{mems}}\,V^2\,{d_2}^3\,e_0\,l\,n}\right)}{9\,l^5} \tag{K.23}$$

Now all known parameters are substituted into these equations, as well as making some assumptions w.r.t. the flake thickness and parameters obtained from fitting the increase in resonance in Appendix H. Plotting the results for two different scenarios is depicted in Figure K.1.

K.2. Discussion

Having plotted this analysis for two different Young's modulii (15 MPa & 750 GPa) there are a number of things that can be discussed. Beginning with the observations of the graphs depicted in Figure K.1. For both scenarios, there is an initial nonlinear hardening that turns into a softening after a certain voltage. With the parameters in this plot, this switching point is independant of the Young's modulus and thus for both is ≈ 24.5 V, an interesting observation that is not directly apparent from the obtained equations. In the experiments, it was also found that there is a switch from nonlinear hardening to softening. Unfortunately, this switching point was observed at a third of this voltage around ≈ 8 V. Which tells us that either the model is incomplete, or the parameters used are incorrect. To resolve the latter it was attempted to alter the parameters such that a correspondence to the observations is obtained. This resulted however in completely unrealistic magnitudes.

The location of the second switching point (the asymptote) seems to be greatly dependent on the Young's modulus on the other hand. This indicates that the stiffness of the

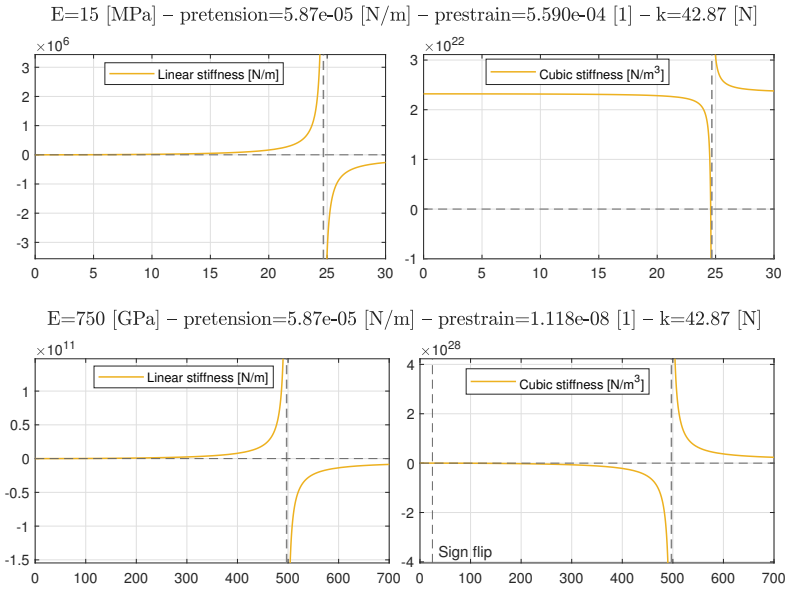

Figure K.1: Simulation of stiffnesses for device parameters as shown in the figure

membrane has a large influence on the behaviour of the MEMS device. There is however a problem with this second switching point. From the analysis, it seems that this asymptote follows from the snap-in behaviour of the MEMS device. In the experiments, a smooth transition from k_3 = positive → negative → positive. Therefore it is unlikely that this model completely describes the observations made from experiments.

Nevertheless, this model does give a clear indication to believe that the obtained effective mass using a high Young's modulus in Appendix H is not a good assumption and that the effective Young's modulus is a lot lower than the typical intrinsic values for graphene.

L

Fresnel diffraction

During the measurements of the modeshapes of the membrane, it could be observed how the results contain lines of zero optical response running through the obtained image. This can be observed in Figure 3.7. A colleague has analysed the cause of these lines and attributed it to what is called a Fresnel diffraction [52].

Fresnel diffraction is the diffraction of light when it passes through an aperture or around an obstacle. In this case, the aperture is the trench over which graphene is suspended. This trench has an interesting non-uniform geometry due to the presence of the electrostatic back-gate (which remains idle in this thesis). The result is an interference pattern, which is the superposition of waves that have travelled different paths. The intensity of the diffraction pattern is given by the Fresnel diffraction equation. The results of fitting these Fresnel equations are presented in Figure L.1.

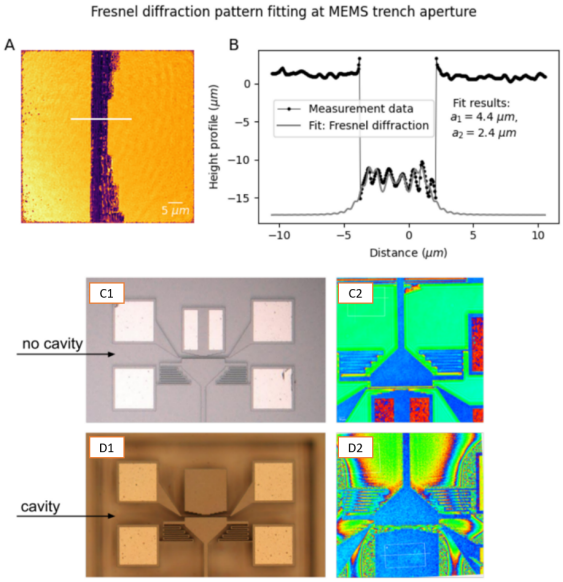

Figure L.1: (a) Interferometric surface profile image made using a 675 nm laser with indication of a profile line. (b) Fit using the Fresnel equations given the aperture dimensions to be that of the trench. (c,d) Optical and interferometric images that show respectively a MEMS device without and with a cavity layer. Illustrations adapted from [52]

This teaches us that the presence of the cavity layer in the MEMS die, causes light to greatly scatter and thus creating this interference which can be observed in the mode-shape measurements. The exact interference pattern is very sensitive to tiny changes in

alignment. The fact that large continuous lines of zero-response are visible in Figure 3.7 therefore shows the alignment of the sample shows very little drift. Which is has taken considerable effort.